國立臺灣大學電機資訊學院電子工程學研究所

碩士論文

Graduate Institute of Electronics Engineering

College of Electrical Engineering & Computer Science

National Taiwan University

Master Thesis

六方氮化硼基板應用於二硫化鉬薄膜電晶體與二硫化鉬-黑磷異質接面特性探討

Study of MoS_2 TFT with Hexagonal Boron Nitride Substrate and MoS_2-Black Phosphorus Heterostructures

洪彬超

Pin-Chao Hung

指導教授：李嗣涔 博士

Advisor: Lee Si-Chen, Ph.D.

中華民國 107 年 7 月

July, 2018

doi:10.6342/NTU201800956

中文口試委員審定書

國立臺灣大學碩士學位論文
口試委員會審定書

六方氮化硼基板應用於二硫化鉬薄膜電晶體
與二硫化鉬-黑磷異質接面特性探討
Study of MoS_2 TFT with Hexagonal Boron Nitride Substrate and MoS_2-Black Phosphorus Heterostructures

本論文係洪彬超君（R05943070）在國立臺灣大學電子工程學研究所完成之碩士學位論文，於民國 107 年 7 月 5 日承下列考試委員審查通過及口試及格，特此證明

口試委員：

（指導教授）

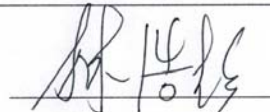

系主任、所長

1

doi:10.6342/NTU201800956

致謝

在碩士班這兩年能夠順利的完成論文並且畢業，首先要感謝我的指導教授李嗣涔博士，感謝老師給我研究上的指導，讓我找到研究方向。接著感謝 2D 組的學長張簡、昌哥、博彥，帶領我進入二維材料的領域，並且教導我如何使用儀器及實驗技巧。另外，也要感謝吳志毅老師實驗室的黃國祐學長、李家碩學長、沈新偉學長及吳肇欣老師實驗室的范鎧麟同學，在實驗上給予我協助。

接著，感謝實驗室的助理馬姐，幫我們處理實驗室許多大大小小的事務，讓我能夠專心地在研究上。感謝實驗室的黃偉倫學長、湯明儒學長、洪宗宏學長，不論是操作機台或是各項事務上也都給了我很大的幫助。也感謝與我同屆的實驗室成員曾奕融、蕭堯，有了你們的陪伴讓我在實驗上不會感到枯燥。也祝福學弟妹們：余凱文、彭天欣、王奇樺、郭哲劭實驗順利，準時畢業。

最後要感謝我的爸媽，有了你們的支持，讓我在求學期間沒有後顧之憂，並順利完成碩士學位，謝謝你們。謹以此論文獻給你們。

doi:10.6342/NTU201800956

摘要

本論文使用機械剝離法分離出擁有奈米級厚度的二硫化鉬並利用二氧化矽基板製作出薄膜電晶體，利用光學顯微鏡及原子力顯微鏡的搭配篩選出較佳厚度範圍的二硫化鉬，並利用低功函數金屬鉻當作金屬電極來達成歐姆接觸。其電晶體最好的場效電子遷移率可以達到 44.7 cm^2/V-s 與最低遲滯為 46.2 V。相較於二氧化矽，六方氮化硼具有較平滑的表面且無懸浮鍵與電荷缺陷，故以其取代二氧化矽作為二硫化鉬薄膜電晶體的基板以改善場效電子遷移率與降低遲滯效應。藉由導入六方氮化硼基板，二硫化鉬薄膜電晶體的場效電子遷移率能提升至 117 cm^2/V-s，遲滯降低至 5 V。此外，藉由比較二硫化鉬薄膜電晶體在兩種不同基板且不同大氣環境下，顯示遲滯效應主要是由二硫化鉬與氧化層之間接面特性所影響，而吸附在二硫化鉬表面的水氣與氧氣並不會造成遲滯效應。然而吸附在表面的水氣與氧氣會使二硫化鉬薄膜電晶體的特性隨時間而下降，因此六方氮化硼被用來當作二硫化鉬薄膜電晶體的保護層並且能使其有更好的穩定度。

接著使用三氟甲烷電漿使二硫化鉬薄膜有 p 型電洞參雜，且藉由 X 光光電子能譜儀可得知參雜後其費米能階往價電帶下降 0.4 eV。因此藉由三氟甲烷電漿參雜二硫化鉬形成 p 區並結合未參雜的二硫化鉬(n 區)成功的製作出二硫化鉬整流二極體，其開關電流比值大約為 100 倍、理想因子為 2.44。然而為了有更好的理想因子(介於 1 與 2 之間)，p 型二維材料黑磷被用來取代三氟甲烷電漿參雜的二硫化鉬

doi:10.6342/NTU201800956

並與未參雜二硫化鉬結合製作出二硫化鉬-黑磷異質接面，其開關電流比值大約為30倍、理想因子為1.84。最後利用寬頻氙燈量測二硫化鉬整流二極體與二硫化鉬-黑磷異質接面的光學特性，可以發現雖然二硫化鉬-黑磷異質接面的光響應比二硫化鉬整流二極體還要小，但二硫化鉬-黑磷異質接面有著比二硫化鉬整流二極體還要好的光偵測能力。

關鍵字：二硫化鉬薄膜二極體、六方氮化硼、遲滯效應、p型電洞參雜、二硫化鉬-黑磷異質接面

doi:10.6342/NTU201800956

ABSTRACT

In this thesis, the mechanically exfoliated 2D material MoS_2 nanosheet was successfully used to fabricate thin film transistor (TFT) on SiO_2 substrate. By using optical microscopy and atomic force microscopy, the MoS_2 flakes with appropriate thickness can be chosen. Ohmic contact of MoS_2 TFT can be achieved by low work function metal Chromium. The highest mobility of MoS_2 TFT on SiO_2 substrate is 44.7 cm^2/V-s and the lowest hysteresis is 46.2 V. In order to further improve the mobility and reduce the hysteresis, the SiO_2 substrate was replaced by h-BN substrate because h-BN has an atomically smooth surface that is relatively free of dangling bonds, charge traps and is naturally flat which can improve the interface property between MoS_2 and oxide layer. By introducing h-BN substrate, the mobility of MoS_2 TFT can be improved to 117 cm^2/V-s and its hysteresis can be reduced to 5 V. Furthermore, by comparing the performance of MoS_2 TFTs among SiO_2 and h-BN substrates with different atmospheric environment, it shows that interface property between MoS_2 and oxide layer would influence hysteresis seriously and the molecules such as H_2O and O_2 adsorbed on MoS_2 surface would not cause hysteresis. However, the molecules such as H_2O and O_2 adsorbed on MoS_2 surface would degrade the characteristics of MoS_2 TFT. Therefore, the h-BN passivation layer is used to passivated the MoS_2 TFT and it shows it has better stability

doi:10.6342/NTU201800956

by using h-BN passivation layer.

Besides, the CHF_3 plasma was used to dope the MoS_2 film to p-type material. By using XPS analysis, it shows that the Fermi level of MoS_2 film would shift about 0.4 eV toward the valence band. Therefore, CHF_3 plasma doping is used to generate p-region and combine with pristine MoS_2 (n-region) to fabricate MoS_2 rectifying diode. The current rectification ratio is about 2 order and its ideality factor is 2.44. In order to have better ideality factor (in the interval between 1 and 2), black phosphorus(BP) which is p-type 2D material is used to combine with MoS_2 to fabricate MoS_2-BP heterostructure n-p junction. The current rectification ratio is 30 and its ideality factor is 1.84 which is better than MoS_2 rectifying diode. Finally, the Xe lamp which is broadband light source is used to measure optical properties of MoS_2 rectifying diode and MoS_2-BP heterostructure n-p junction. It shows that although MoS_2-BP heterostructure n-p junction has lower responsivity than MoS_2 rectifying diode, it has better photodetecting ability than MoS_2 rectifying diode.

Key words: molybdenum disulfide (MoS_2) thin film transistor (TFT), hexagonal boron nitride (h-BN), hysteresis effect, p-type doping, MoS_2-Black Phosphorus heterostructure

doi:10.6342/NTU201800956

CONTENTS

中文口試委員審定書 i

致謝 ii

摘要 iii

ABSTRACT v

CONTENTS vii

LIST OF FIGURES xi

LIST OF TABLE xvii

Chpater 1 Introduction 1

1.1 Overview of Molybdenum Disulfide 1

1.2 Advantages of MoS_2 FETs 8

1.3 Motivation 11

Chpater 2 Experiments 14

2.1 Heterostructure Fabrication System 14

2.2 Reactive Ion Etching System 17

2.3 Measurement Techniques 18

2.3.1 Atomic Force Microscopy (AFM) 18

2.3.2 Raman Spectroscopy 18

doi:10.6342/NTU201800956

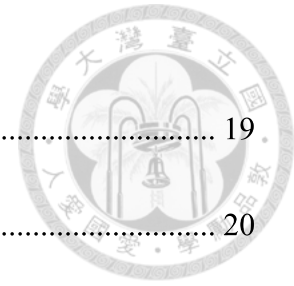

2.3.3 Photoluminescence (PL) 19

2.3.4 Photoemission Spectroscopy (PES) 20

2.3.5 Current-Voltage Characteristics 22

2.4 Rapid Thermal Annealing (RTA) 23

Chpater 3 Material Analysis 24

3.1 Substrate Preparation 24

3.2 Preparation of Exfoliated MoS_2 26

3.3 Characterization of MoS_2 Film Thickness 26

3.3.1 Optical Microscopy 27

3.3.2 Atomic Force Microscopy(AFM) 28

3.4 Optical and Vibrational Properties of MoS_2 31

3.4.1 Raman Spectroscopy 31

3.4.2 Photoluminescence(PL) 33

3.5 X-ray Photoelectron Spectroscopy(XPS) 37

3.5.1 XPS spectrum of MoS_2 38

3.5.2 Stability of MoS_2 in Air 39

3.5.3 Material Analysis of RIE doped MoS_2 41

3.6 Ultraviolet photoelectron spectroscopy(UPS) 43

doi:10.6342/NTU201800956

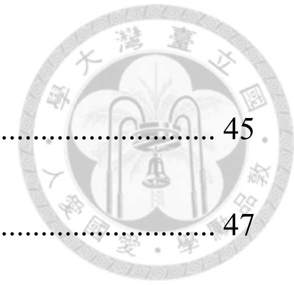

3.6.1 Work Function of MoS_2 45

3.6.2 Material Analysis of RIE doped MoS_2 47

Chpater 4 MoS_2 Thin Film Transistors 49

4.1 MoS_2 Back-gated TFTs using SiO_2 Substrate 49

4.1.1 Device Process Flow 49

4.1.2 Device Performance 52

4.2 MoS_2 Back-gated TFTs using h-BN Substrate 56

4.2.1 Device Process Flow 56

4.2.2 Device Performance 59

4.3 Comparison between SiO_2 and h-BN Substrate 62

4.3.1 Device Process Flow 62

4.3.2 Device Performance 64

4.4 Discussion of hysteresis and stability of MoS_2 TFT 67

4.4.1 Hysteresis in MoS_2 back-gated TFTs 67

4.4.2 Stability in MoS_2 back-gated TFTs 69

4.5 MoS_2 p-n rectifying diode 71

4.5.1 Device Process Flow 71

4.5.2 Device Performance 73

doi:10.6342/NTU201800956

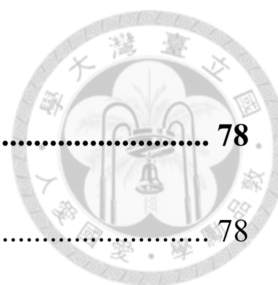

4.6 MoS_2-Black phosphorus (BP) heterostructure 78

4.6.1 Device Process Flow 78

4.6.2 Device Performance 80

4.7 Summary 87

Chpater 5 Conclusions 88

References.. 90

doi:10.6342/NTU201800956

LIST OF FIGURES

Fig. 1.1 The transition metals and the three chalcogen elements are shown in the periodic table ... 3

Fig. 1.2 Three dimensional representation of the structure of MoS_2 ... 3

Fig. 1.3 Three polytypes of MoS_2: 2H (two layers per unit cell), 3R (three layers per unit cell) and 1T (one layer per unit cell). ... 4

Fig. 1.4 The metal coordination and top view of 1T, 2H, and 3R phase. ... 4

Fig. 1.5 Calculated band structures of (a) bulk (b) quadrilayer (c) bilayer, and (d) monolayer MoS_2. ... 6

Fig. 1.6 Band gap energy of MoS_2 as function of layer number for N= 1~6. ... 6

Fig. 1.7 (a) A simple planar structure of FET. (b)The potential $\phi(x)$ distribution from the source to drain. (c) The potential energy distribution $U(x)$ for electrons from the source to drain. ... 10

Fig. 2.1 Three axis micrometer stage. ... 15

Fig. 2.2 Heterosutructure fabrication system. ... 15

Fig. 2.3 PDMS Stamp. ... 16

Fig. 2.4 h-BN flake on SiO_2/Si substrate under optical microscope. ... 16

Fig. 2.5 MoS_2 flake on PDMS under optical microscope. ... 16

doi:10.6342/NTU201800956

Fig. 2.6 Heterostructure of MoS_2 and hBN 17

Fig. 2.7 Diagram of RIE setup........ 18

Fig. 2.8 Diagram of how photoelectron is generated. 20

Fig. 2.9 The band diagram of an unknown material........ 21

Fig. 3.1(a) Thickness dependence of color and (b) contrast in optical microscope. 25

Fig. 3.2 Exfoliated MoS_2 on 300nm SiO_2/Si substrate under optical microscopy......... 28

Fig. 3.3(a) OM image of exfoliated MoS_2. AFM line profile for (b) blue (c) green (d) yellow (e) orange color of MoS_2 film........ 30

Fig. 3.4 Schematic illustration of in-plane phonon modes E^1_{2g} and the out-of-plane phonon mode A_{1g} for MoS_2. 32

Fig. 3.5 Thickness dependent Raman spectra for MoS_2........ 33

Fig. 3.6 Calculated band structures of (a) bulk (b) quadrilayer (c) bilayer, ... 34

Fig. 3.7 Photoluminescence spectra for monolayer, 4-layer and bulk MoS_2. 35

Fig. 3.8 The band structure of monolayer MoS_2 with the label of C calculated by the DFT. The arrows indicate the transition in A, B and the band nesting. 36

Fig. 3.9 The band diagram of X-ray photoelectron spectroscopy........ 38

Fig. 3.10 X-ray photoelectron spectroscopy for (a) Mo (b) S 39

Fig. 3.11 (a) Raman Spectra for monolayer and bulk MoS_2,respectively. (b) XPS profile

doi:10.6342/NTU201800956

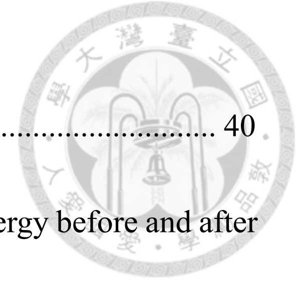

of the oxygen intensity at surface and inner MoS_2. 40

Fig. 3.12 The XPS spectra for (a) Mo 3d (b) F 1s (c) O 1s binding energy before and after plasma treatment. (d) The reported[73] XPS for Mo binding energy in the MoS_2 and MoO_3. 42

Fig. 3.13 Band diagram of an unknown material. 44

Fig. 3.14 (a), (b) and (c) UPS spectra of pristine MoS_2 46

Fig. 3.15 Band diagram of bulk MoS_2... 46

Fig. 3.16 UPS spectra for (a) 30s (b) 60s plasma treatment.. 48

Fig. 3.17 The band diagram of (a) pristine (b) plasma treatment for 30s (c) plasma treatment for 60s MoS_2... 48

Fig. 4.1 Patterned Substrate 50

Fig. 4.2 The flow chart for back-gated MoS_2 TFT fabrication process......................... 51

Fig. 4.3 (a) Cross-section view of device structure. (b) Top view of MoS_2 TFT under optical microscopy.. 51

Fig. 4.4 (a) top view of MoS_2 TFT under AFM. (b) The thickness of the MoS_2 flake measured by AFM. 53

Fig. 4.5 The characteristics of SiO_2 substrate MoS_2 TFT (a) I_d versus V_d characteristics. (b) I_d versus V_g curves in log and linear scale. 54

doi:10.6342/NTU201800956

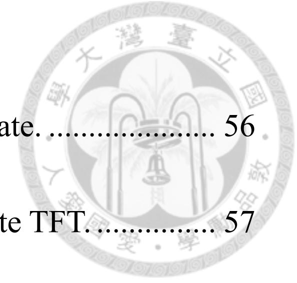

Fig. 4.6 The flow chart for MoS_2 back-gated TFT using h-BN substrate. 56

Fig. 4.7 Schematic flow of the fabrication process of h-BN substrate TFT. 57

Fig. 4.8 Top view of h-BN substrate TFT under optical microscopy. 58

Fig. 4.9 Raman spectra of h-BN substrate MoS_2 TFT. 58

Fig. 4.10 The characteristics of h-BN substrate MoS_2 TFT (a) I_d versus V_d (b) I_d versus V_g curves in log and linear scale. 60

Fig. 4.11 AFM image for the thickness of h-BN. 61

Fig. 4.12 MoS_2 and h-BN heterostructure with (a) The whole MoS_2 flake on the h-BN (b) half of MoS_2 flake on the h-BN under optical microscopy. 63

Fig. 4.13 (a)Cross-sectional view of device structure. (b) Top view of MoS_2 TFT under optical microscopy. Electrodes 1 and 2 are the TFT on SiO_2 substrate, whereas electrodes 3 and 4 are the TFT on h-BN substrate. 63

Fig. 4.14 I_d versus V_d characteristics of TFTs on the (a) SiO_2 substrate (b) h-BN substrate. They use the same MoS_2 flake. 64

Fig. 4.15 AFM image for the thickness of h-BN. 65

Fig. 4.16 I_d versus V_g characteristics of TFTs on the (a) SiO_2 substrate (b) h-BN substrate. They use the same MoS_2 flake. 66

Fig. 4.17 Hysteresis in transfer characteristics of MoS_2 TFT on SiO_2 substrate (a) before

doi:10.6342/NTU201800956

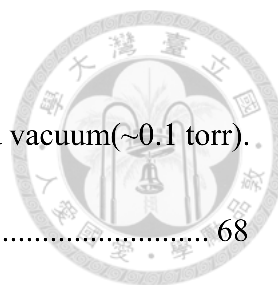

and after annealing (b) after annealing but measure in atmosphere and vacuum(~0.1 torr). 68

Fig. 4.18 MoS_2 back-gated TFT (a) without (b) with h-BN passivation layer. 69

Fig. 4.19 The variety of (a) mobility (b) on/off ratio (c) subthreshold swing after MoS_2 TFTs exposure in air for 28 days. 70

Fig. 4.20 The flow chart for MoS_2 p-n rectifying diode fabrication process. 71

Fig. 4.21 Schematic flow of the fabrication process of MoS_2 rectify diode.................. 72

Fig. 4.22 (a) MoS_2 flake with half region open(inside the dashed line) (b) Top view of MoS_2 rectifying diode under optical microscopy. 73

Fig. 4.23 I_d versus V_d of MoS_2 rectifying diode in log scale... 74

Fig. 4.24 The emission spectra of Xe lamp. 74

Fig. 4.25 The photoresponse of MoS_2 rectifying diode with different light intensity illumination... 76

Fig. 4.26 I_d versus V_d characteristics of MoS_2 rectifying diode under various incident light intensity. The inset shows the details in the reverse bias region. 77

Fig. 4.27 Photodetection responsivity of MoS_2 rectifying diode versus incident light intensity.. 77

Fig. 4.28 The flow chart for MoS_2-BP heterostructure fabrication process 78

doi:10.6342/NTU201800956

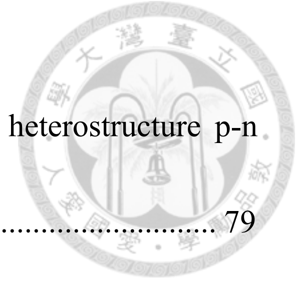

Fig. 4.29 Schematic flow of the fabrication process of MoS_2-BP heterostructure p-n junction. 79

Fig. 4.30 Top view of MoS_2-BP heterostructure (a) without electrode (b) with electrode. 80

Fig. 4.31 I_d versus V_d in log scale of MoS_2-BP heterostructure n-p junction. 80

Fig. 4.32 The photoresponse of MoS_2-BP heterostructure n-p junction with different light intensity illumination. 82

Fig. 4.33 I_d versus V_d characteristics of MoS_2-BP heterostructure n-p junction under various incident light intensity. The inset (1) shows the details in the negative bias region and the inset (2) shows the derails in the positive bias around 2V. 82

Fig. 4.34 Photodetection responsivity of MoS_2-BP heterostructure n-p junction versus incident light intensity. 83

Fig. 4.35 I_d versus V_d characteristics of MoS_2 TFT under various incident light intensity. The inset shows the details in the positive bias region from 1 to 2 V. 85

Fig. 4.36 I_d versus V_d characteristics of BP TFT under various incident light intensity. The inset shows the details in the positive bias region around 2 V. 86

Fig. 4.37 Responsivity of MoS_2 and BP TFT versus incident light intensity in semi-log scale. The black line is MoS_2 TFT and red line is BP TFT. 86

doi:10.6342/NTU201800956

LIST OF TABLE

Table 3.1 Thickness dependence of color for MoS_2 film on 300nm SiO_2/Si substrate under optical microscopy. 27

Table 4.1 Summary of MoS_2 TFT using SiO_2 substrate 55

Table 4.2 Summary of h-BN substrate back-gated MoS_2 TFT....................................... 61

Table 4.3 Summary of SiO_2 substrate and h-BN substrate MoS_2 TFTs 66

doi:10.6342/NTU201800956

Chpater 1 Introduction

1.1 Overview of Molybdenum Disulfide

Two dimensional (2D) material was not widely studied until the first experimental demonstration done by Novoselov et.al in 2004[1]. Novoselov exfoliated graphene from bulk graphite by using a scotch tape and they received the Nobel Prize in 2010. This is a useful method to fabricate a few atomic layered thick materials which are held together by weak Van der Waals force (40~70 meV). From then on, various 2D materials such as molybdenum disulfide (MoS_2) and hexagonal boron nitride (h-BN) have been successfully fabricated by mechanical exfoliation method of 2D material from bulk crystal by scotch tape[2, 3]. Thanks to the discovery of graphene, it opened a window to the entire family of 2D materials[4].

However, although graphene has high mobility and low resistance, gapless property of pristine graphene makes it difficult to turn off when used in field effect transistors(FET) so that it has poor on/off current ratio ($\sim 10^2$)[5, 6]. Because of its poor on/off current ratio, it is unsuitable to switching application. In 2011, the first single layered molybdenum disulfide (MoS_2) transistor was fabricated by Andras Kis group[7]. Single layered MoS_2 is a kind of transition metal dichalcogenides (TMDCs) which has higher energy bandgap and can be turned off when used in FET.

doi:10.6342/NTU201800956

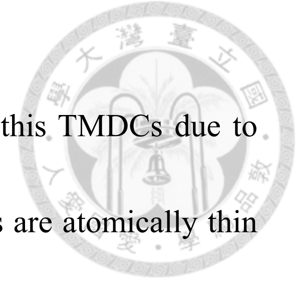

Recently, many researchers become interested in researching this TMDCs due to their properties complementary to those in graphene[8-10]. TMDCs are atomically thin semiconductors of the type MX_2, where M is a transition metal of groups 4-10 (except group 8) and X is a chalcogen as shown in Fig. 1.1. One layer of M atoms is sandwiched between two layers of X atoms and each layer is usually 6~7 Å thick as shown in Fig 1.2. TMDCs are held together by weak Van der Waals force between layers. Within each layer, the M-X bond is a covalent bond.

The crystal structure of single layer MoS_2 is similar to that of the graphene honeycomb lattice. However, each carbon atom in graphene is replaced by Mo or a pair of S atoms for MoS_2. In nature, MoS_2 has three polytypes which are 2H, 3R and 1T phases[11-13]. Both 2H and 3R phases are semiconducting and have trigonal prismatic coordination[13]. However, 1T phase is metallic[14] and has octahedral coordination[13]. The 2H-MoS_2, which is two layers per unit cell in the hexagonal symmetry, stacking sequence is AbA BaB (the capital represents chalcogen and the small letter represents metal in TMDCs). The 3R-MoS_2, which is three layers per unit cell in the rhombohedral symmetry, stacking sequence is AbA BcB CaC. The 1T-MoS_2, which is one layers per unit cell in tetragonal symmetry, stacking sequence is AbC [15] as shown in Fig. 1.3. The metal coordination and top view of this three phases are shown in Fig. 1.4.

doi:10.6342/NTU201800956

MX$_2$
M = Transition metal
X = Chalcogen

H																	He
Li	Be											B	C	N	O	F	Ne
Na	Mg	3	4	5	6	7	8	9	10	11	12	Al	Si	P	**S**	Cl	Ar
K	Ca	Sc	**Ti**	**V**	Cr	Mn	Fe	**Co**	**Ni**	Cu	Zn	Ga	Ge	As	**Se**	Br	Kr
Rb	Sr	Y	**Zr**	**Nb**	**Mo**	**Tc**	Ru	**Rh**	**Pd**	Ag	Cd	In	Sn	Sb	**Te**	I	Xe
Cs	Ba	La - Lu	**Hf**	**Ta**	**W**	**Re**	Os	**Ir**	**Pt**	Au	Hg	Tl	Pb	Bi	Po	At	Rn
Fr	Ra	Ac - Lr	Rf	Db	Sg	Bh	Hs	Mt	Ds	Rg	Cn	Uut	Fl	Uup	Lv	Uus	Uuo

Nature Nature chemistry vol 5 April 2013

Fig. 1.1 The transition metals and the three chalcogen elements are shown in the periodic table

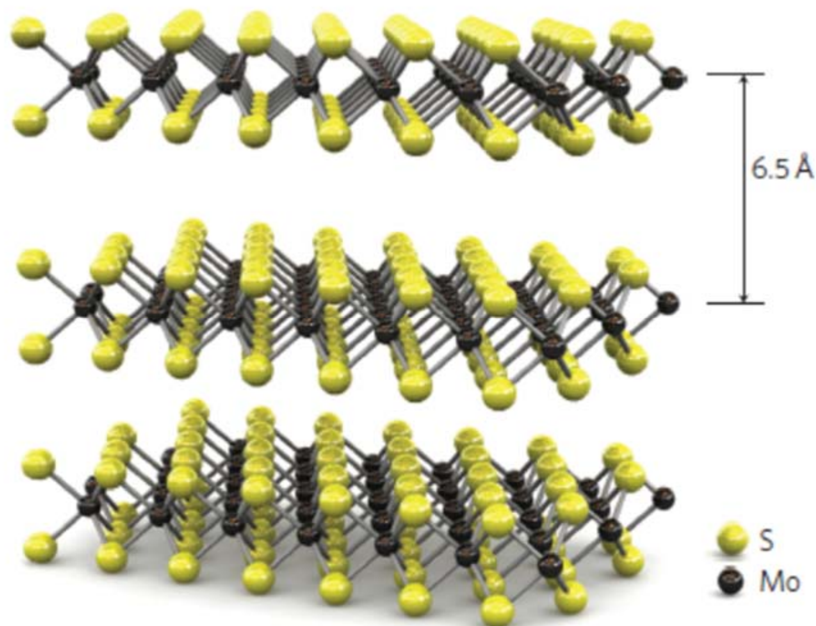

Nature Nanotechnology, **2011**, 6, 147-150

Fig. 1.2 Three dimensional representation of the structure of MoS_2

doi:10.6342/NTU201800956

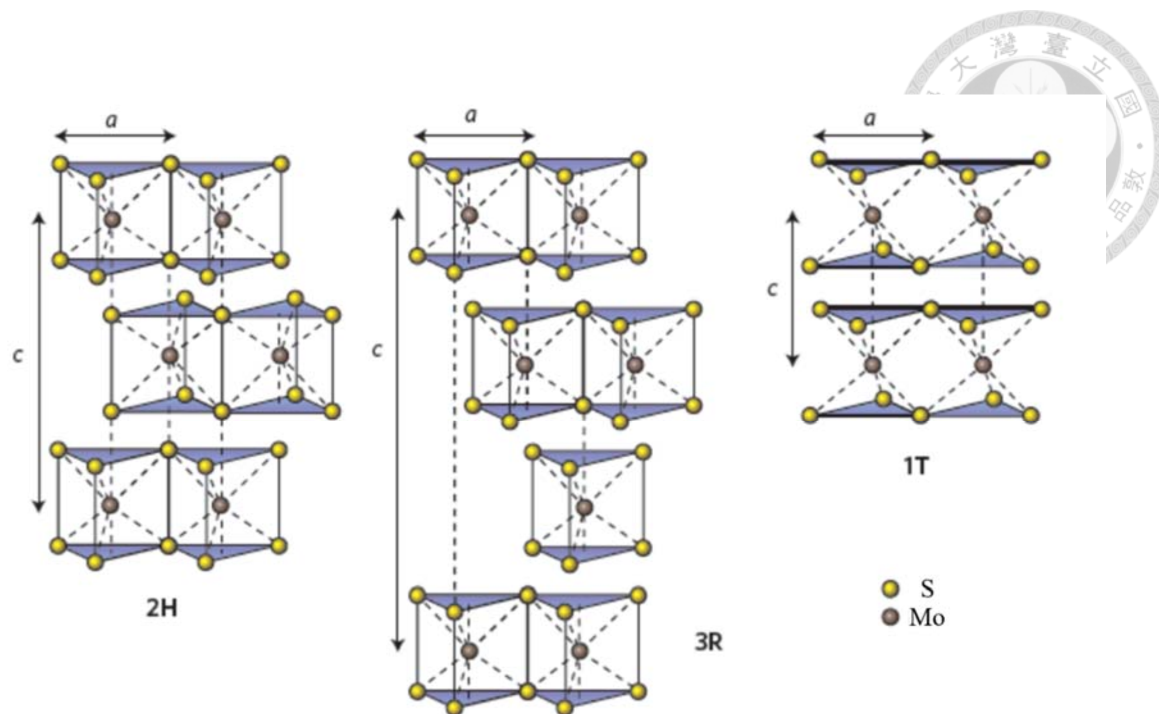

Nature Nanotechnology, 2012, 7, 699-712

Fig. 1.3 Three polytypes of MoS_2: 2H (two layers per unit cell), 3R (three layers per unit cell) and 1T (one layer per unit cell).

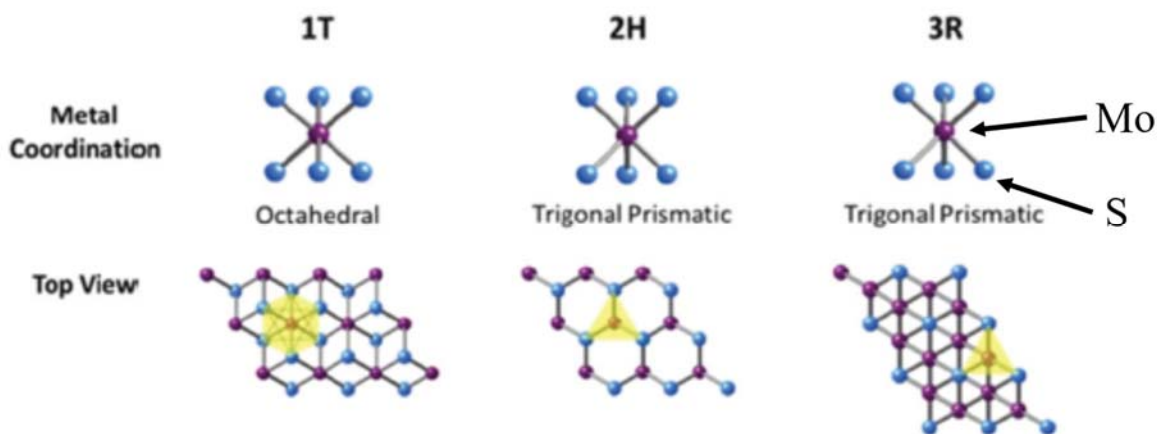

Chem Commun., 2017, 53, 3054-3057

Fig. 1.4 The metal coordination and top view of 1T, 2H, and 3R phase.

doi:10.6342/NTU201800956

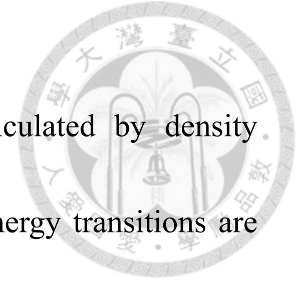

The band structures of MoS_2 with different thickness, calculated by density functional theory (DFT), are shown in Fig. 1.5[16]. The lowest energy transitions are labeled by the solid arrows. For bulk MoS_2 crystal, the valence band maximum is located at the Γ-point, while the conduction band minimum is located almost halfway along the Γ-K range. Therefore, bulk MoS_2 is an indirect bandgap material and its bandgap is 1.29eV. When the layer number decreases, the conduction minimum moves upward and the valence band maximum (Γ-point) moves downward. However, the direct transition at K-point barely changes when the layer number decreases. Finally, MoS_2 becomes a direct bandgap (~1.9eV)[2, 17, 18] material when it is a single layer. This phenomena could be explained as follows[16]: The conduction band states at the K-point are mainly composed of strongly localized d orbitals at Mo atom sites. Mo atoms are located in the middle of the S-Mo-S sandwich structure, so the interlayer coupling is weak. In contrast, states near the Γ-point and the point of indirect bandgap mainly originate from a linear combination of d orbitals at Mo atoms and antibonding p_z orbitals at S atoms. Strong interlayer coupling results in the energy dependence on layer thickness. Similar changes in the electronic band structure as a function of sample thickness have been predicted for other semiconducting 2D materials[19, 20]. The MoS_2 band gap energy versus layer number is summarized in Fig 1.6[2].

doi:10.6342/NTU201800956

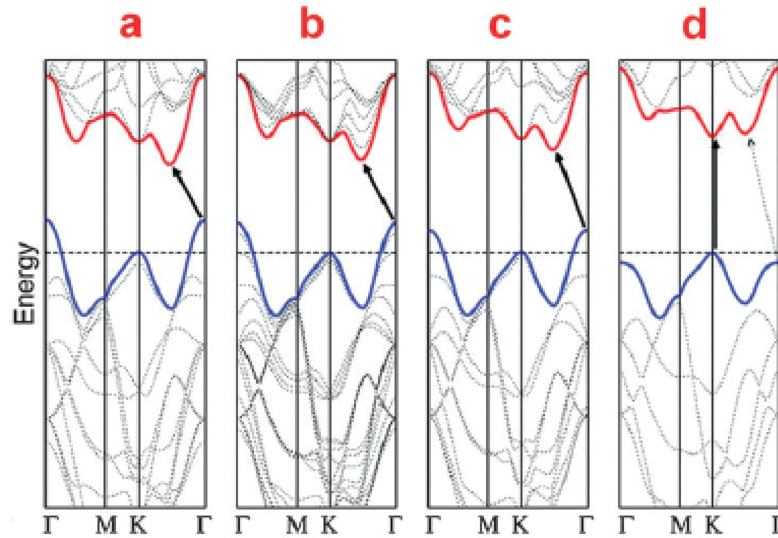

Nano letter, **2010**, 10, 1271-1275

Fig. 1.5 Calculated band structures of (a) bulk (b) quadrilayer (c) bilayer, and (d) monolayer MoS_2.

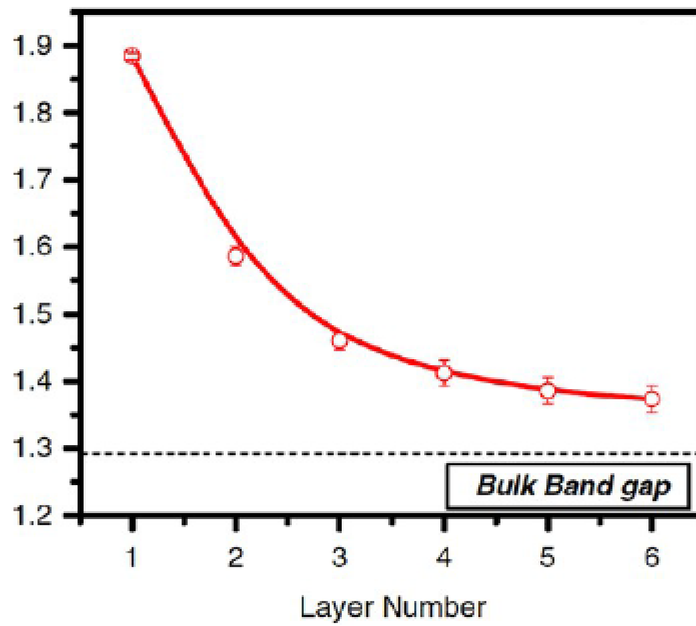

Phys. Rev. Letter. 2010, **105**, 136805.

Fig. 1.6 Band gap energy of MoS_2 as function of layer number for N= 1~6.

doi:10.6342/NTU201800956

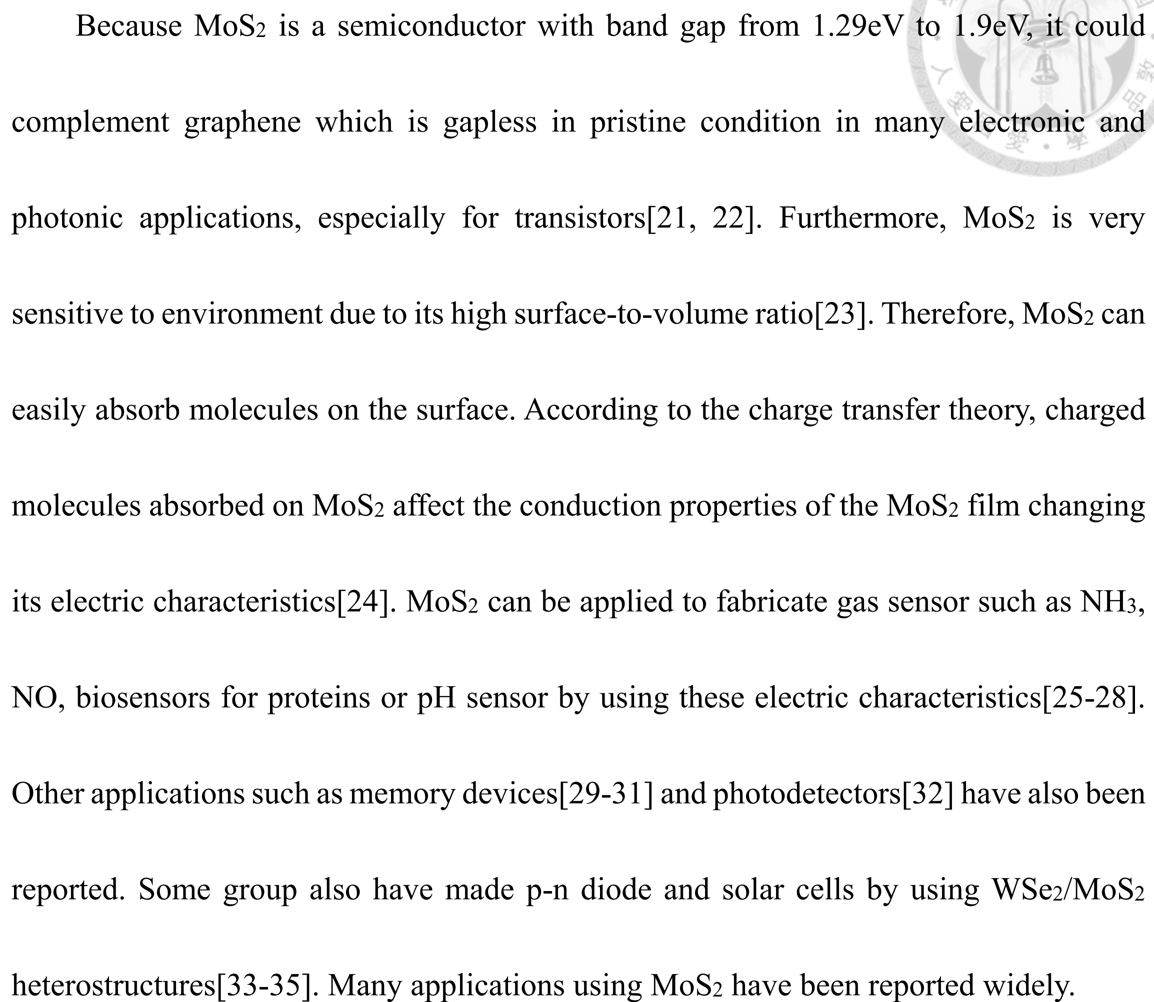

Because MoS_2 is a semiconductor with band gap from 1.29eV to 1.9eV, it could complement graphene which is gapless in pristine condition in many electronic and photonic applications, especially for transistors[21, 22]. Furthermore, MoS_2 is very sensitive to environment due to its high surface-to-volume ratio[23]. Therefore, MoS_2 can easily absorb molecules on the surface. According to the charge transfer theory, charged molecules absorbed on MoS_2 affect the conduction properties of the MoS_2 film changing its electric characteristics[24]. MoS_2 can be applied to fabricate gas sensor such as NH_3, NO, biosensors for proteins or pH sensor by using these electric characteristics[25-28]. Other applications such as memory devices[29-31] and photodetectors[32] have also been reported. Some group also have made p-n diode and solar cells by using WSe_2/MoS_2 heterostructures[33-35]. Many applications using MoS_2 have been reported widely.

doi:10.6342/NTU201800956

1.2 Advantages of MoS_2 FETs

Moore's Law had predict the development trend of semiconductor devices and the transistor keeps scaling in the past fifty years[36]. However, it will face a serious challenge in the next few generations of transistors. With the transistor size keeps scaling down, it will encounter several bottleneck such as large leakage current, short channel effect and so on[37]. The scaling theory has predicted that a field effect transistor with a thinner dielectric and a thinner gate-controlled region will ease the short channel effect down to very short gate length[38]. This can also be understood by the concept of characteristic length[39] as shown below.

The short channel planar transistor is shown in Fig 1.7 (a) and its potential $\phi(x)$ and potential energy $U(x)$ distribution are demonstrated in Fig 1.7 (b) and (c) respectively. The characteristic length λ is defined in Eq. (1.1) and the lowest potential along the channel is shown in Eq. (1.2).

$$\lambda = \sqrt{\frac{\varepsilon_s}{\varepsilon_{ox}} t_s t_{ox}} \quad (1.1)$$

$$\phi_{\min} \approx 2\sqrt{\phi_s \phi_d}\, e^{-L_{eff}/2\lambda} \quad (1.2)$$

Where λ is the characteristic length, ε_s ：the permittivity of semiconductor, ε_{ox} ：the permittivity of gate oxide, t_s ：thickness of semiconductor channel, t_{ox} ：thickness of

doi:10.6342/NTU201800956

gate oxide, $\phi_{\min}$ ：the lowest potential along the channel, ϕ_s ：the potential in the source, ϕ_d ：the potential in the drain, L_{eff} ：the effective channel length.

It is obvious that having a large ratio between L_{eff} and λ results in a smaller $\phi_{\min}$, which allows a better control of the gate when the channel scales down. Therefore, it can immune to short channel effect. While the channel length L_{eff} scales down, a large ratio between L_{eff} and λ requires a small λ, which means smaller channel dielectric constant, thinner dielectric and thinner channel thickness are required according to the Eq. (1.1).

In order to reduce short channel effect, the channel thickness of 3D materials (such as silicon) should become thinner. However, compared with 2D materials, the roughness at the 3D materials surface will degrade mobility seriously when it becomes thinner. Even worse, the channels showing a serious thickness fluctuations lead to unacceptably large threshold-voltage variations. These problems occur even at channel thicknesses many times greater than the thickness of 2D materials. On the other hand, monolayer MoS_2 not only owns ultrathin channel thickness but also has low dielectric constant compared with silicon (Si=11.9ε_0 and MoS_2=3.3ε_0). Besides, because of no out-of-plane broken bonds in 2D materials, there are no interface traps in the semiconductor channel and make it have a clean semiconductor-metal interface. Therefore, MoS_2 has the possibility to replace silicon and result in a better FETs.

doi:10.6342/NTU201800956

With its ultra-thin and sizable bandgap, MoS_2 has been widely studied by scientists around the word. It has been reported that 15 nm gate length MoS_2 transistors have on/off ratio up to 10^8~10^{10}, subthreshold swing (SS) of 60 mV per decade, and drain induced barrier lowering (DIBL) of 10 mV/V[40]. Many device simulations have also shown that MoS_2 has advantages over the scaling issue because of its immunity to short channel effect[40-42].

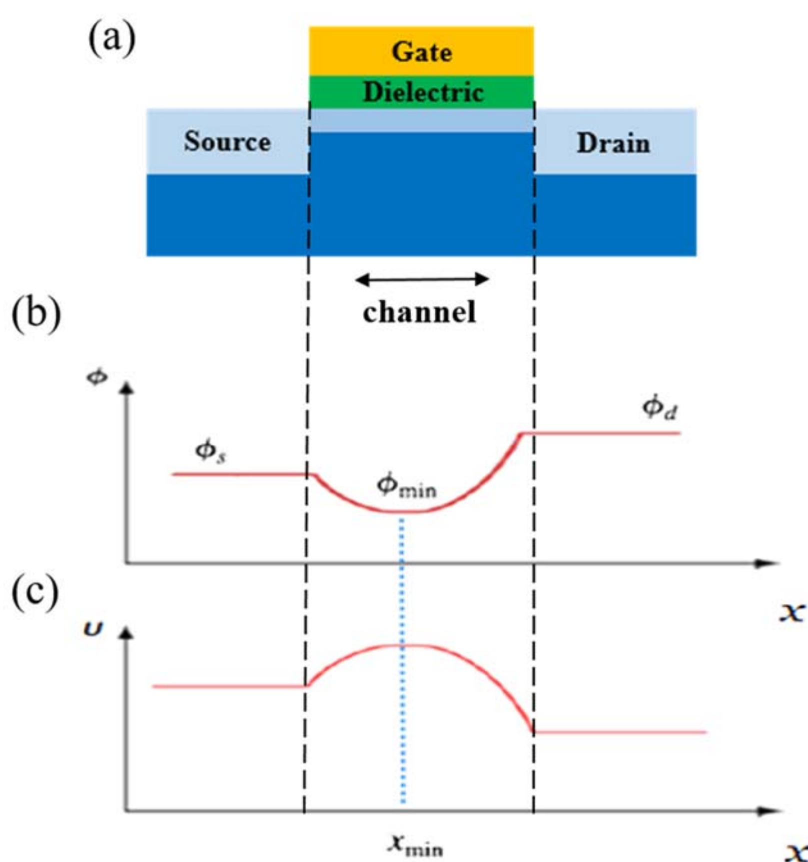

Fig. 1.7 (a) A simple planar structure of FET. (b)The potential $\phi(x)$ distribution from the source to drain. (c) The potential energy distribution $U(x)$ for electrons from the source to drain.

doi:10.6342/NTU201800956

1.3 Motivation

As mentioned above, MoS_2 material has the potential to replace the silicon. Recently, many researchers use SiO_2 as a bottom gate or high k material (such as Al_2O_3 and HfO_2) as a top gate to fabricate MoS_2 transistors[43-46]. However, the field effect mobility of MoS_2 transistors are around 10-65 $cm^2V^{-1}s^{-1}$ which is lower than the mobility of silicon (1400 $cm^2V^{-1}s^{-1}$ for electron and 450 $cm^2V^{-1}s^{-1}$ for hole respectively). Furthermore, the hysteresis of MoS_2 transistor is another important issue[47]. This is not desirable for logic switching applications because hysteresis increases the on/off switching voltage, thereby increasing the power consumption of the circuit[48]. In previous reports, it reports that the single or multi layers MoS_2 transistor has large hysteresis when using SiO_2 as an oxide layer[49-51]. Another important issue concerning the MoS_2 transistor is its stability. Some reports show that the performance of MoS_2 transistors would degrade after exposing to air for a long time[3].

It has been shown that the field effect mobility and hysteresis of MoS_2 transistors were strongly affected by interfacial charged impurities, surface roughness on Si/SiO_2 substrates and so on[3, 52]. In order to solve these problems, we will use hexagonal boron nitride (h-BN) substrate. It is a better choice which can be used to eliminate problematic surface effects in MoS_2 samples because it has an atomically smooth surface that is

doi:10.6342/NTU201800956

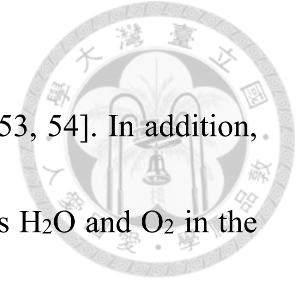

relatively free of dangling bonds, charge traps and is naturally flat[53, 54]. In addition, Single or multi layers MoS_2 can easily absorb the molecules such as H_2O and O_2 in the atmosphere because of its high surface-to-volume ratio[55]. Therefore, we will use h-BN as a passivation layer to let MoS_2 transistor have better stability and reliability.

MoS_2 also has another problem in CMOS compatible issue because of its naturally n-type characteristic. Recently, possible methods to modify MoS_2 has been reported[56-59]. The major method that most scientists do is to immerse MoS_2 in a fluid which can be served as a donor or acceptor[60-63]. In order to change MoS_2 film to p-type, some researchers use plasma which has Fluorine or Oxygen as a p-type doping for MoS_2[64-66]. Therefore, some reports have shown that it can fabricate MoS_2 rectify diode by using plasma-assisted doping as a p-region[67, 68]. However, the ideality factor of MoS_2 rectify diode is 2.21[67]. In order to have better ideality factor (in the interval between 1 and 2), black phosphorus(BP) which is p-type 2D material will be used to combine with MoS_2 to fabricate MoS_2-BP heterostructure n-p junction.

In this thesis, the introduction of MoS_2 and its development is presented in Chapter 1. The fabrication method of MoS_2/h-BN heterostructure and measurement systems are introduced in Chapter 2. The exfoliation method of MoS_2 and the material analysis of MoS_2 before and after plasma treatment to dope the material to either p or n-type are

doi:10.6342/NTU201800956

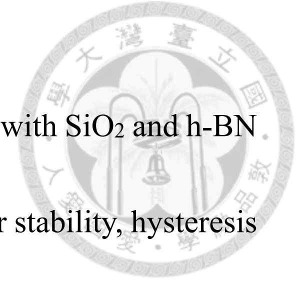

presented in Chapter 3. Chapter 4 presents the back-gate MoS_2 TFTs with SiO_2 and h-BN substrate, first. Then, we will use h-BN as a passivation layer. The air stability, hysteresis and electrical properties will also be discussed here. We will also present the characteristics of BP-MoS_2 heterostructure in this chapter. Finally, the conclusions are given in Chapter 5.

doi:10.6342/NTU201800956

Chpater 2 Experiments

In this chapter, the fabrication system of the heterostructure devices will be first introduced. Then the measurement techniques for material analysis and annealing techniques will be presented.

2.1 Heterostructure Fabrication System

Heterosutructure fabrication system, which consists of three axis micrometer stage (Fig. 2.1) and optical microscopy, is shown in Fig. 2.2. By using this micromanipulator, the MoS_2 or h-BN can be transfer to the desired position of our substrate.

After the setup of our system, we exfoliate the MoS_2 flakes on the PDMS stamp (Fig. 2.3). Second, the target sample is fixed on the stage (Fig. 2.2) by using double side tape and find the position that we want to fabricate heterostructure (Fig. 2.4). Third, the PDMS stamp is inspected under the optical microscope to select the flake that we want to use (Fig. 2.5). As the PDMS is transparent, we can see the target sample through it and thus it is possible to align the desired flake on the target sample where we want to transfer the flake with sub-micrometer resolution. Finally, as the desired position is reached, we can lower the glass slide with micromanipulator and let the PDMS stamp be adhered to the target sample to fabricate heterostructue, as shown in Fig. 2.6.

doi:10.6342/NTU201800956

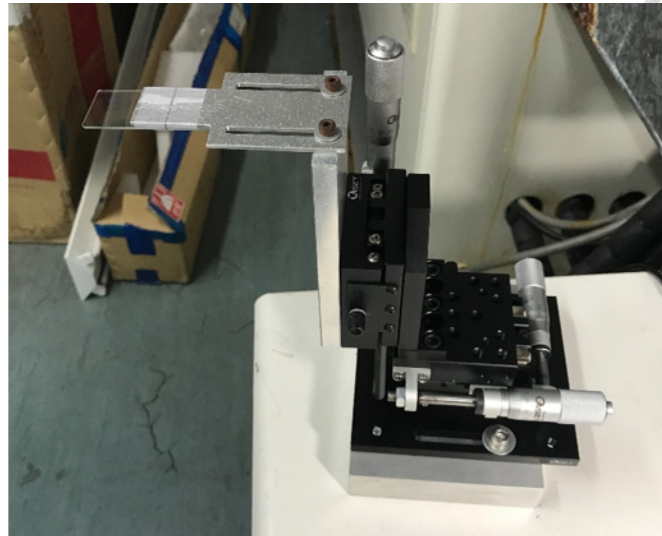

Fig. 2.1 Three axis micrometer stage.

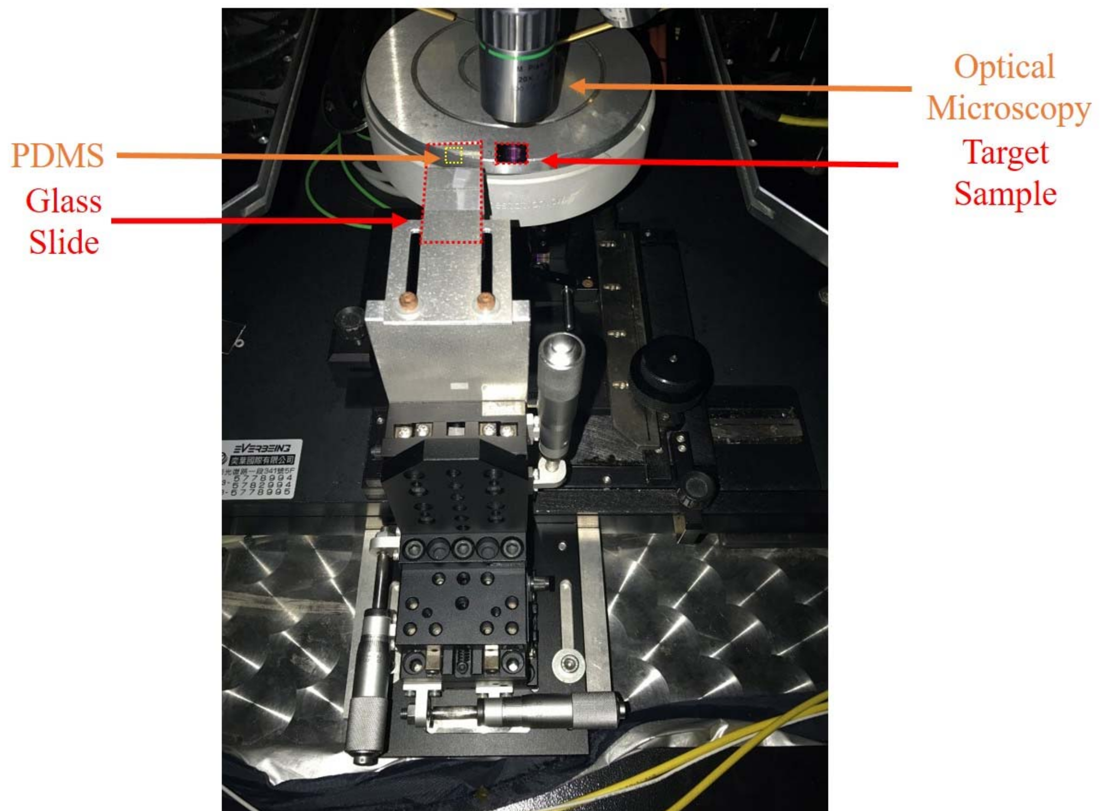

Fig. 2.2 Heterosutructure fabrication system.

doi:10.6342/NTU201800956

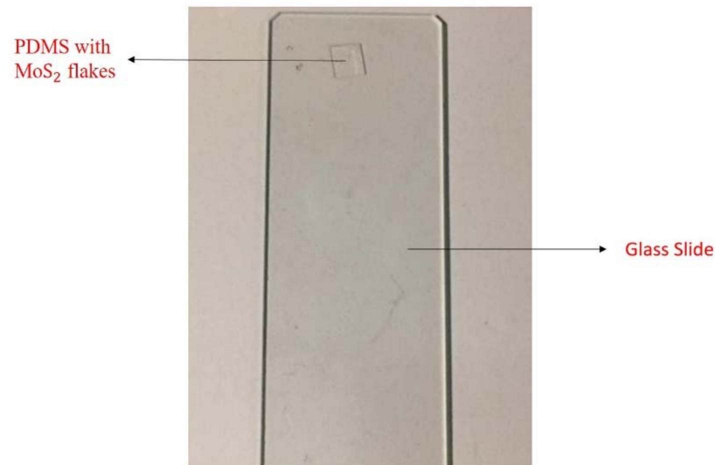

Fig. 2.3 PDMS Stamp.

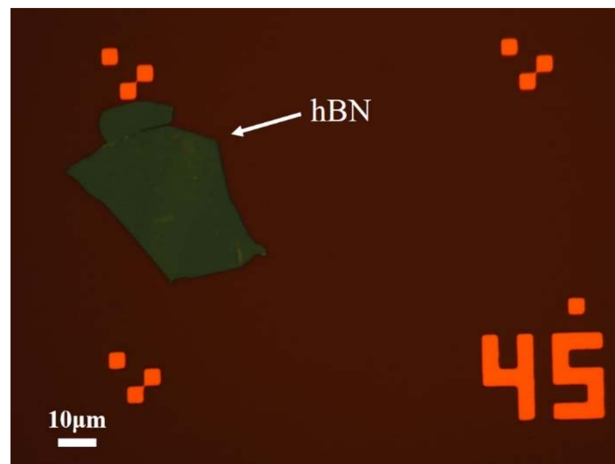

Fig. 2.4 h-BN flake on SiO_2/Si substrate under optical microscope.

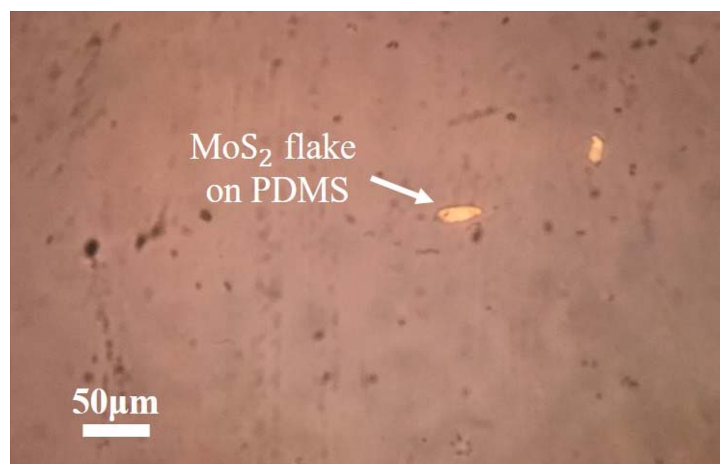

Fig. 2.5 MoS_2 flake on PDMS under optical microscope.

doi:10.6342/NTU201800956

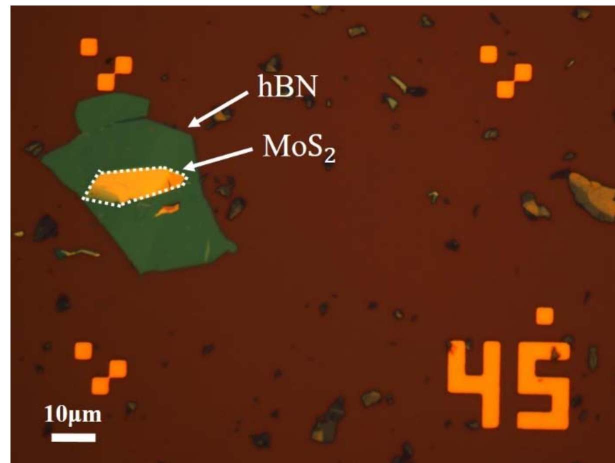

Fig. 2.6 Heterostructure of MoS_2 and hBN

2.2 Reactive Ion Etching System

Reactive ion etching (RIE) is an etching technology. There are two major etching technologies, dry etching and wet etching. RIE is one kind of dry etching, using chemically reactive plasma to remove materials on the wafers. In this study, we use RIE to generate plasma to itch the MoS_2 film and put dopants on the MoS_2 surface.

The operation method of RIE is illustrated in Fig. 2.7. Plasma is generated by applying a RF (13.56MHz) to the wafer platter. The strong electric field ionized the gas molecules to create a plasma. The electrons are accelerated up and down, directly attacking the wafer in the chamber.

doi:10.6342/NTU201800956

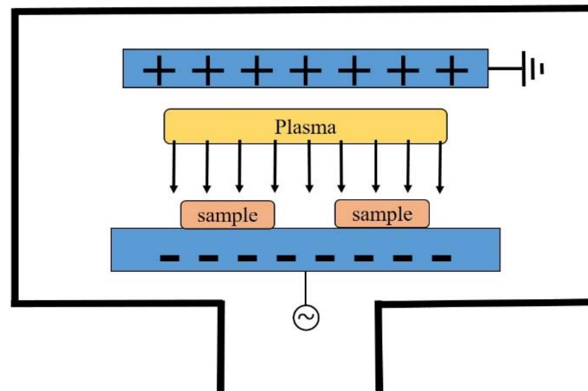

Fig. 2.7 Diagram of RIE setup

2.3 Measurement Techniques

2.3.1 Atomic Force Microscopy (AFM)

Atomic force microscopy (AFM) is a very high-resolution type of scanning probe microscopy, with demonstrated resolution on the order of fractions of a nanometer, more than 1000 times better than the optical diffraction limit.

In this experiment, AFM is used to check the thickness of MoS_2 and h-BN nanosheets by standard tapping mode, which relies on the decreasing of the oscillation amplitude when the tip comes close to the surface.

2.3.2 Raman Spectroscopy

Raman spectroscopy is a spectroscopic technique used to observe the lattice vibrational mode (phonon) of the MoS_2 film. The laser light interacts with molecular

doi:10.6342/NTU201800956

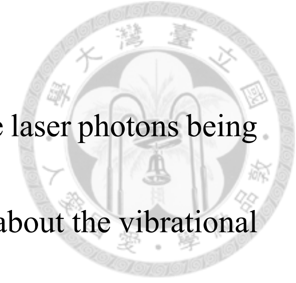

vibrations, phonons or other excitations, resulting in the energy of the laser photons being shifted up or down. Therefore, the shift in energy gives information about the vibrational modes in the system.

Raman spectroscopy occurs as a result of the atomic vibration causing a "change in polarizability" of the molecule. In contrast, Infrared spectroscopy occurs as a result of a vibration causing a change in the "permanent dipole moment". They always yield similar, but complementary information.

In this experiment, 532nm laser is used in Raman measurement. It gives the thickness information of MoS2 thanks to interlayer interactions in different thickness.

2.3.3 Photoluminescence (PL)

Photoluminescence describes the phenomenon of light emission from any form of matter after the absorption of photons. It is one of many forms of luminescence and is initiated by photoexcitation. The excitation typically undergoes various relaxation processes and then photons are re-radiated.

In this experiment, the evolution of the electronic structures of MoS2 nanosheets with various thicknesses can be reflected in their PL spectra.

doi:10.6342/NTU201800956

2.3.4 Photoemission Spectroscopy (PES)

Photoemission spectroscopy (PES), also known as photoelectron spectroscopy, refers to energy measurement of electrons emitted from solids, gases or liquids by the photoelectric effect. By using different incident light, photoemission spectroscopy has two major techniques which is Ultraviolet Photoemission Spectroscopy (UPS) and X-ray Photoelectron Spectroscopy (XPS). The basic theory of photoemission presented in Fig. 2.8.

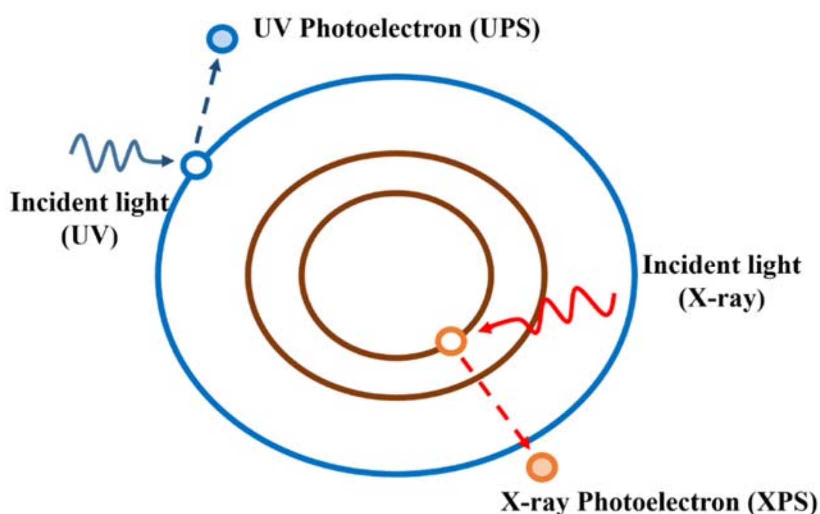

Fig. 2.8 Diagram of how photoelectron is generated.

2.3.4.1 Ultraviolet Photoemission Spectroscopy (UPS)

Ultra-violate photoemission spectroscopy (UPS) is to use ultraviolet photons to emit photoelectrons to determine the molecular orbital energies in the valence band region. Through analysis of photoelectron kinetic energy, we can calculate the binding energy of

doi:10.6342/NTU201800956

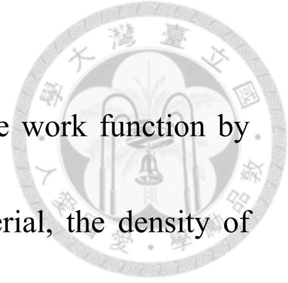

the specific molecular orbital energy. Besides, we can calculate the work function by using the below equation. The band diagram of an unknown material, the density of valence states and UPS spectrum are shown in Fig. 2.9.

$$E_{binding} = E_{photon} - (E_{kinetic} + \phi)$$

Where $E_{binding}$ is the binding energy of the electron from the Fermi-level, E_{photon}, which is hν as shown in Fig. 2.9, is the energy of the UV, $E_{kinetic}$ is the kinetic energy of the electron and ϕ is the work function of the material.

In this experiment, the Fermi level and work function differences before and after plasma treatment is presented.

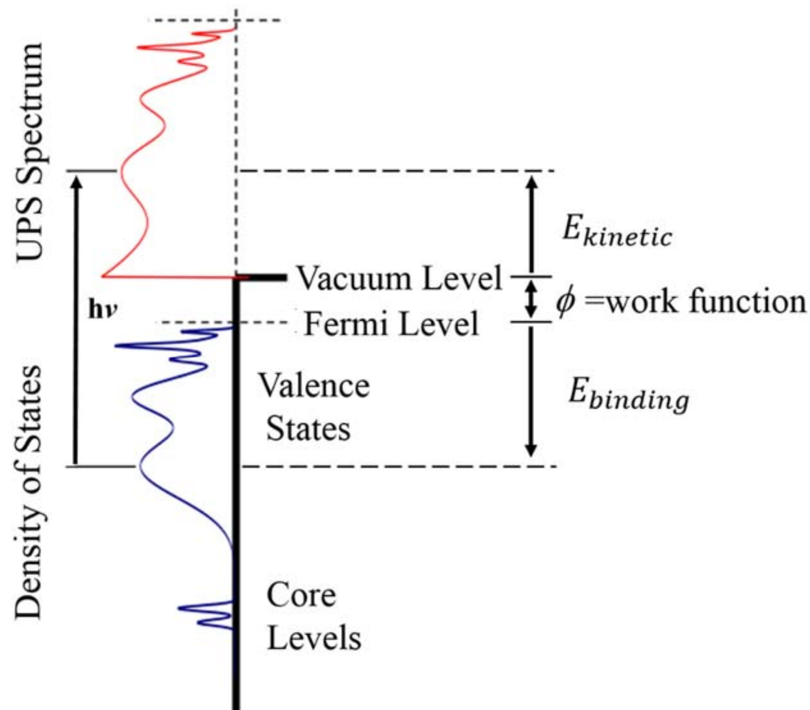

Fig. 2.9 The band diagram of an unknown material.

doi:10.6342/NTU201800956

2.3.4.2 X-ray Photoelectron Spectroscopy (XPS)

X-ray Photoelectron Spectroscopy (XPS) is a quantitative spectroscopic technique that measures the elemental composition, empirical formula, chemical state and electronic state of the elements that exist in a material. XPS spectra are obtained by irradiating a material with a beam of X-rays while simultaneously measuring the kinetic energy and number of electrons that escape from the top 1 to 10 nm of the material being analyzed. In this experiment, XPS is used to understand the element composition and atomic ratio of MoS2 bulk material.

2.3.5 Current-Voltage Characteristics

The current-voltage (I-V) characteristics of the MoS_2 thin film transistor were measured by Agilent B1500A Semiconductor Device Parameter Analyzer. The field effect mobility (μ_{EF}) of the TFT can be obtained by the transconductance (g_m) with a given V_D. The equation of field effect mobility is shown below.

$$\mu_{EF} = \frac{g_m}{C_i \frac{W}{L} V_D}$$

where W(L) is the channel width (length), C_i is the oxide capacitance per unit area. V_T can also be determined using linear extrapolation of the I_D -V_G plot.

doi:10.6342/NTU201800956

2.4 Rapid Thermal Annealing (RTA)

Rapid thermal anneal (RTA) is a subset of Rapid Thermal Processing (RTP). It is a process used in semiconductor device fabrication which consist of heating single semiconductor wafers in order to improve their electrical properties.

In this Experiment, MoS_2 thin film transistors were annealed by MILA 3000 Rapid Thermal Annealing Vacuum Furnace in N_2 environment at 200ºc for 5 minutes.

doi:10.6342/NTU201800956

Chpater 3 Material Analysis

In this chapter, the scotch tape method to exfoliate the MoS_2 film will be introduced. Next, the material analysis for the exfoliated and bulk MoS_2 will be investigated in details.

3.1 Substrate Preparation

The exfoliated MoS_2 was prepared from the bulk by using Nitto tape and transferring the flakes onto a highly doped p-type silicon substrate covered by 300 nm thermally oxidized SiO_2 layer. Before the transfer procedure, the silicon wafer was pre-cleaned by sonication in acetone, methanol, isopropyl alcohol and DI water each for 10 minutes. Then, the wafers were blown dry by nitrogen gas. This process removed any residue and contaminants on the wafer. Late et al.[69] found that when the film is inspected under the optical microscope, the level of contrast depends on the thickness of the oxide layer, as shown in Fig. 3.1 (a) and (b). As the thickness of MoS_2 increases, the color changes from purple to green to gold as a result of optical interference effects with the oxide layer. Just in analogy with graphene, the color contrast between MoS_2 nanosheet and the underlying SiO_2 is due to the interference of different wavelengths through the thin film and SiO_2, as shown in Fig. 3.1 (c).

doi:10.6342/NTU201800956

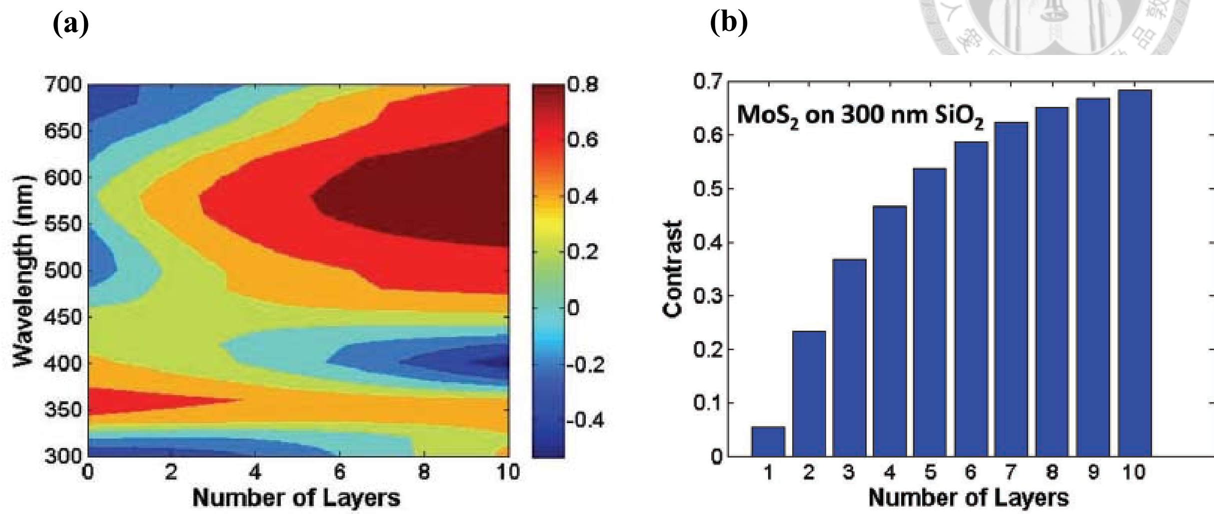

Advanced Functional Materials 2012, ***22 (9)***, *1894-1905.*

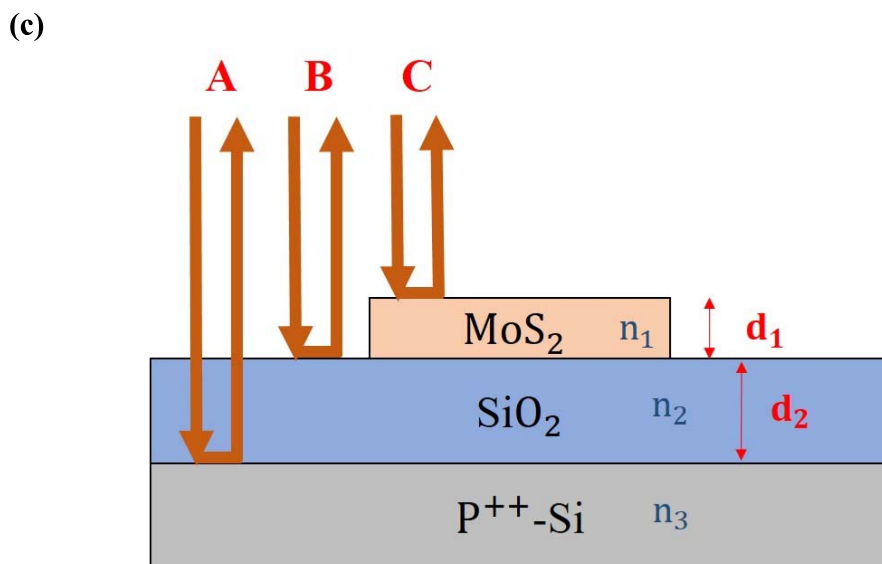

Fig. 3.1(a) Thickness dependence of color and (b) contrast in optical microscope. (c) Optical reflection and transmission for MoS_2 nanosheet with thickness d_1 and refractive index n_1 exfoliated on a SiO_2 layer with thickness d_2 and refractive index n_2 grown on a heavily doped Si substrate. Nanosheets on SiO_2 are visible due to interference between reflected light rays A, B and C.

doi:10.6342/NTU201800956

3.2 Preparation of Exfoliated MoS_2

First, small piece of bulk MoS_2 was torn off using Nitto scotch tape. Then, the Nitto tape was folded for several times in order to make the MoS_2 flakes become thinner. Next, the MoS_2 flakes were pasted onto SiO_2/Si substrate by Nitto scotch tape. Thin flakes were attached onto substrate with scotch tape residue. The scotch tape residue was removed by acetone alcohol immersion for 1 hours. Finally, the substrate was checked carefully under an optical microscope to find out the MoS_2 nanosheet with proper thickness.

3.3 Characterization of MoS_2 Film Thickness

For mechanically exfoliated MoS_2, it is important to locate the position of the MoS_2 film first. Next, AFM can be used to accurately determine both the vertical and lateral dimensions of nanosheets. However, AFM imaging is so time consuming and of relatively slow throughput, which is unsuitable for large area inspection.

As mentioned in Sec. 3.1, optical imaging offers a simple, rapid and non-destructive characterization of large-area samples. For convenience, the optical microscopy was first used for large-scale inspection so as to select an optimal nanosheet with an appropriate thickness. After choosing the nanosheet, AFM is then used to quantitatively measure its thickness.

doi:10.6342/NTU201800956

3.3.1 Optical Microscopy

Optical contrast can be used to differentiate MoS_2 nanosheets with different thickness on SiO_2/Si substrates. The level of contrast depends on the thickness of the oxide layer and the optimal oxide thickness for identifying MoS_2 thickness is about 300nm. Table 3.1 and Fig. 3.2 depict how the color of MoS_2 nanosheets changes with its thickness on 300nm SiO_2/Si substrates. The color of few layer MoS_2 flakes are blue under the optical microscopy. As the thickness increases, the color changes from green to orange as a result of optical interference effects with the oxide layer.

Once a flake of interest has been located using optical microscopy, the exact thickness can be confirmed by AFM.

Table 3.1 Thickness dependence of color for MoS_2 film on 300nm SiO_2/Si substrate under optical microscopy.

MoS_2 thickness	Color
<10nm	blue
10~20 nm	Green
20~40 nm	Yellow
>40 nm	Orange

doi:10.6342/NTU201800956

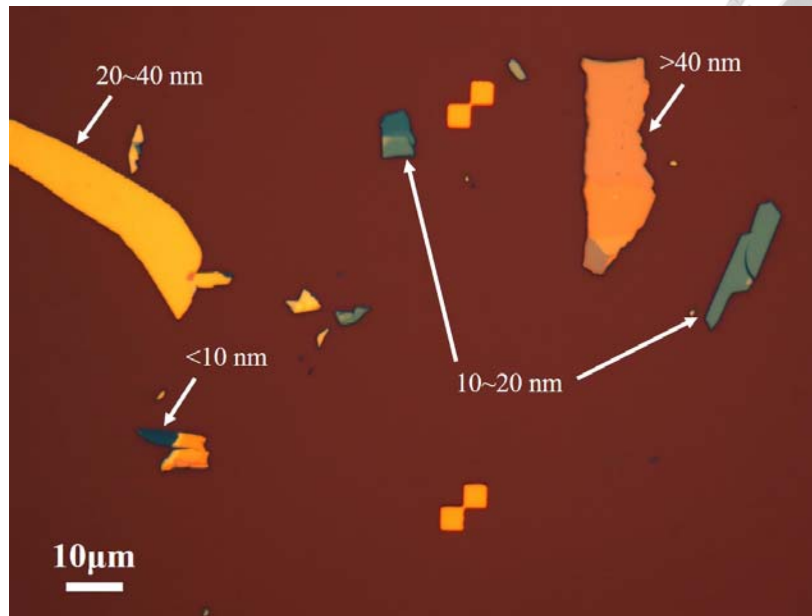

Fig. 3.2 Exfoliated MoS_2 on 300nm SiO_2/Si substrate under optical microscopy

3.3.2 Atomic Force Microscopy(AFM)

In this section, the color of MoS_2 nanosheets changes with its thickness on 300nm SiO_2/Si substrates are confirmed by AFM. Fig. 3.3 (a) displays two regions, (i) and (ii), in region (i), although the MoS_2 flake has different color, we just measure its thickness in blue region. In region (ii), it has three color which are green, yellow and orange. The thickness of blue MoS_2 film is 6nm as shown in Fig. 3.3 (b). The thickness of green, yellow and orange MoS_2 films are 15, 23, 60nm as shown in Fig. 3.3 (c), (d), and (e), respectively. From Fig. 3.3, it verifies that the thickness correspondence table in Table 3.1 is correct. And we can use the OM image to find the proper thickness of MoS_2 film that we want to use quickly.

doi:10.6342/NTU201800956

(a)

(b)

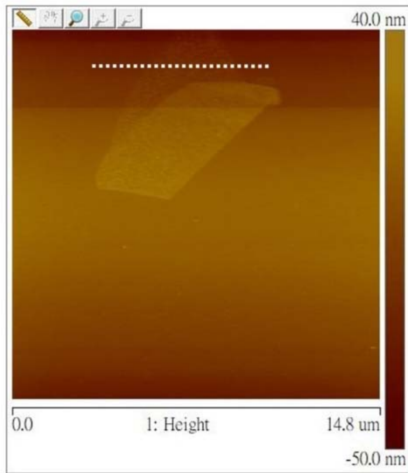

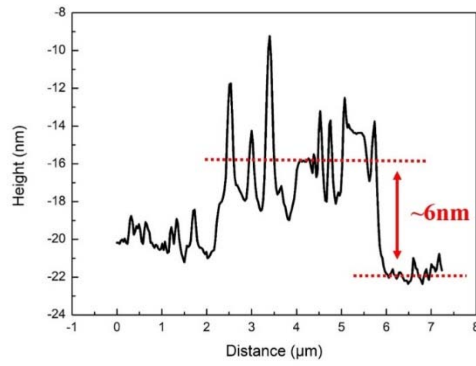

doi:10.6342/NTU201800956

(c)

(d)

(e)

Fig. 3.3(a) OM image of exfoliated MoS_2. AFM line profile for (b) blue (c) green (d) yellow (e) orange color of MoS_2 film.

doi:10.6342/NTU201800956

3.4 Optical and Vibrational Properties of MoS_2

After the thickness of MoS_2 flake was measured by AFM, they were also analyzed by Raman and Photoluminescence (PL) in order to understand their optical and vibrational properties

3.4.1 Raman Spectroscopy

Raman spectroscopy is another useful technique to quantitatively determine the layer thickness of MoS_2. The main Raman peaks correspond to the in-plane E^1_{2g} and the out-of-plane A_{1g} mode are shown in Fig. 3.4. The E^1_{2g} is an in-plane mode resulting from the opposite vibration of two S atoms with respect to the Mo atom between them, while the A_{1g} mode is attributed to the out-of-plane vibration of only S atoms in opposite directions[60]. The system used in our experiment utilizes a 532nm laser. Importantly, it is necessary to use a low laser power to prevent sample decomposition. The power used here is 50mW.

The Raman spectra of E^1_{2g} and A_{1g} mode shift as the thickness of MoS_2 film changes, as shown in Fig. 3.5. For bulk MoS_2, the A_{1g} mode locates at about 407.7 cm^{-1} and E^1_{2g} mode is near 382.3 cm^{-1}. The peak separation A_{1g} - E^1_{2g} = 25.4 cm^{-1}. When the MoS_2 layer thickness decreases, the A_{1g} mode red shifts whereas the E^1_{2g} mode blue shifts. The

doi:10.6342/NTU201800956

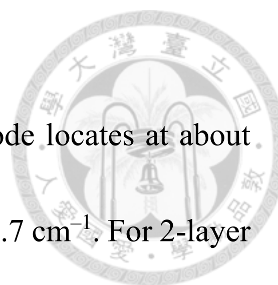

peak separation becomes smaller. For monolayer MoS_2, the A_{1g} mode locates at about 404 cm^{-1} and E^1_{2g} mode is near 385.3 cm^{-1}. The peak separation is 18.7 cm^{-1}. For 2-layer MoS_2, the A_{1g} mode locates at about 405.1 cm^{-1} and E^1_{2g} mode is 383.1 cm^{-1}. The peak separation is 21.7 cm^{-1}. For 3-layer MoS_2, the A_{1g} mode locates at about 407.3 cm^{-1} and E^1_{2g} mode is 383.5 cm^{-1}. The peak separation is 23.8 cm^{-1}. For 4-layer MoS_2, the A_{1g} mode locates at about 407.5 cm^{-1} and E^1_{2g} mode is 382.9 cm^{-1}. The peak separation is 24.6 cm^{-1}. Therefore, we can use Raman spectroscopy to identify MoS_2 film from monolayer to 4-layer.

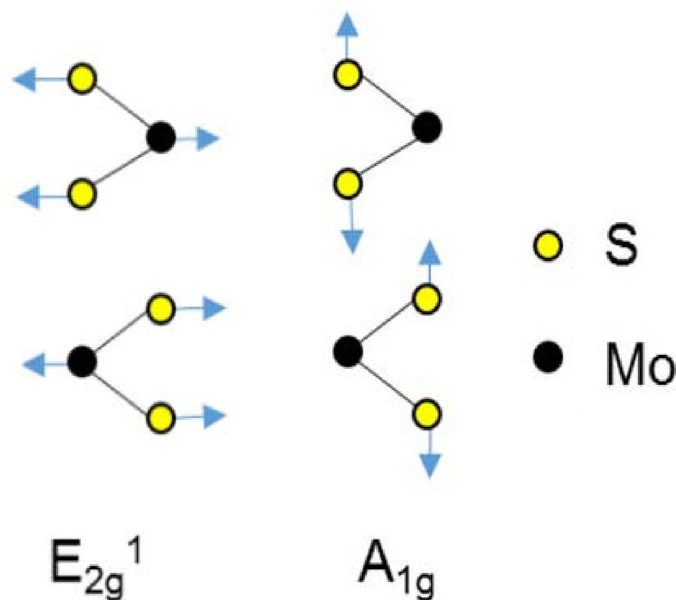

Photonics **2015**, *2*(1), 288-307

Fig. 3.4 Schematic illustration of in-plane phonon modes E^1_{2g} and the out-of-plane phonon mode A_{1g} for MoS_2.

doi:10.6342/NTU201800956

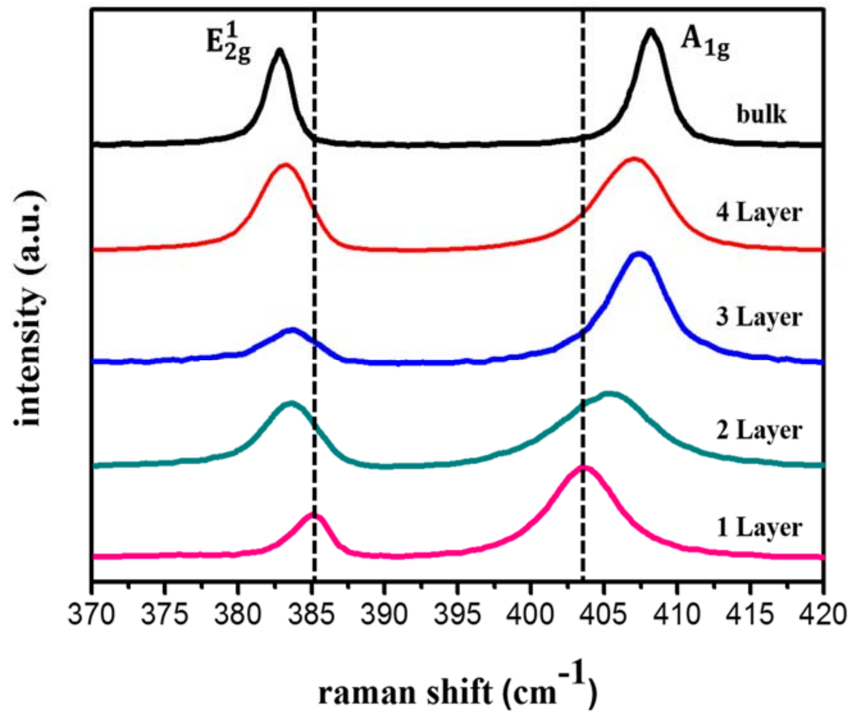

Fig. 3.5 Thickness dependent Raman spectra for MoS_2.

3.4.2 Photoluminescence(PL)

Bulk MoS_2 is a semiconductor with an indirect bandgap of about 1.3 eV and single layer MoS_2 has a direct bandgap of ~1.8 eV[2, 17, 18]. According to density functional theory (DFT), the band structures of MoS_2 with different thickness is shown in Fig. 3.6[16]. For bulk MoS_2, the direct transition occurs at K-point which has a high energy. Therefore, bulk MoS_2 is an indirect bandgap material. However, as the MoS_2 layer thickness decreases, the transition between conduction band minimum and valence band maximum at Γ-point becomes larger, while the direct transition at K-point barely changes.

doi:10.6342/NTU201800956

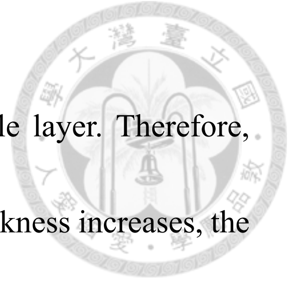

Finally, MoS_2 becomes a direct bandgap material when it is single layer. Therefore, single layer MoS_2 has a ~1.8 eV direct bandgap. With the MoS_2 thickness increases, the bandgap of MoS_2 becomes smaller and changes from direct bandgap to indirect bandgap.

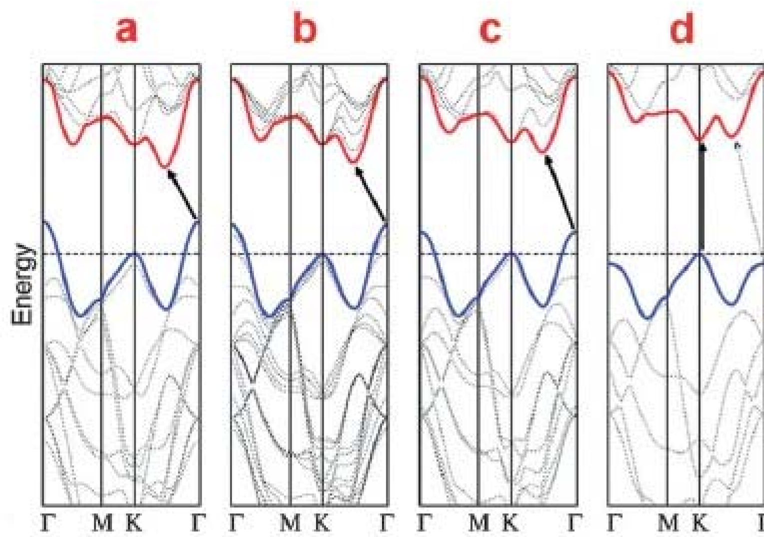

Nano letter, **2010**, 10, 1271-1275

Fig. 3.6 Calculated band structures of (a) bulk (b) quadrilayer (c) bilayer, and (d) monolayer MoS_2.

The PL system used in our experiment utilizes a 532nm laser with a power of 5mW, measured at 300K. The bulk MoS_2 showed negligible PL compare to monolayer MoS_2 PL as shown in Fig. 3.7. Thinner MoS_2 exhibited pronounced emissions at about 670 and 625 nm. These two peaks arise from the direct excitonic transitions at the K-point as shown in the arrow A and B in Fig. 3.8. The energy difference between these two peaks

doi:10.6342/NTU201800956

originates from the spin-orbit splitting of the valence band energy[16]. In Fig. 3.7, the black and red line represents photoluminescence spectra for 1 and 4 layer MoS_2 film, respectively. The difference of major peak position is barely changes because of the unchanged direct transition at K-point as discussed above. Furthermore, it was also shown that the PL intensity was decreased as the layer number of MoS_2 nanosheets increases. In bulk MoS_2, no photoluminescence is observable because of the local field effect, that is, the local electric field at a high refractive index material like MoS_2 is much weaker than the incident electrical field[16].

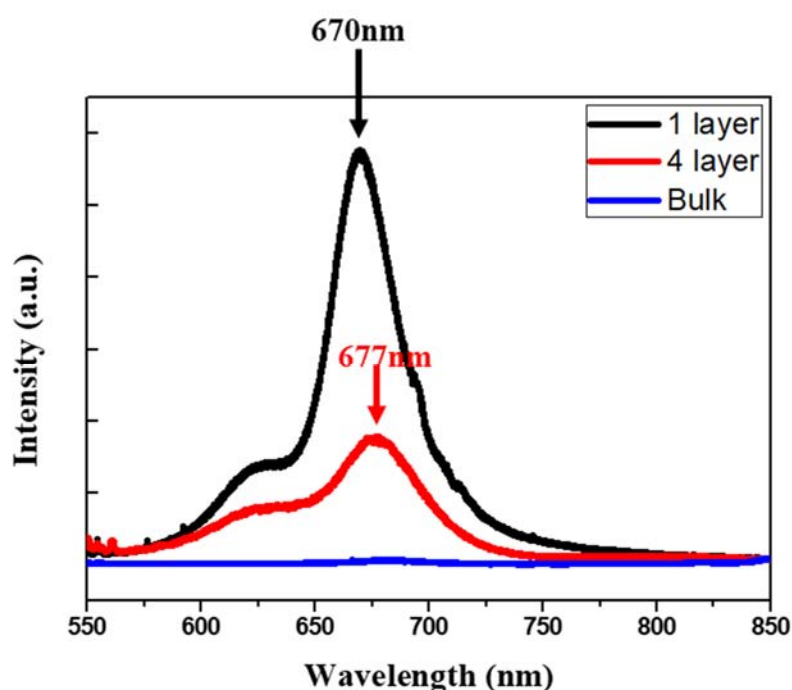

Fig. 3.7 Photoluminescence spectra for monolayer, 4-layer and bulk MoS_2.

doi:10.6342/NTU201800956

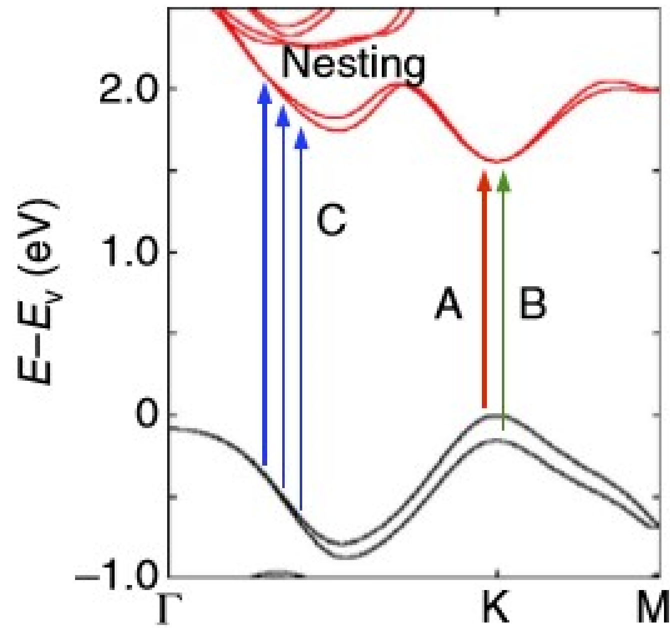

Nature Comm., **2014**, 5, 4543

Fig. 3.8 The band structure of monolayer MoS_2 with the label of C calculated by the DFT. The arrows indicate the transition in A, B and the band nesting.

doi:10.6342/NTU201800956

3.5 X-ray Photoelectron Spectroscopy(XPS)

X-ray photoelectron spectroscopy is a useful technique to determine the composition of an unknown materials. XPS is based on the photoelectric effect. Each atom has core electron with the characteristic binding energy. When the X-ray beam hits on the surface of sample, the core electron will absorb the energy of X-ray photon. If the photon energy (E_{photon}) is large enough, the core electron will escape from the atom and emit out of the surface. The emitted electron with the kinetic energy E_k will be detect by energy analyzer. Then we can use the below equation to calculate the core electron binding energy.

$$E_{binding} = E_{photon} - (E_k + \phi_{sp}) \qquad (3.1)$$

Where $E_{binding}$ is the binding energy of the core electron, E_{photon} is the X-ray photon energy, E_k is the kinetic energy of photoelectron which can be measured by the energy analyzer and ϕ_{sp} is the work function of the analyzer. Because the Fermi level of the sample and spectrometer are aligned, the spectrometer work function (ϕ_{sp}) is already known. Therefore, we can use above equation to get the binding energy. The band diagram of XPS is shown in Fig. 3.9.

In the section, we use XPS to analyze stability of MoS_2 in air and Fermi level shift before and after plasma treatment.

doi:10.6342/NTU201800956

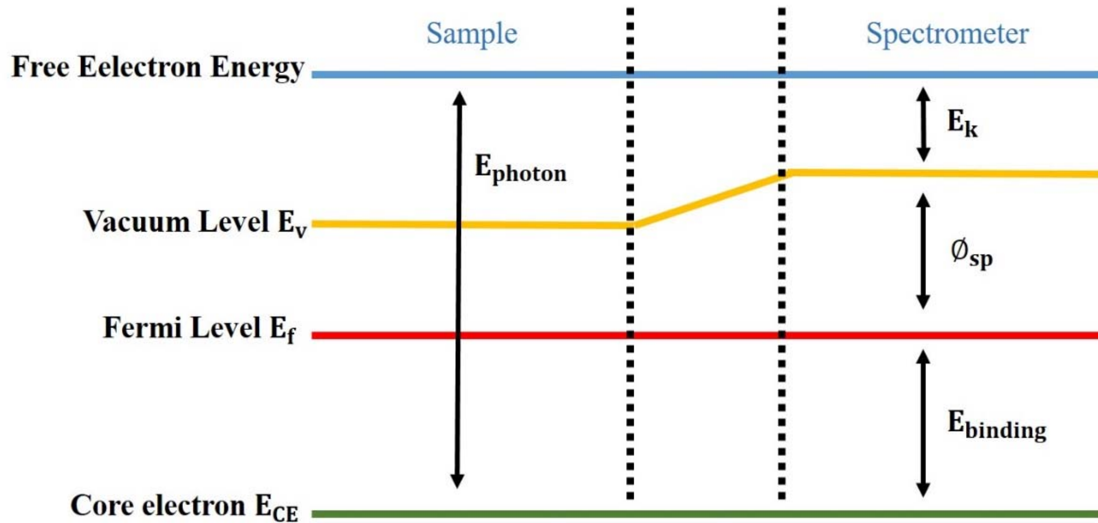

Fig. 3.9 The band diagram of X-ray photoelectron spectroscopy.

3.5.1 XPS spectrum of MoS_2

X-ray photoelectron spectroscopy is measured in high vacuum (~10^8 torr) to reduce environmental interference. Fig. 3.10 (a) shows 3 peaks of Mo and S signal, one is Mo^{4+} $3d_{5/2}$ which is at 229.3 eV, another is Mo^{4+} $3d_{3/2}$ which is at 232.5 eV, the other is S 2s which is at 226.6 eV. Fig. 3.10 (b) shows 2 peaks of S signal, one is S $2P_{3/2}$ which is at 162.1 eV and the other is S $2p_{1/2}$ which is at 163.3 eV.

doi:10.6342/NTU201800956

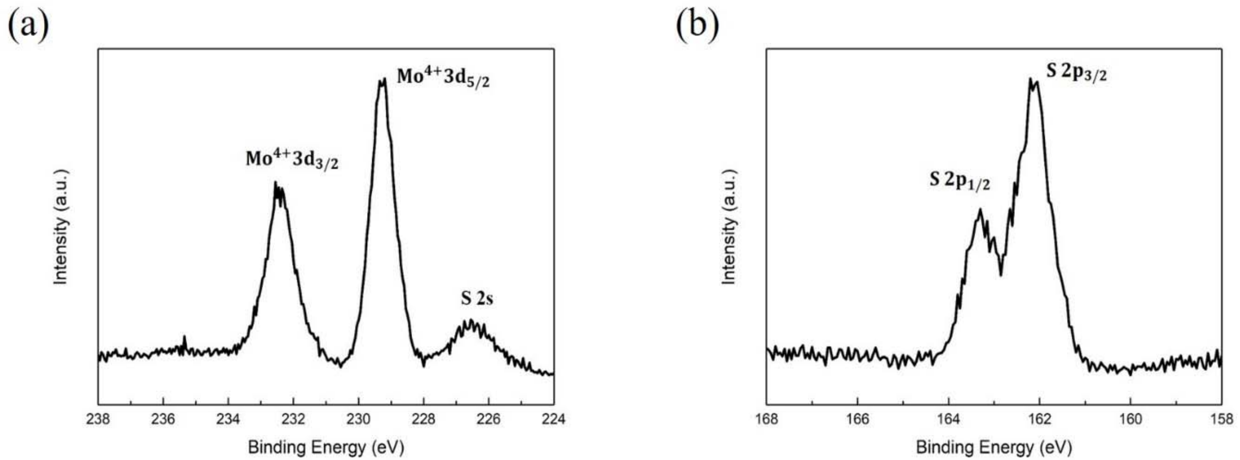

Fig. 3.10 X-ray photoelectron spectroscopy for (a) Mo (b) S

3.5.2 Stability of MoS_2 in Air

For electronic application, the stability of a material has a great impact on its reliability. Especially for 2D materials, a large surface area to volume ratio makes this issue more crucial in ambient environment. For further investigation of this phenomenon, we use Raman and XPS analysis to study this problem. Fig. 3.11 (a) shows the Raman spectra of the monolayer and bulk MoS_2, it was found that a small peak appears around 450 cm^{-1} on monolayer MoS_2, providing a supportive evidence for oxygen contaminated surface. The Raman peak at 440 cm^{-1} can be ascribed to Mo-S vibrations for oxysulfide species[70]. Oxygen may attack S–Mo–S bonds. However, It shows little peak in bulk MoS_2. It indicates that oxygen is only able to attack only surface layers rather than inner layer.

doi:10.6342/NTU201800956

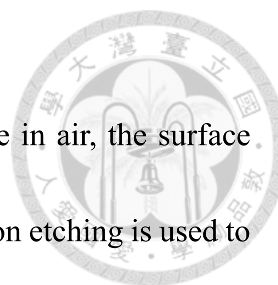

In order to confirm the oxygen adsorption on the MoS_2 surface in air, the surface analysis of the exfoliated MoS_2 by XPS was also utilized. An argon ion etching is used to etch the MoS_2 surface to investigate the inner part of MoS_2. Fig 3.11 (b) shows the surface oxygen scan before and after argon ion etching for 5 sec. A broad peak near 532 eV was detected before ion etching, which could be partially assigned to absorbed oxygen or water molecules. The oxygen signal was almost eliminated after argon ion etching. Therefore, it should be noted that the oxygen layer was only in the surface rather than in the inner layer. This p type doping was reported in many research due to heavily physical adsorption oxygen[71, 72].

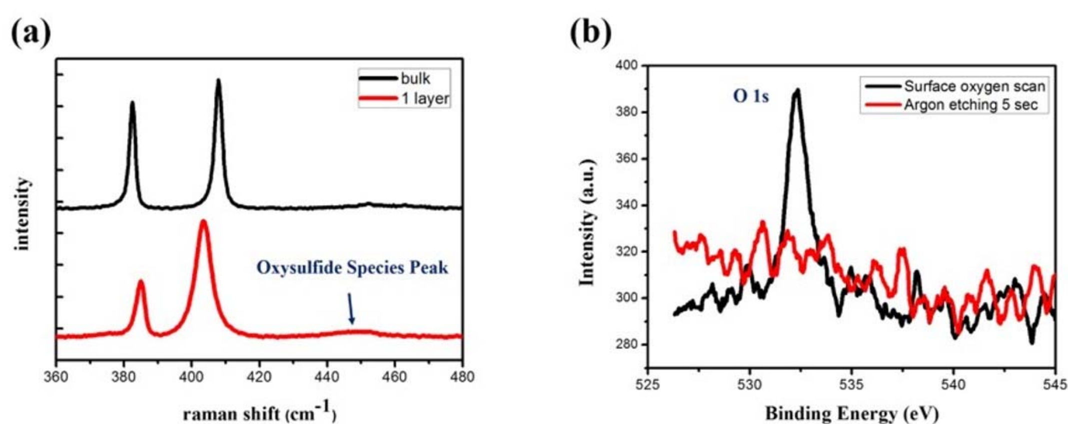

Fig. 3.11 (a) Raman Spectra for monolayer and bulk MoS_2,respectively. (b) XPS profile of the oxygen intensity at surface and inner MoS_2.

doi:10.6342/NTU201800956

3.5.3 Material Analysis of RIE doped MoS_2

In this section, we will use Reactive ion etching(RIE) as a plasma source to dope the bulk MoS_2 material. Here, we will choose CHF_3 gas for p-type plasma doping and the RF power is 100W, the camber pressure is 1.3pa and the gas flow rate is 10sccm during the plasma doping process.

Fig. 3.12 (a), (b), (c) display the XPS spectra of Mo 3d, F 1s and O 1s peaks before and after plasma treatment (doping time is 30s and 60s, respectively). After the plasma treatment, Mo 3d peaks shift to lower binding energy. This downshift of the peaks can be attributed to the p-doping effect because it caused the Fermi level shift toward the valence band edge and it shift about 0.4eV after plasma treatment. However, the Fermi level shift would not depend on the doping time. It shifts 0.4eV for both doping 30s and 60s.

To further identify the plasma treatment method, Fig. 3.12 (b) showed the F 1s peak before and after plasma treatment. F-related peak appeared for both 30s and 60s plasma treatment while it had no peaks on the untreated bulk MoS_2. It indicated that F-contained particles are absorbed onto the MoS_2 surface. In Fig. 3.12 (a), there is a new peak which is around 235eV and it corresponded to the Mo^{6+} signal as shown in Fig. 3.12 (d)[73]. At the same time, there is also a new O-related peak shown in Fig. 3.12 (c) after 30s and 60s plasma treatment. It may be caused by the oxidation of MoS_2 surface since the direct

doi:10.6342/NTU201800956

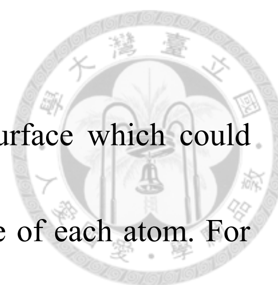

plasma attack give rise to the damage and defect on the MoS_2 surface which could accelerate the oxidation process. XPS can also know the percentage of each atom. For 30s plasma treatment, the percentage of F and O atoms are 19.9% and 21.0% respectively. For 60s, the percentage of F and O atoms are 23.5% and 20.4% respectively. Because the percentage of F and O atoms, which would induce the positive charge in the lower layer of MoS_2 film and cause p-type doping, are almost the same for both doping 30s and 60s, the Fermi level shift is the same for both doping 30s and 60s as mentioned in the previous paragraph.

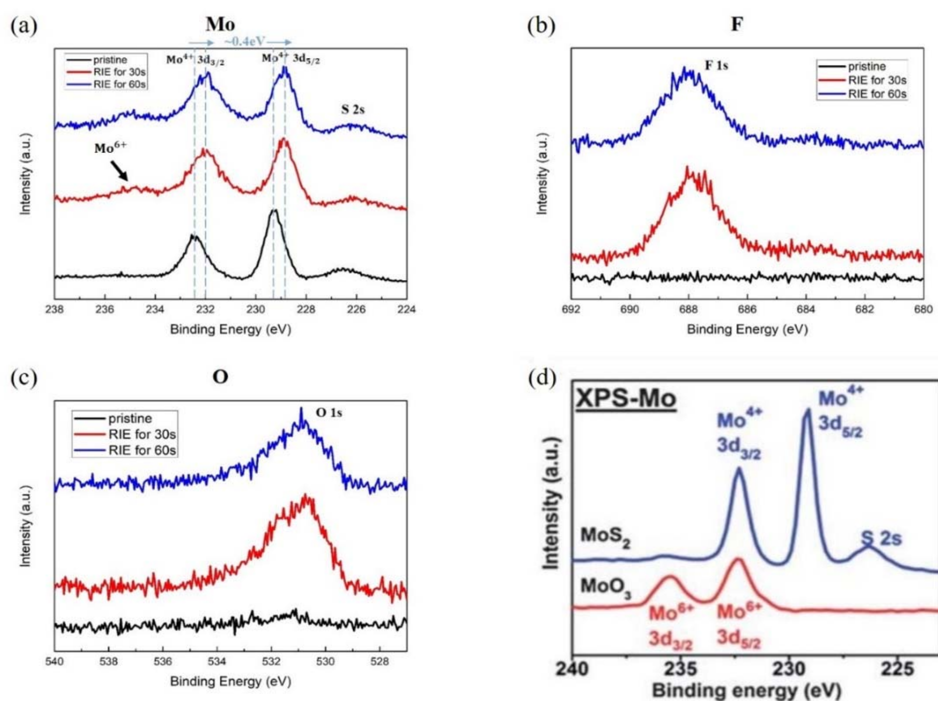

Fig. 3.12 The XPS spectra for (a) Mo 3d (b) F 1s (c) O 1s binding energy before and after plasma treatment. (d) The reported[73] XPS for Mo binding energy in the MoS_2 and MoO_3.

doi:10.6342/NTU201800956

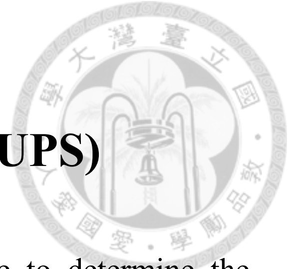

3.6 Ultraviolet photoelectron spectroscopy(UPS)

Ultraviolet photoelectron spectroscopy is an useful technique to determine the electronic state of the surface region of semiconductor a sample. Comparing to XPS, it is also measured in high vacuum (~1×10^{8} torr) to reduce environmental contamination. In order to explain how UPS works, the band diagram of a unknown material, the density of valence states and UPS spectrum is shown in Fig. 3.13. When ultraviolet radiation with a photon energy of 10~45 eV is used, the electrons at valence levels emit. The electrons are called secondary electrons (SE). With its <50 eV photon energy, it can only excite electrons at valence states while the XPS with its 200~2000 eV photon energy can excite the electrons in the core levels. In UPS, electrons emit from valence states to vacuum level follows the equations bellow.

$$E_{binding} = E_{photon} - (E_{kinctic} + \phi) \tag{3.2}$$

Where $E_{binding}$ is the binding energy of the electron from Fermi-level, E_{photon} is the energy of the UV, $E_{kinetic}$ is the kinetic energy of the electron and ϕ is the work function of the material. The kinetic energy of electrons which emit from valence states can be detected by UPS detector. When electrons come from deeper valence states, the kinetic energy becomes smaller. Therefore, the kinetic energy of electrons of the deepest valence states can be zero and this position is called secondary electron edge (SEE). According to the

doi:10.6342/NTU201800956

equation, the work function can be extracted from SEE.

$$\phi = E_{photon} - \mathrm{E}_{binding} \qquad \text{where} \quad E_{kinctic} = 0 \tag{3.3}$$

On the other hand, electrons emit from valence band maximum have the largest kinetic energy. Through UPS analysis, the binding energy between valence band maximum and Fermi-level can be extracted.

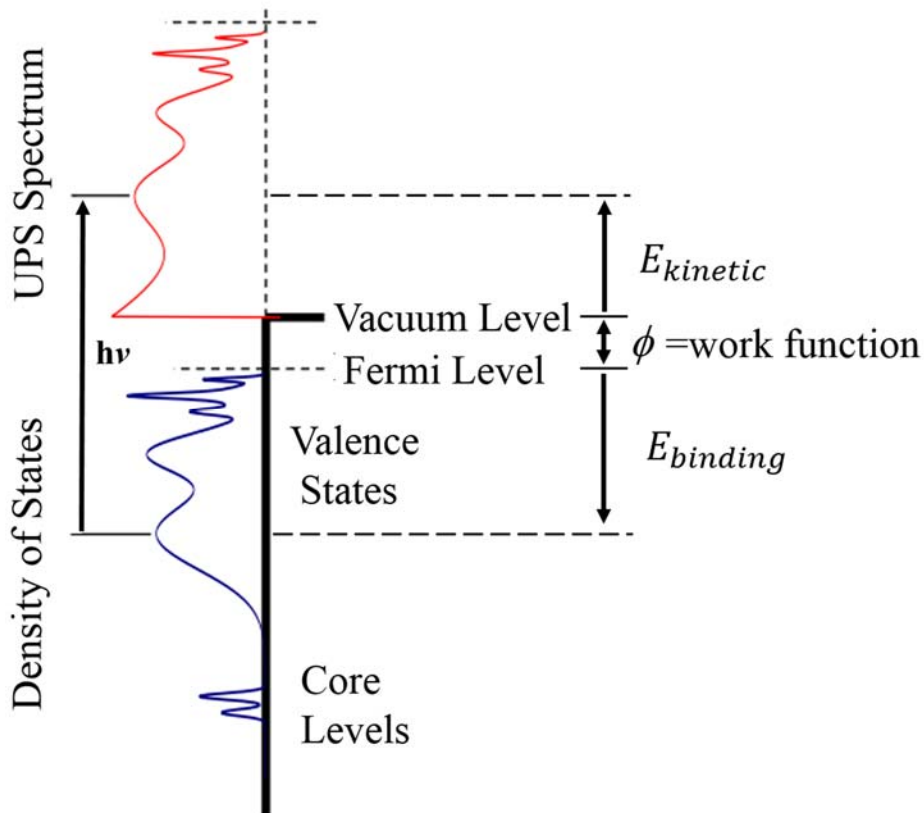

Fig. 3.13 Band diagram of an unknown material.

doi:10.6342/NTU201800956

3.6.1 Work Function of MoS_2

The UPS spectrum of MoS_2 is shown in Fig. 3.14 (a). To further investigate the spectrum, we fit the lines to extract binding energy for the zero and maximum kinetic energy of emitted electrons which are shown in Fig. 3.14 (b) and Fig. 3.14(c). In Fig 3.14 (b), the binding energy which corresponds to the secondary electron edge (SEE) is 16.7 eV. From the SEE at which the kinetic energy of emitted electron is zero, the work function of bulk MoS_2 can be calculated to be 4.45eV. In Fig. 3.14 (c), we can extract the smallest binding energy which means these electrons are emitted from the valence band maximum. Therefore, the energy between valence band maximum and Fermi-level is 1.2 eV. Because bulk MoS_2 has an indirect bandgap about 1.3 eV[16], the Fermi-level is close to the conduction band with about 0.1 eV energy difference that indicates the n-type characteristic of MoS_2 layer. And the band diagram of bulk MoS_2 is shown in Fig. 3.15.

Work function = (photon energy of He-I lamp radiation) – (binding energy of SEE)

ϕ =21.2eV – 16.75 eV = 4.45 eV

doi:10.6342/NTU201800956

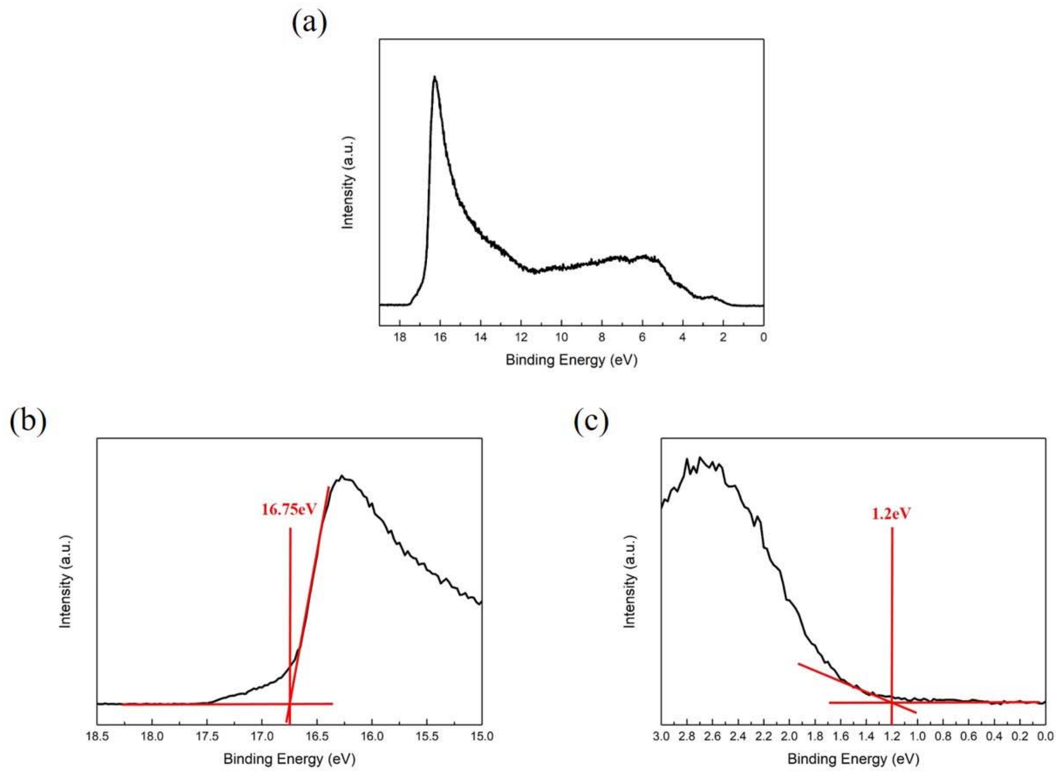

Fig. 3.14 (a), (b) and (c) UPS spectra of pristine MoS_2

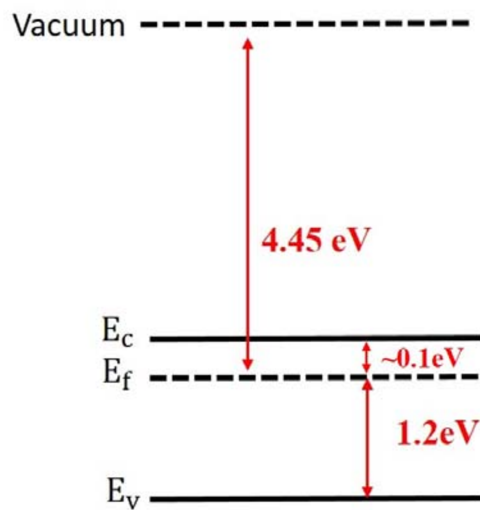

Fig. 3.15 Band diagram of bulk MoS_2

doi:10.6342/NTU201800956

3.6.2 Material Analysis of RIE doped MoS_2

In this section, we will use the same sample as mentioned in Sec. 3.5.3 but using UPS to analyze the work function difference before and after RIE doping.

In Fig. 3.16 (a) and (b), the binding energy which corresponds to the secondary electron edge (SEE) of plasma treatment MoS_2 for 30s and 60s are 16.6 eV and 16.48 eV respectively. Therefore, we can calculate the work function is 4.6 eV and 4.72 eV respectively. In Sec. 3.5.3, we know that the Fermi level shift either for 30s or 60s plasma treatment MoS_2 are 0.4 eV. However, the increased work function is 0.15 eV and 0.27 eV respectively rather than 0.4 eV. It is because that the MoS_2 will easily absorb the carbon in the atmosphere after plasma treatment. The information that we can acquire from the UPS is just in the sample surface about 1-3nm. Therefore, the carbon which is absorbed on the MoS_2 surface would influence the measurement of UPS and let the vacuum level shift to the conduction band as shown in Fig. 3.17.

doi:10.6342/NTU201800956

國立臺灣大學

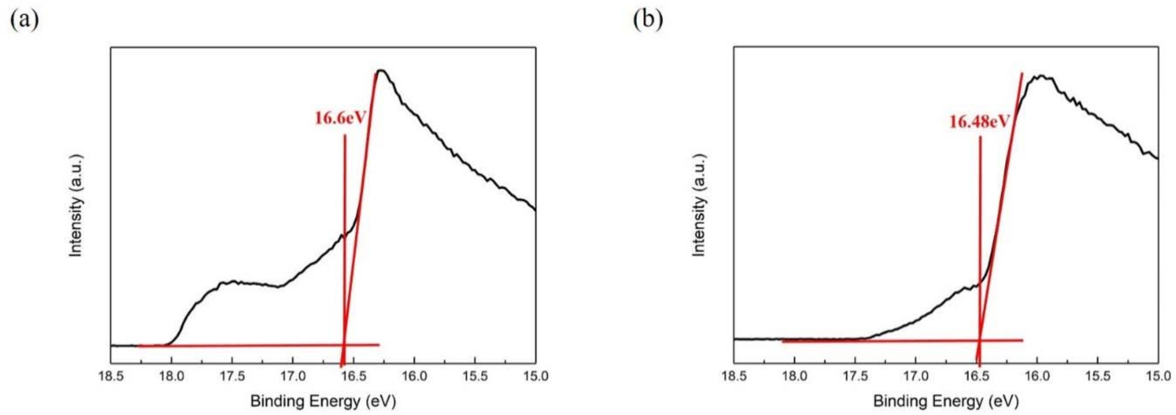

Fig. 3.16 UPS spectra for (a) 30s (b) 60s plasma treatment

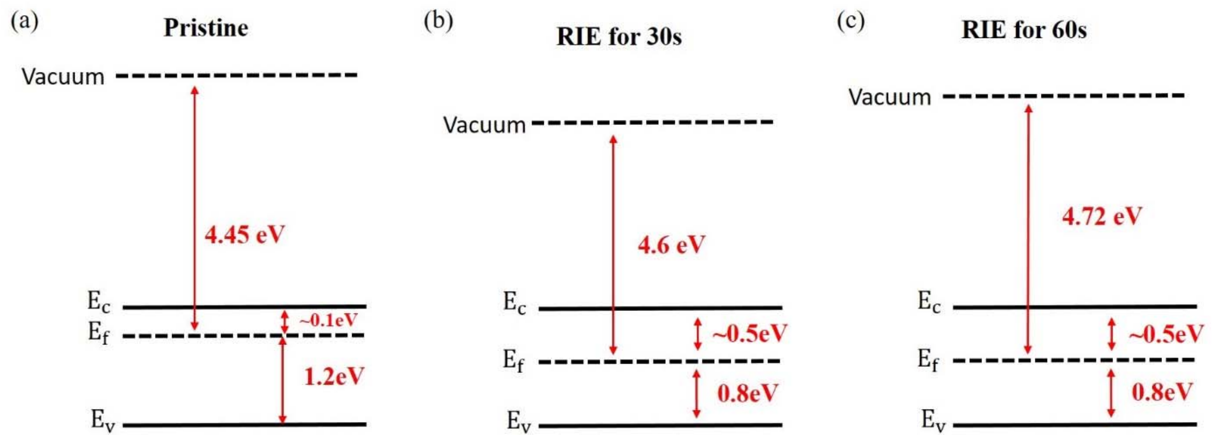

Fig. 3.17 The band diagram of (a) pristine (b) plasma treatment for 30s (c) plasma treatment for 60s MoS_2.

doi:10.6342/NTU201800956

Chpater 4 MoS_2 Thin Film Transistors

In this chapter, the fabrication processes and the electronic properties of back-gated MoS_2 TFT will be first described. Then, SiO_2 substrate will be replaced by h-BN substrate in order to improve the mobility and reduce the hysteresis. The same MoS_2 flake with and without h-BN as a bottom gate would be fabricated to compare the properties of these two TFTs on the different substrate. Finally, the MoS_2 rectify diode and MoS_2-Black Phosphorus n-p heterojunction was fabricated and theirs electronic and optical properties will be measured and discussed.

4.1 MoS_2 Back-gated TFTs using SiO_2 Substrate

In this section, the fabrication processes and the electronic properties of MoS_2 back-gated TFT using SiO_2 substrate will be described.

4.1.1 Device Process Flow

Because it is very hard to locate the position of the chosen flake on the substrate during the processing steps of the devices. Therefore, a two-digit number system was used to define our pattern on the 300nm SiO_2/p^{++} Si substrate by photolithography followed by thermal evaporation of Cr (5nm)/Au (80nm) contact metal and lift off process,

doi:10.6342/NTU201800956

as shown in Fig. 4.1. The process flow of the fabrication process for the MoS_2 TFT are shown in Fig. 4.2. First, the MoS_2 flakes was exfoliated onto the patterned substrate as described in Sec. 3.1 and 3.2 by scotch tape. The heavily doped silicon substrate with 300nm thick SiO_2 on top serves as the bottom gate and oxide insulator of our device. Then, the MoS_2 flakes were located based on their optical contrast with respect to the underlying SiO_2 layer. An appropriate flake was chosen with a proper thickness under optical microscope. In order to remove any possible contamination and residue in above process, an hour acetone immersion was used to remove any organic residues after exfoliation. Next, E-beam lithography was used to defined the source and drain, followed by thermal evaporation of Cr (5nm)/ Au (80nm) contact metal and lift off process. Chromium of 5nm thickness was necessary for the adhesion layer because of poor attachment of gold on oxide. The cross section and top views of the MoS_2 TFT are shown in Fig. 4.3(a) and (b).

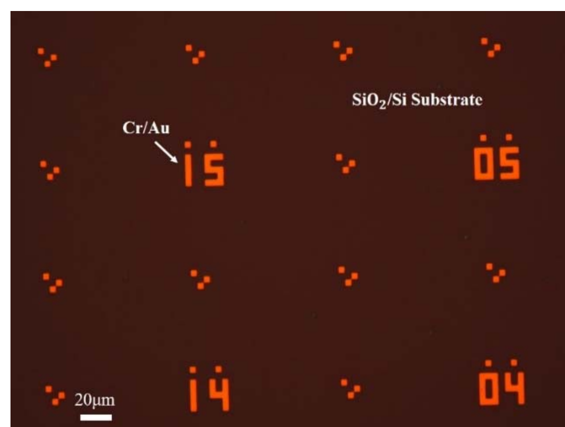

Fig. 4.1 Patterned Substrate

doi:10.6342/NTU201800956

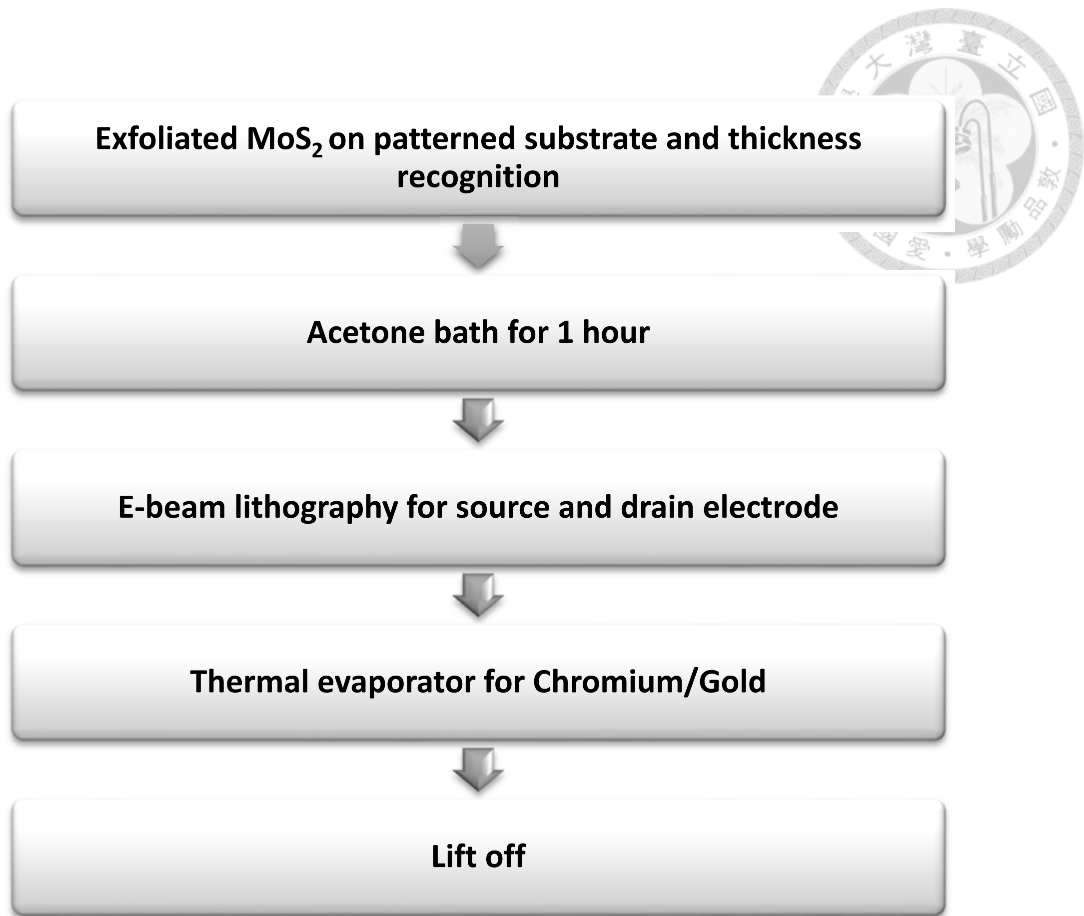

Fig. 4.2 The flow chart for back-gated MoS_2 TFT fabrication process.

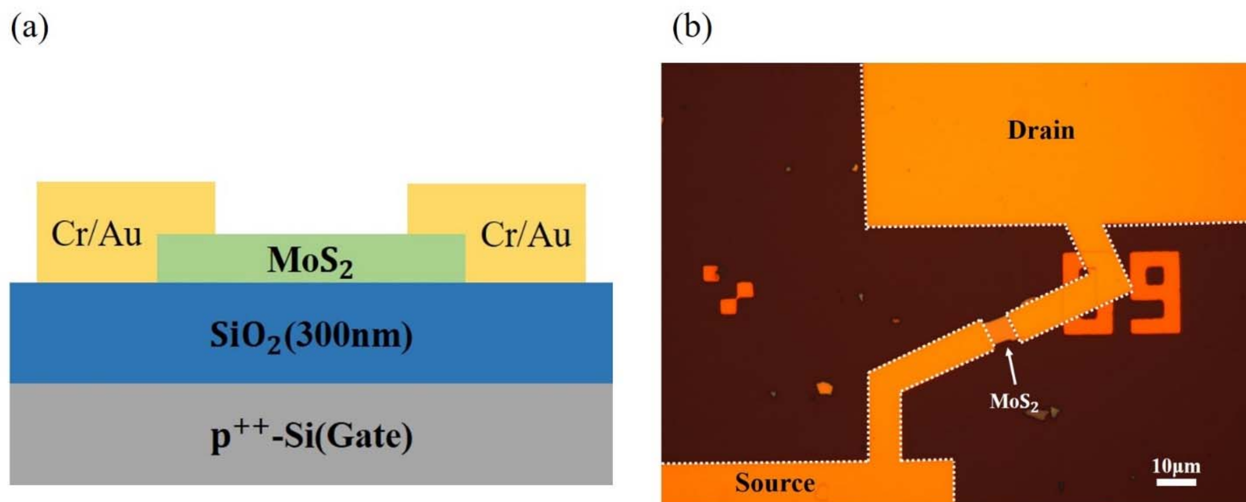

Fig. 4.3 (a) Cross-section view of device structure. (b) Top view of MoS_2 TFT under optical microscopy.

doi:10.6342/NTU201800956

4.1.2 Device Performance

Fig. 4.4 (a) and (b) display the AFM image and thickness of the MoS_2 flake which is fabricated on the SiO_2 substrate as a MoS_2 TFT. The thickness of MoS_2 flake is 33nm and the surface is pretty flat. Fig. 4.5 (a) and (b) show the device performance. In Fig. 4.5 (a), a typical ohmic contact behavior in the drain current-drain voltage (I_d-V_d) output characteristics of MoS_2 TFT is observed. As the gate voltage (V_g) increases, the drain current I_d becomes larger. It is because MoS_2 layer has n-type characteristics. The transfer drain current versus gate voltage characteristics of the MoS_2 TFT is shown in Fig. 4.5 (b). In order to identify the hysteresis of the MoS_2 TFT, the measurement of transfer characteristics was carried out from the negative to the positive gate voltage (forward sweep), and immediately from the positive to the negative gate voltage (reverse sweep). The sweep direction was shown in the black (semi-log scale) and red (linear scale) arrow in Fig. 4.5 (b). From Fig. 4.5 (b), it can extract the on/off current ratio of MoS_2 TFT which is up to 4×10^7. This property is lacking in most graphene FETs due to its zero band gap. The subthreshold swing is 0.94 V/dec. The field effect mobility is about 44.7 cm^2/V-sec which can be extracted from the transconductance of linear region by using Eq. (4.1).

$$\mu_{EF} = \frac{g_m}{C_i \frac{W}{L} V_d} \quad (4.1)$$

doi:10.6342/NTU201800956

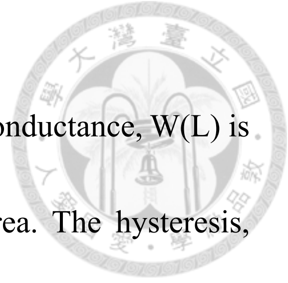

Where μ_{EF} is the field effect mobility of the TFT, g_m is the transconductance, W(L) is the channel width (length), and C_i is the capacitance per unit area. The hysteresis, defined as the threshold voltage shift during the forward sweep and reverse sweep, is 62.2V. However, the hysteresis is not desirable for logic switching applications because it will increase the on/off switching voltage, thereby increasing the power consumption of the circuit. Therefore, h-BN was used to replace SiO_2 as a substrate for MoS_2 TFT to lower the hysteresis which will be shown in Sec. 4.2. Table 4.1 summarizes the performance of MoS_2 TFT using SiO_2 substrate.

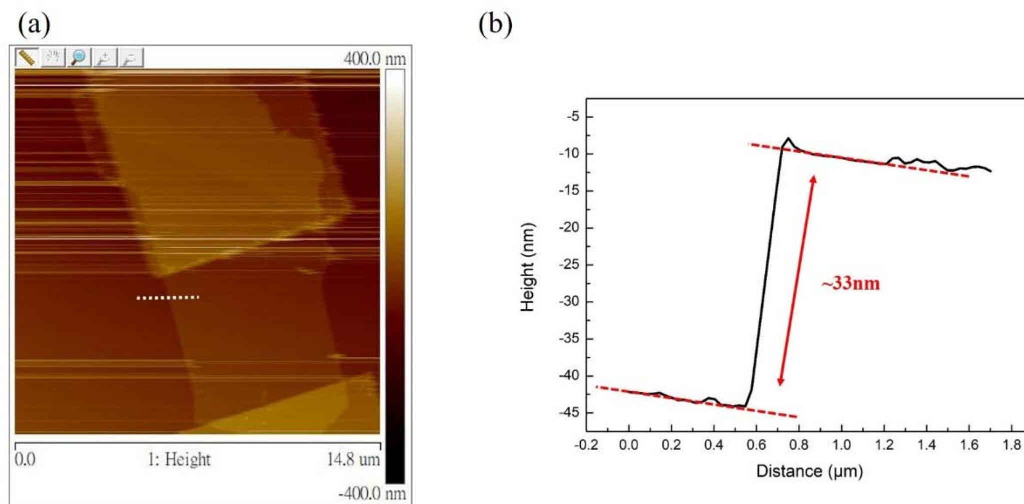

Fig. 4.4 (a) top view of MoS_2 TFT under AFM. (b) The thickness of the MoS_2 flake measured by AFM.

doi:10.6342/NTU201800956

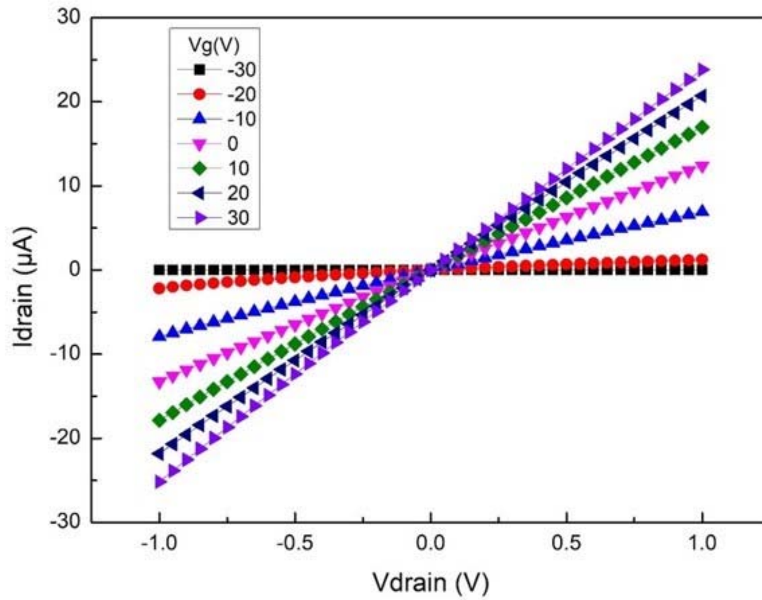

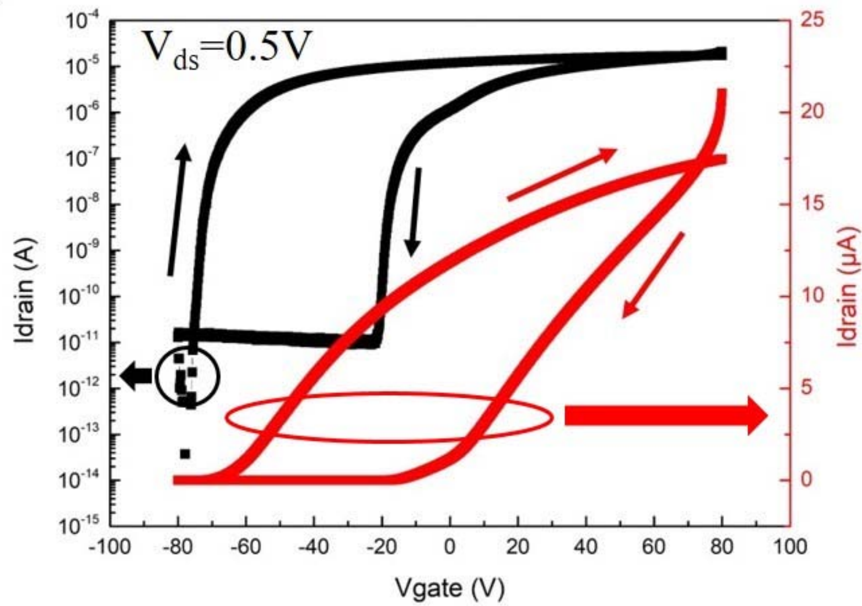

Fig. 4.5 The characteristics of SiO_2 substrate MoS_2 TFT (a) I_d versus V_d characteristics. (b) I_d versus V_g curves in log and linear scale.

doi:10.6342/NTU201800956

Table 4.1 Summary of MoS_2 TFT using SiO_2 substrate

Field Effect Mobility	44.7 $cm^2/V\text{-}s$
Drain Bias(V_{ds})	0.5 V
On/off ratio	4×10^7
Subthreshold Swing	0.94 V/dec
Hysteresis	62.2 V
W/L	5.5 μm/5.8 μm

doi:10.6342/NTU201800956

4.2 MoS_2 Back-gated TFTs using h-BN Substrate

In order to enhance the mobility and lower the hysteresis of the MoS_2 back-gated TFT as mentioned in previous section, the hexagonal boron nitride (h-BN) was used as a back-gated substrate to reduce the interface trap and impurities density between MoS_2 and SiO_2 layer. So in this section, MoS_2 back-gated TFT using h-BN substrate will be fabricated, and the electronic properties will be measured and discussed.

4.2.1 Device Process Flow

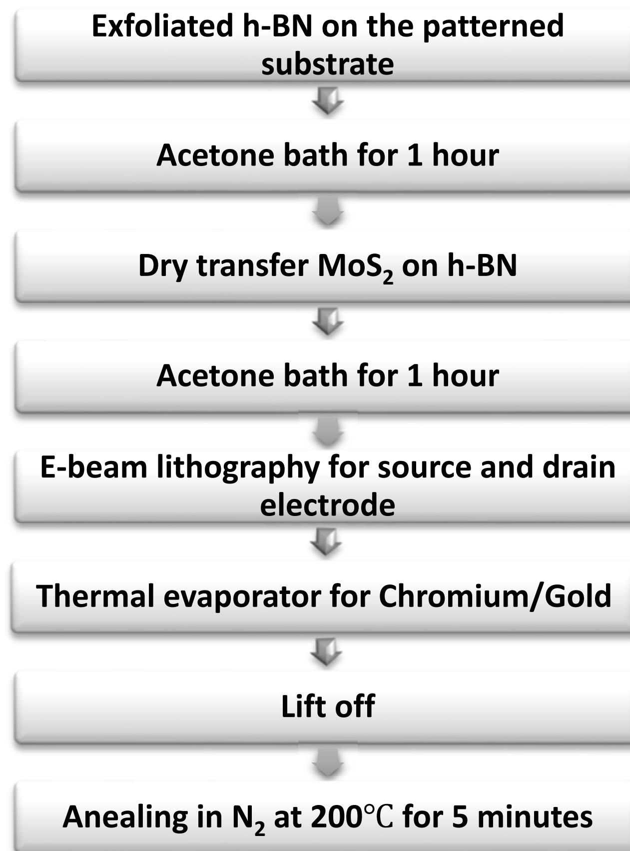

Fig. 4.6 The flow chart for MoS_2 back-gated TFT using h-BN substrate.

doi:10.6342/NTU201800956

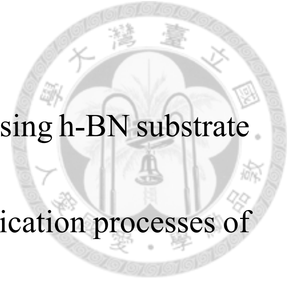

The process flow of the fabrication processes for the MoS_2 TFT using h-BN substrate is shown in Fig. 4.6. Fig. 4.7 illustrates the schematic flow of the fabrication processes of our device. The h-BN flakes were mechanically exfoliated by scotch-tape technique and transferred to a patterned 300nm SiO_2/p^{++} Si substrate as shown in Fig. 4.1. After bath acetone for one hour, MoS_2 flake was transferred on the top of h-BN by PDMS stamping as mentioned in section 2.1. After second bath acetone for one hour, the source and drain would be defined by E-beam lithography followed by thermal evaporation of Cr (5nm)/Au (80nm) contact metal and lift off process. Finally, the device was annealed at 200℃ for 5 minutes in N_2 to have better contact between MoS_2 and h-BN. Fig. 4.8 shows the completed devices under optical microscopy.

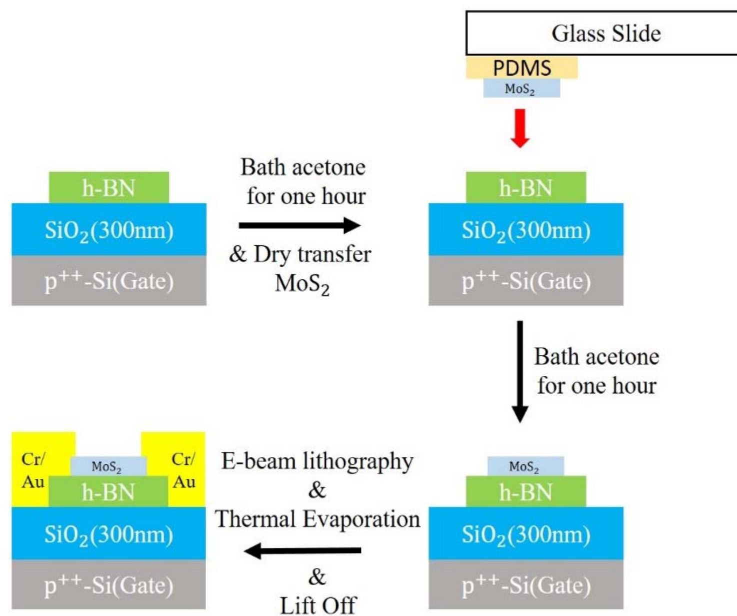

Fig. 4.7 Schematic flow of the fabrication process of h-BN substrate TFT.

doi:10.6342/NTU201800956

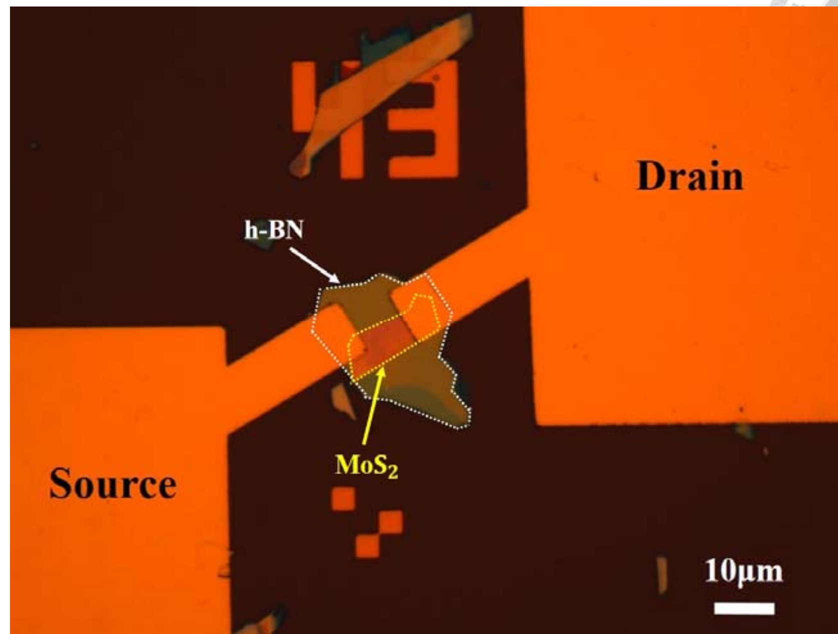

Fig. 4.8 Top view of h-BN substrate TFT under optical microscopy.

Before measurement, Raman spectroscopy is used to double check our device. Fig. 4.9 displays the Raman spectra of h-BN substrate MoS_2 TFT, peaks at 382.4 cm^{-1} and 407.9 cm^{-1} are the E^1_{2g} and A_{1g} for MoS_2, and peaks at 1362 cm^{-1} is the signal of h-BN.

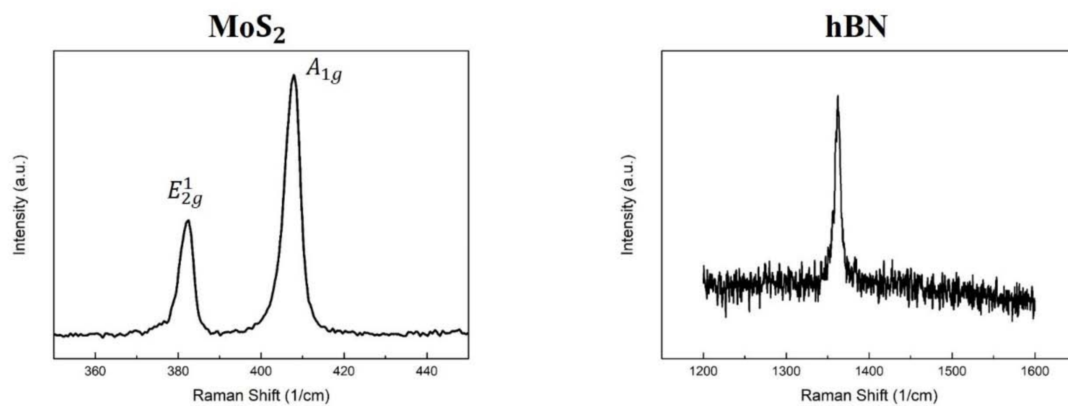

Fig. 4.9 Raman spectra of h-BN substrate MoS_2 TFT.

doi:10.6342/NTU201800956

4.2.2 Device Performance

Fig. 4.10 (a) shows the I_d-V_d output characteristics of MoS_2 TFT and it shows that it is a typical ohmic contact behavior. The transfer drain current versus gate voltage characteristics of MoS_2 TFT is shown in Fig. 4.10 (b). The output current on/off ratio is 9×10^6, subthreshold swing is 1.4 V/dec and the hysteresis is 5V. Field effect mobility can obtain from the Eq. (4.1). In previous calculation, C_i is 1.15×10^{-8} F/cm^2 for the 300nm SiO_2 substrate. However, we use the additional h-BN layer as an oxide layer. Therefore, C_i should become the total capacitance of SiO_2 and h-BN in series. In order to calculate the capacitance of h-BN, the thickness of h-BN flake is measured by AFM as shown in Fig. 4.11 and its thickness is 68nm. According to the capacitance per unit area equation $C = \frac{\varepsilon_r \varepsilon_0}{d}$, where ε_r is the dielectric constant which is 3 for h-BN[74], ε_0 is the vacuum permittivity constant which is 8.85×10^{-14} F/cm and d is the thickness of h-BN flake which is 68nm. Therefore, the total capacitance of SiO_2 and h-BN in series are 8.88×10^{-9} F/cm^2 and the field effect mobility extracted from the linear region of I_d-V_g plot is 117 cm^2/V-sec which is close to the best reported value 116 cm^2/V-sec of MoS_2 TFT[75]. It is obvious that it can improve the mobility from 44.7 cm^2/V-sec to 117 cm^2/V-sec and reduce the hysteresis form 62.2V to 5V of MoS_2 TFT by using h-BN as a substrate. Table 4.2 summarizes the performance of MoS_2 TFT using h-BN substrate.

doi:10.6342/NTU201800956

(a)

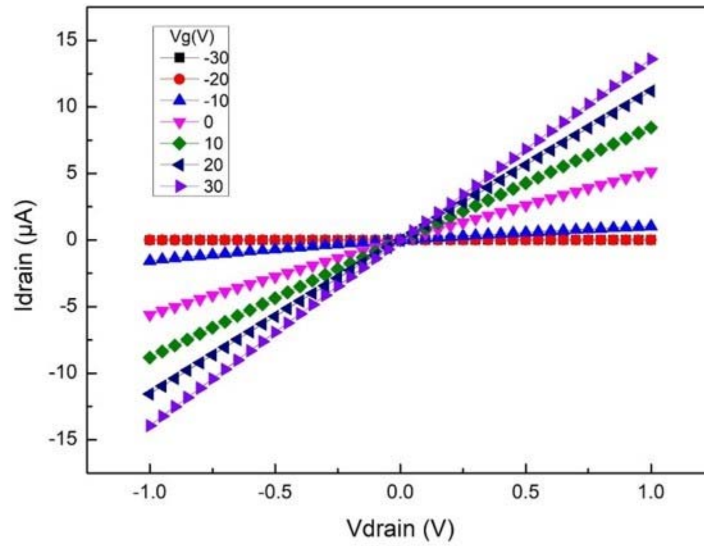

(b)

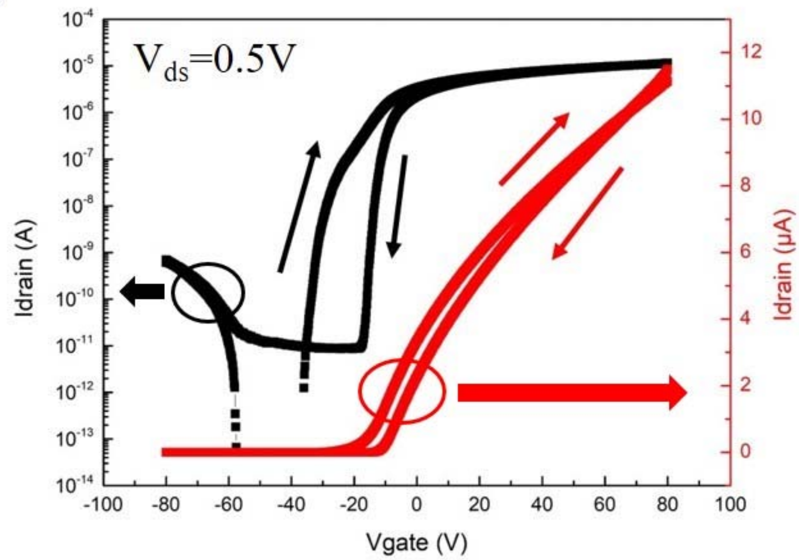

Fig. 4.10 The characteristics of h-BN substrate MoS_2 TFT (a) I_d versus V_d (b) I_d versus V_g curves in log and linear scale.

doi:10.6342/NTU201800956

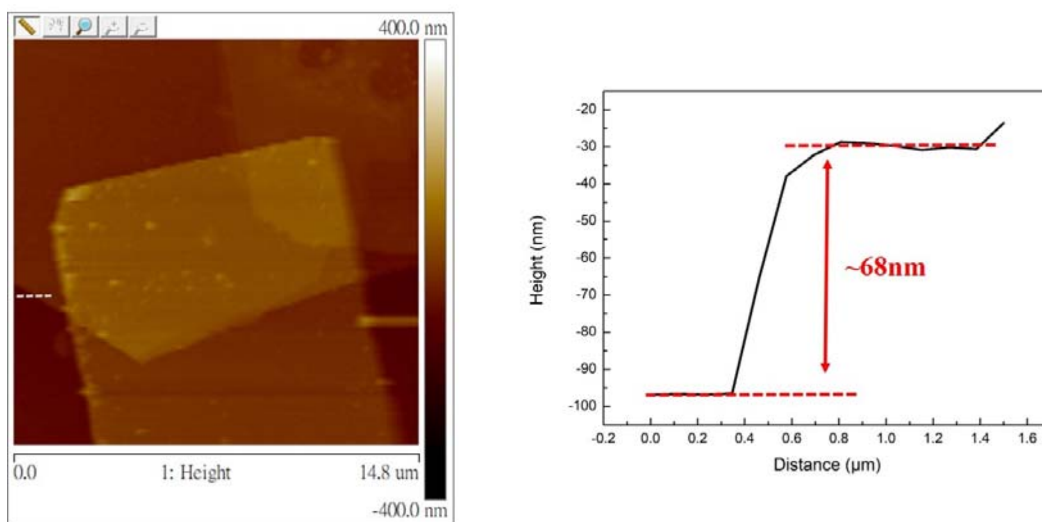

Fig. 4.11 AFM image for the thickness of h-BN.

Table 4.2 Summary of h-BN substrate back-gated MoS_2 TFT

Field Effect Mobility	117 cm^2/V-s
Drain Bias(V_{ds})	0.5 V
On/off ratio	9×10^6
Subthreshold Swing	1.4 V/dec
Hysteresis	5 V
W/L	3.3 μm/7.7 μm

doi:10.6342/NTU201800956

4.3 Comparison between SiO_2 and h-BN Substrate

In previous section, although it shows that TFT using h-BN substrate has better device performance (mobility and hysteresis) than that using SiO_2 substrate, the device performance will be influenced by many different factors. Therefore, two MoS_2 TFTs with the same MoS_2 flake but with and without h-BN substrate were fabricated. In this way, it can ensure these two TFTs have nearly the same thickness of MoS_2 and undergoing the same fabrication processes.

4.3.1 Device Process Flow

The fabrication process flow is almost the same as mentioned in section 4.2.1. There is only one step different from the section 4.2.1 which is the dry transfer MoS_2 on h-BN. In section 4.2.1, the whole piece of MoS_2 flake was transferred on the h-BN as shown in Fig. 4.12 (a). In this section, in order to compare between SiO_2 and h-BN substrate, we will let half of the MoS_2 flake on the SiO_2 and the other half on the h-BN substrate as shown in Fig. 4.12 (b). Finally, Cr/Au (5nm/80nm) electrodes were patterned by E-beam lithography and thermal evaporation and lift off process. The cross section and top views of the TFT are shown in Fig. 4.13 (a) and (b), respectively. In Fig. 4.13 (b), electrodes 1 and 2 are the MoS_2 TFT on the SiO_2 substrate and electrodes 3 and 4 are the MoS_2 TFT

doi:10.6342/NTU201800956

on the h-BN substrate.

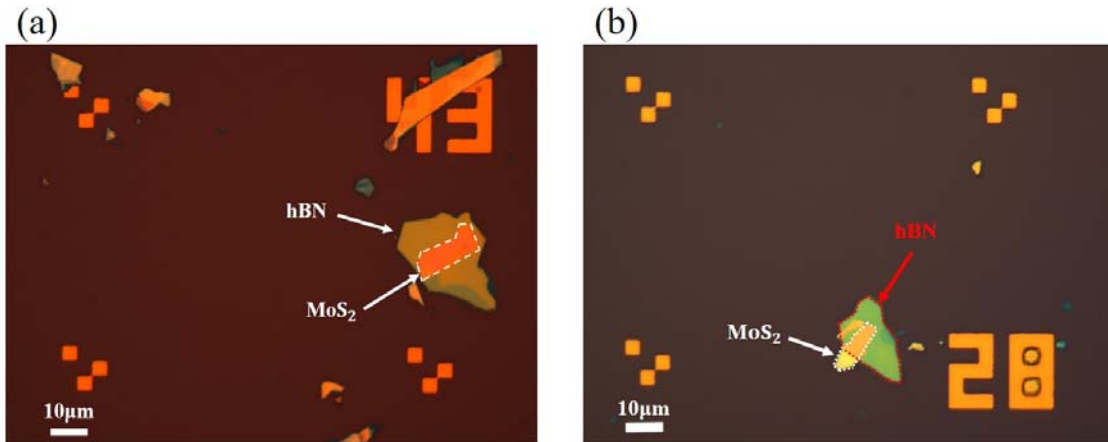

Fig. 4.12 MoS_2 and h-BN heterostructure with (a) The whole MoS_2 flake on the h-BN (b) half of MoS_2 flake on the h-BN under optical microscopy.

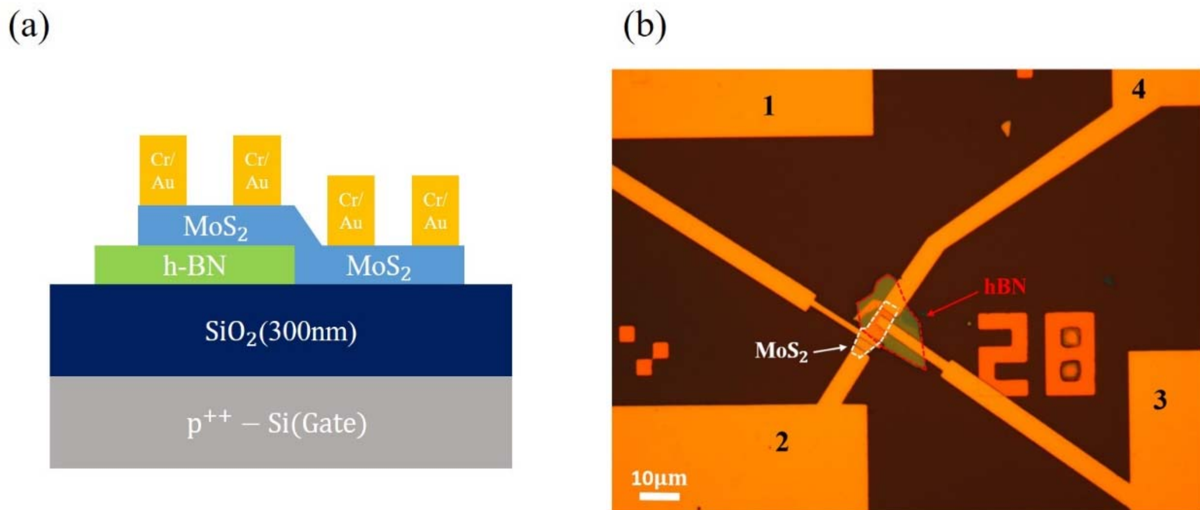

Fig. 4.13 (a)Cross-sectional view of device structure. (b) Top view of MoS_2 TFT under optical microscopy. Electrodes 1 and 2 are the TFT on SiO_2 substrate, whereas electrodes 3 and 4 are the TFT on h-BN substrate.

doi:10.6342/NTU201800956

4.3.2 Device Performance

Fig. 4.14 (a) and (b) shows the I_d-V_d plot of the SiO_2 (electrode 1 and 2) and h-BN (electrode 3 and 4) substrate MoS_2 TFT. Similar to the previous result, both of these two device have a typical ohmic contacts.

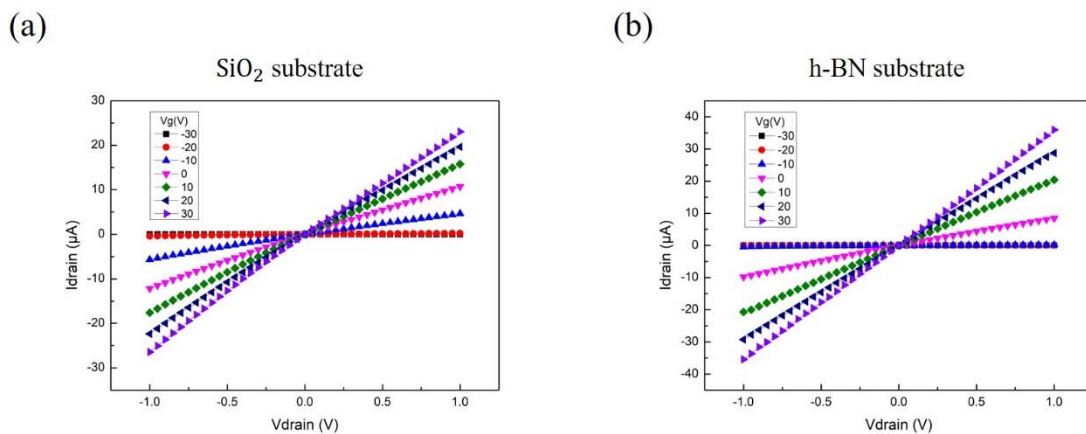

Fig. 4.14 I_d versus V_d characteristics of TFTs on the (a) SiO_2 substrate (b) h-BN substrate. They use the same MoS_2 flake.

Fig. 4.15 shows the thickness of the h-BN flake which is 50nm thick. Fig. 4.16 (a) and (b) show the I_d-V_g plot of TFTs on SiO_2 and h-BN substrate, respectively. Form these plot, it can extract on/off current ratio which is 8×10^7 for TFT on SiO_2 substrate and 2×10^6 for TFT on h-BN substrate. The subthreshold swing is 1.61 V/dec for TFT on SiO_2 substrate and 1.85 V/dec for TFT on h-BN substrate. Because the capacitance of TFT on h-BN substrate is smaller than that on SiO_2 substrate, TFT on h-BN substrate has

doi:10.6342/NTU201800956

poorer gate control so that it has poorer on/off current ratio and subthreshold swing than that on SiO_2 substrate. However, TFT on h-BN substrate TFT has larger mobility and lower hysteresis than that on SiO_2 substrate. The mobility is 21.0 cm^2/V-sec for TFT on SiO_2 substrate and 63.5 cm^2/V-sec for TFT on h-BN substrate. The hysteresis is 46.2 V for TFT on SiO_2 substrate and 0.16 V for TFT on h-BN substrate. It is because that h-BN has an atomically smooth surface that is relatively free of dangling bonds, charge traps and is naturally flat. Therefore, it has fewer interface trap density in the h-BN-MoS_2 interface than SiO_2-MoS_2 interface. Fewer interface trap not only reduce the carrier scattering rate which would enhance the mobility but let fewer charge trapped in the interface which would reduce the hysteresis. From this section, it proves that h-BN substrate can improve the mobility and reduce the hysteresis for MoS_2 TFT. Table 4.3 summarizes the performance of MoS_2 TFT using SiO_2 and h-BN substrate.

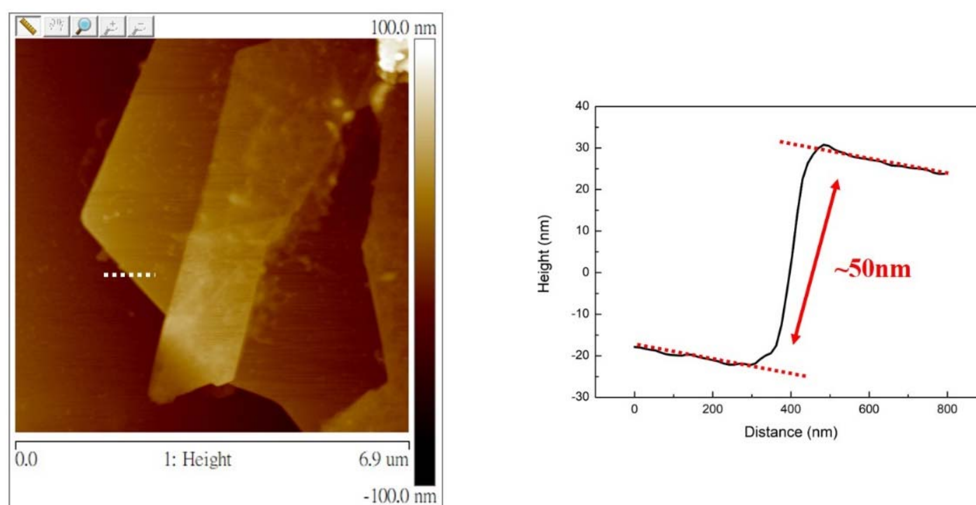

Fig. 4.15 AFM image for the thickness of h-BN.

doi:10.6342/NTU201800956

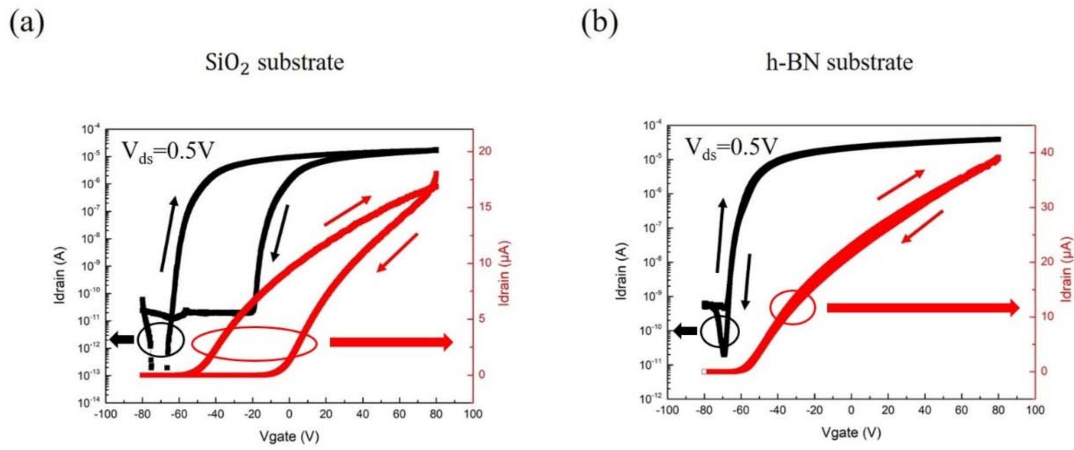

Fig. 4.16 I_d versus V_g characteristics of TFTs on the (a) SiO_2 substrate (b) h-BN substrate. They use the same MoS_2 flake.

Table 4.3 Summary of SiO_2 substrate and h-BN substrate MoS_2 TFTs

Substrate	SiO_2	h-BN
Field Effect Mobility	21.0 cm^2/V-s	63.5 cm^2/V-s
Drain Bias(V_{ds})	0.5 V	0.5 V
On/off ratio	8×10^7	2×10^6
Subthreshold Swing	1.61 V/dec	1.85 V/dec
Hysteresis	46.2 V	0.16 V
W/L	4.7 μm/2.3 μm	2.8 μm/1.5 μm

doi:10.6342/NTU201800956

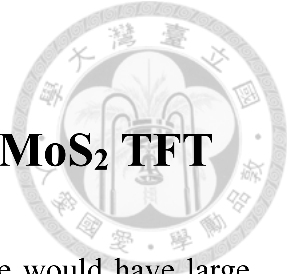

4.4 Discussion of hysteresis and stability of MoS_2 TFT

In previous section, it shows that MoS_2 TFT on SiO_2 substrate would have large hysteresis but it would be reduced by using h-BN substrate. In order to further discuss the mechanism of the hysteresis, we will compare the performance of TFTs among SiO_2 substrate in atmosphere, SiO_2 substrate in vacuum and h-BN substrate in atmosphere. Furthermore, the reliability of MoS_2 TFT is another important issue. Because of its large surface-to-volume ratio, it will easily absorb the molecules such as H_2O and O_2 in the atmosphere and being oxidized. In order to have better stability, we will use h-BN as a passivation layer to make it more stable in the atmosphere.

4.4.1 Hysteresis in MoS_2 back-gated TFTs

In Fig. 4.17 (a), both of the black and red line are the I_d-V_g characteristics of MoS_2 TFT on SiO_2 substrate and measure in the atmosphere. From Fig. 4.17(a), the hysteresis reduces from 57 V to 51 V after the device annealing in N_2 at 200℃. It is because annealing process can reduce the interface trap density between MoS_2 and SiO_2 layer but the effect is limited. In Fig. 4.17 (b), both of the red and blue line are the I_d-V_g characteristics of MoS_2 TFT on SiO_2 substrate after annealing in N_2 at 200℃. The red line is measured in atmosphere and the blue line is measured in vacuum (~0.1 torr). In

doi:10.6342/NTU201800956

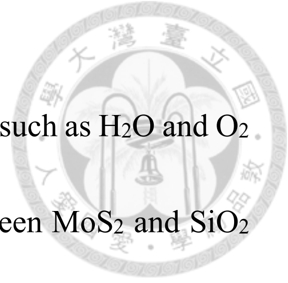

vacuum, the hysteresis was reduced from 51 V to 8 V. The molecules such as H_2O and O_2 which could be absorbed on the surface of MoS_2 and interface between MoS_2 and SiO_2 would be taken away in vacuum. However, as mentioned in section 4.3.2, the hysteresis of MoS_2 TFT which is measured in atmosphere is 0.16 V by using h-BN substrate. It can prove that the molecules such as H_2O and O_2 absorbed on the MoS_2 surface would not cause the hysteresis. Therefore, the molecules such as H_2O and O_2 absorbed between MoS_2 and SiO_2 would cause hysteresis and can be reduced by measuring in vacuum.

In summary, the interface property would influence the hysteresis seriously. By using annealing process and measuring in vacuum, it can improve the interface property between MoS_2 and SiO_2. However, the most effective method to improve interface is using h-BN substrate. The 2D to 2D interface can have better interface property and reduce the hysteresis.

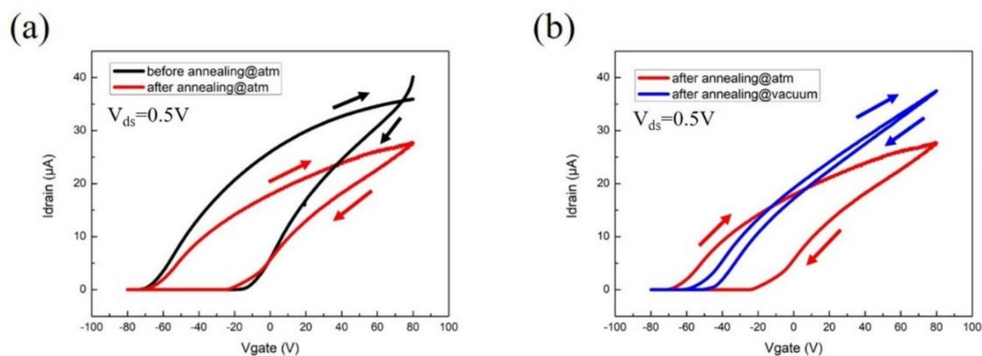

Fig. 4.17 Hysteresis in transfer characteristics of MoS_2 TFT on SiO_2 substrate (a) before and after annealing (b) after annealing but measure in atmosphere and vacuum(~0.1 torr).

doi:10.6342/NTU201800956

4.4.2 Stability in MoS_2 back-gated TFTs

Because MoS_2 film has large surface-to-volume ratio, it will easily adsorb the molecules such as H_2O and O_2 in the atmosphere and oxidize as mentioned in sec. 3.5.2. Because of the oxidation, the device performance will degrade after exposing in air for a long time. However, stability in air is very important for practical applications. In order to enhance the stability of MoS_2 TFT, we use h-BN as a passivation layer to protect the oxidation of MoS_2 film.

The device which the process flow is the same as mentioned in sec. 4.1.1 would be fabricated as shown in Fig. 4.18 (a). Then, the h-BN passivation layer would be transferred on the MoS_2 TFT by using dry transfer method as shown in Fig. 4.18 (b).

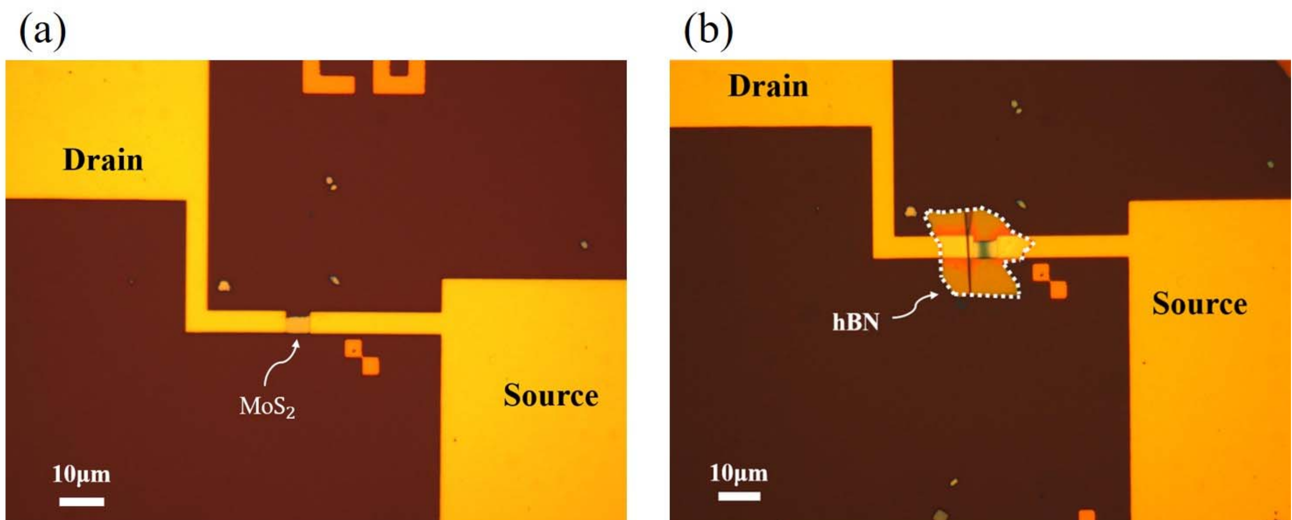

Fig. 4.18 MoS_2 back-gated TFT (a) without (b) with h-BN passivation layer.

doi:10.6342/NTU201800956

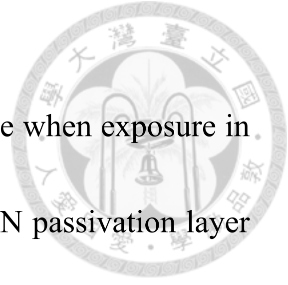

Fig. 4.19 (a), (b) and (c) show the variety of device performance when exposure in air for 28 days. Although the mobility of both with and without h-BN passivation layer would degrade after exposure in air for 28 days, the on/off ratio and subthreshold swing show the device with h-BN passivation layer has better stability than without h-BN passivation layer. For the device with h-BN passivation layer, the on/off ratio still has near 5 orders of magnitude and subthreshold swing remains around 1 V/dec after exposure in air for 28 days. In contrast, the transistor characteristics of the device without h-BN passivation layer is almost disappeared (on/off ratio $< 10^1$ and SS=385 V/dec). Therefore, it can substantially enhance the stability by using h-BN passivation layer.

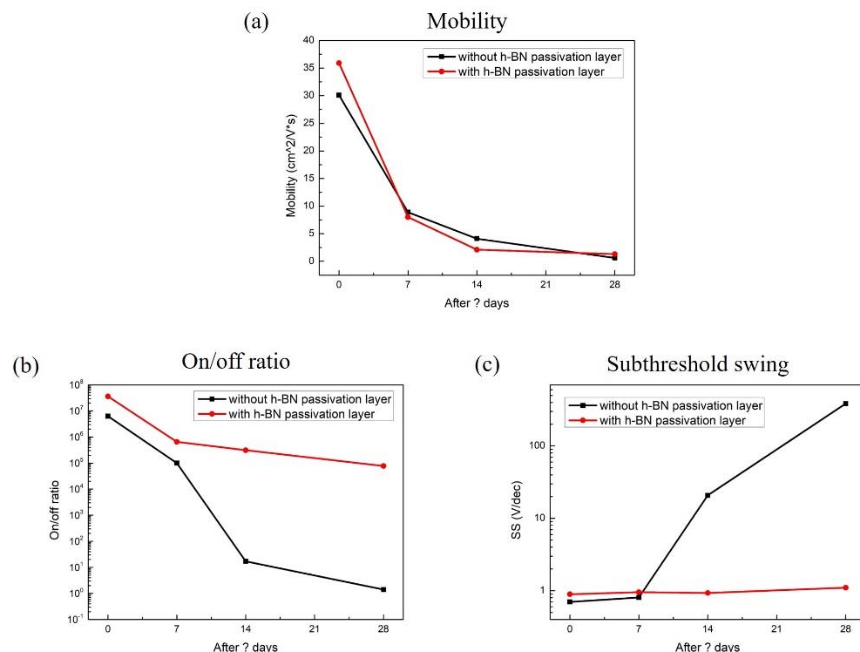

Fig. 4.19 The variety of (a) mobility (b) on/off ratio (c) subthreshold swing after MoS_2 TFTs exposure in air for 28 days.

doi:10.6342/NTU201800956

4.5 MoS_2 p-n rectifying diode

In Sec. 3.5.3, it is indicated that RIE can be used to dope the MoS_2 film to p-type material. Because the pristine MoS_2 film has n-type characteristics, RIE can be applied to generate the p region which can be combined with the pristine MoS_2 (n region) to make the MoS_2 p-n rectifying diode. Its electronic and optical properties would also be measured and discussed in this section.

4.5.1 Device Process Flow

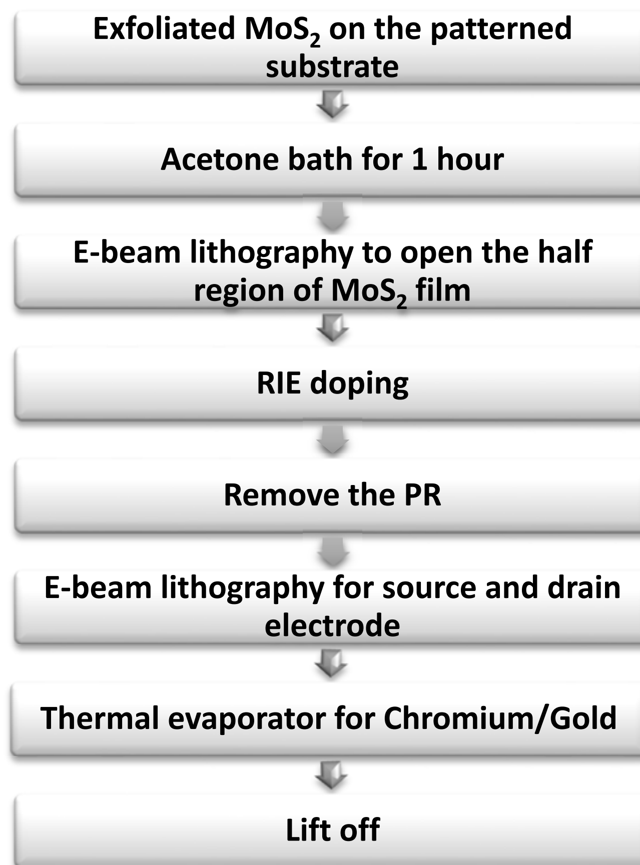

Fig. 4.20 The flow chart for MoS_2 p-n rectifying diode fabrication process.

doi:10.6342/NTU201800956

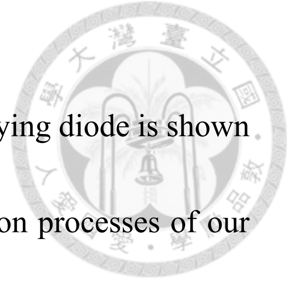

The process flow of the fabrication processes of the MoS_2 rectifying diode is shown in Fig. 4.20. Fig. 4.21 illustrates the schematic flow of the fabrication processes of our device. First, the MoS_2 flakes were mechanically exfoliated by scotch-tape technique and transferred to a patterned 300nm SiO_2/p^{++} Si substrate as shown in Fig. 4.1. After bath acetone for one hour, the half region of MoS_2 flake was opened by using E-beam lithography as shown in the dashed line in Fig. 4.22 (a). Then, the open region would be doped using RIE. Here, we use CHF_3 gas for p-type plasma doping and the RF power was 100W, the chamber pressure was 1.3 pa, the gas flow rate was 10sccm and the doping time was 30s. After removing the PR, the source and drain would be defined by E-beam lithography, followed by thermal evaporation of Cr (5nm)/Au (80nm) contact metal and lift off process. Fig. 4.22 (b) shows the completed devices under optical microscopy.

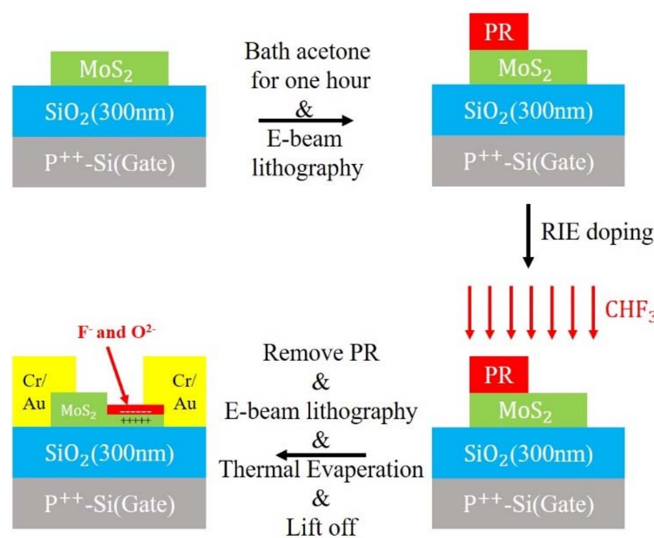

Fig. 4.21 Schematic flow of the fabrication process of MoS_2 rectify diode.

doi:10.6342/NTU201800956

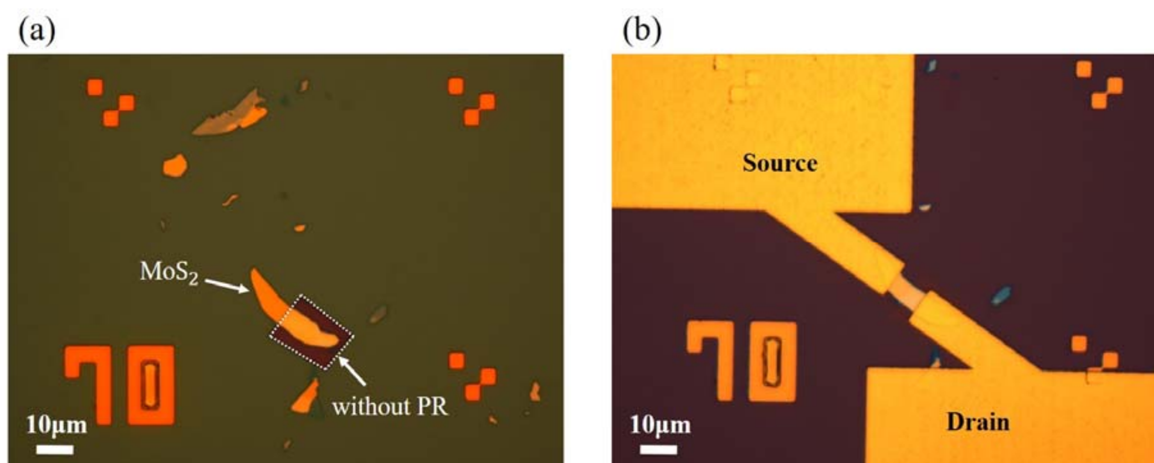

Fig. 4.22 (a) MoS_2 flake with half region open(inside the dashed line) (b) Top view of MoS_2 rectifying diode under optical microscopy.

4.5.2 Device Performance

Fig. 4.23 shows the I_d-V_d curve in log scale of MoS_2 rectifying diode. The current rectification ratio which is defined as forward current (I_F) divided by reverse current (I_R) at $|V_d| = 1V$ is about 2 order. In order to further discuss its characteristics, we will consider the ideality factor (n), which is an important parameter to determine how a real diode to an ideal diode behavior (n=1). The ideality factor n can be extracted from the I_d-V_d plot in log scale and using the slope as shown in red dashed line in Fig. 4.23, following these equations.

$$I = I_0(e^{\frac{qV}{nkT}} - 1) \tag{4.2}$$

$$n = \frac{q}{kT \times \ln(10) \times slope} \tag{4.3}$$

doi:10.6342/NTU201800956

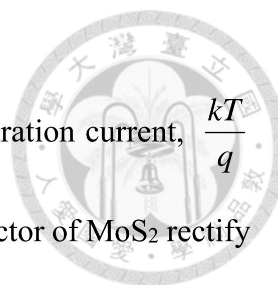

where n is the ideality factor, I is the current of diode, I_0 is the saturation current, $\frac{kT}{q}$ =25.9 (mV) at room temperature and V is the voltage. The ideality factor of MoS_2 rectify diode is 2.44 which indicates that the forward current is dominated by recombination current. In general, the ideality factor for p-n junction is in the interval between 1 and 2. Therefore, MoS_2 rectify diode is not a real p-n junction.

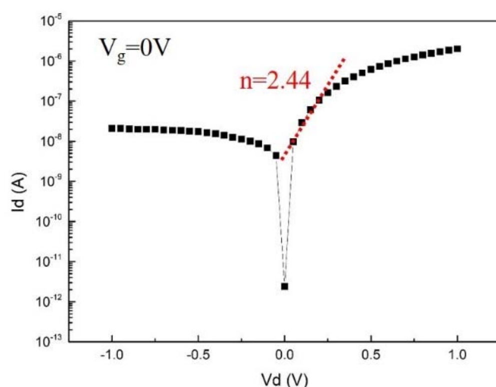

Fig. 4.23 I_d versus V_d of MoS_2 rectifying diode in log scale.

In order to further discuss the characteristics of MoS_2 rectifying diode, Xe lamp was used as a broadband light source to measure its optical properties. The emission spectra of Xe lamp is shown in Fig. 4.24.

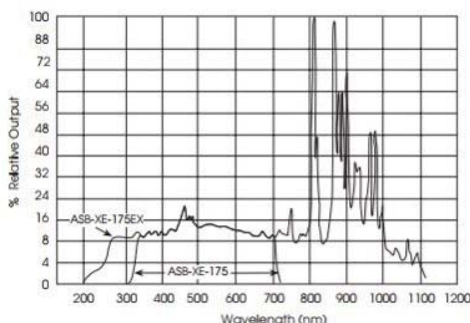

Fig. 4.24 The emission spectra of Xe lamp.

doi:10.6342/NTU201800956

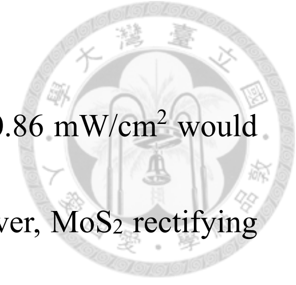

The incident light which intensities are 1.334, 4.72, 8.4 and 10.86 mW/cm^2 would be used to measure photoresponse of MoS_2 rectifying diode. However, MoS_2 rectifying diode doesn't have any photoresponse when the incident light intensity is low at 1.334 mW/cm^2. Therefore, Fig. 4.25 shows the photoresponse at V_{ds}=1V of MoS_2 rectifying diode with larger light intensity illumination from 4.72 to 10.86 mW/cm^2. In Fig. 4.25, the off region is the drain current without light illumination and the on region is the drain current with light illumination. It obviously shows on current has a strong dependence on the incident light intensity. Fig. 4.26 shows the I_d-V_d curve under dark and various incident light intensity from 4.72 to 10.86 mW/cm^2 and the inset shows the details of the negative V_d bias region. Under forward and reverse bias, as the incident light intensity increases, the photocurrent become larger. At V_{ds}=0V, the diode didn't show any photoresponse indicating that the MoS_2 rectifying diode is a photoconductor rather than a photodiode. At V_{ds}=2V, the photocurrent I_{ph}, which is defined as $I_{illumination}$-I_{dark}, where $I_{illumination}$ and I_{dark} are the drain current I_d with and without light illumination, are 17.7, 45.3 and 59.3 nA for incident light intensity 4.72, 8.4 and 10.86 mW/cm^2, respectively. Fig. 4.27 shows the responsivity R of the diode versus light intensity at V_{ds}=2V. The responsivity R, which is defined as I_{ph}/P_{laser}, where P_{laser} is the incident light intensity multiply by the device area (47 μm^2), are 7.97, 11.46 and 13.57 A/W for incident light

doi:10.6342/NTU201800956

intensity 4.72, 8.4 and 10.86 mW/cm^2, respectively. In theory, the responsivity would decrease as the light intensity increases. However, in Fig. 4.27, it shows that the responsivity slightly increases as the light intensity increases. It is because that recombination in either channel region or the underlying SiO_2 reach saturation when light intensity is large enough. Therefore, the responsivity would not decrease as the light intensity increases.

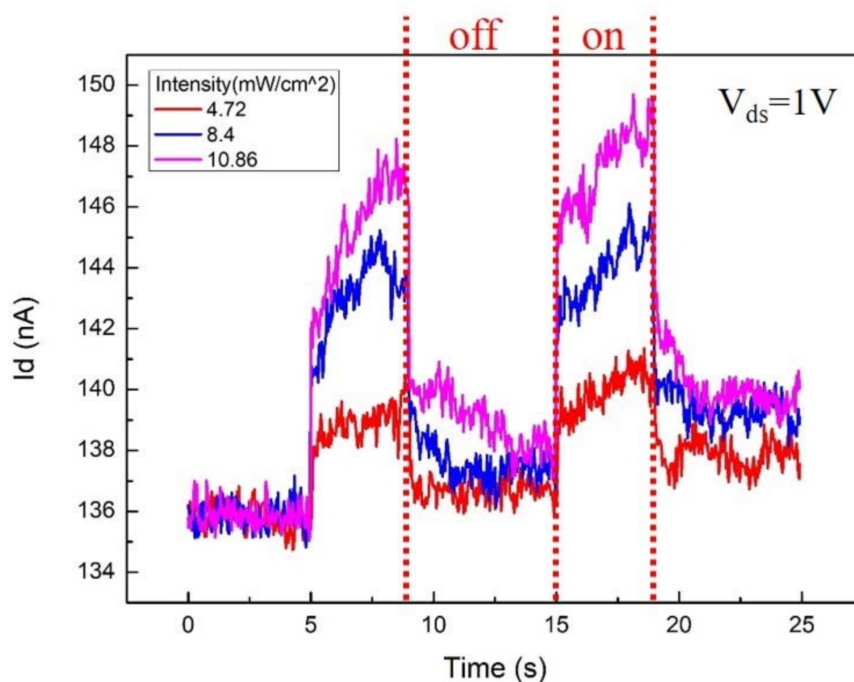

Fig. 4.25 The photoresponse of MoS_2 rectifying diode with different light intensity illumination.

doi:10.6342/NTU201800956

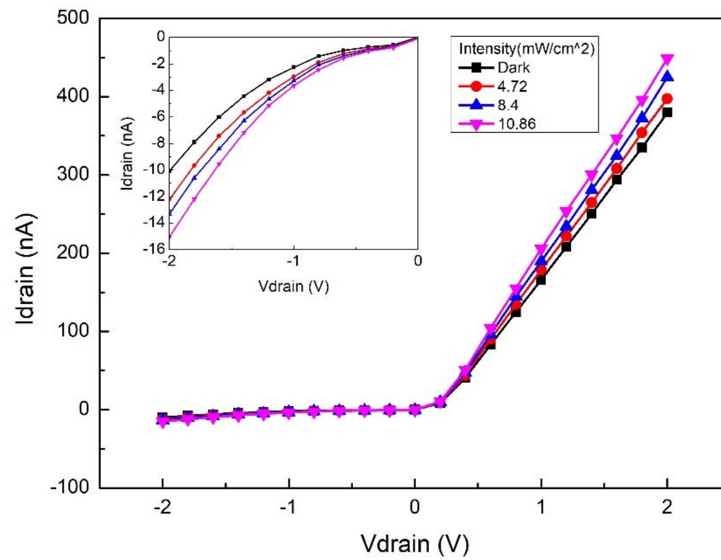

Fig. 4.26 I_d versus V_d characteristics of MoS_2 rectifying diode under various incident light intensity. The inset shows the details in the reverse bias region.

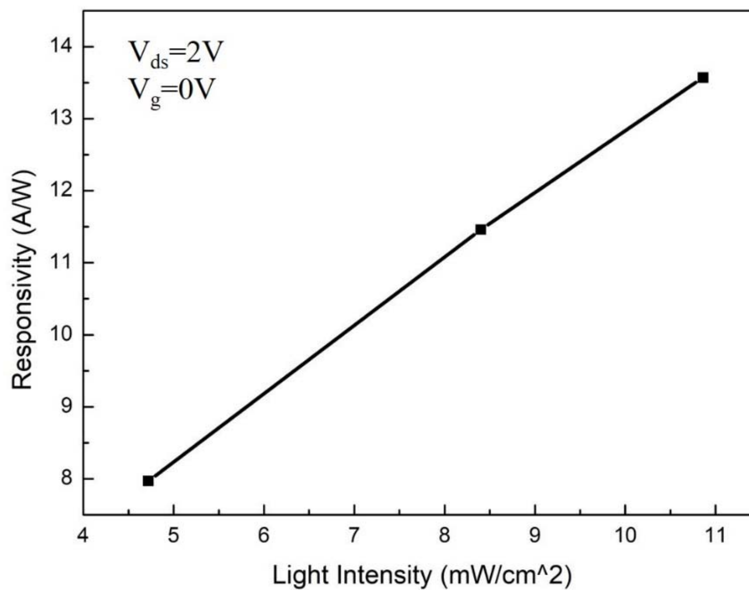

Fig. 4.27 Photodetection responsivity of MoS_2 rectifying diode versus incident light intensity.

doi:10.6342/NTU201800956

4.6 MoS_2-Black phosphorus (BP) heterostructure

In Sec. 4.5, MoS_2 rectifying diode was fabricated by using RIE doping. However, it is not a real p-n junction because its ideality factor is larger than 2. In order to fabricate a real p-n junction, black phosphorus which is a p-type 2D material was adopted as a p region and combine with n-type MoS_2 to fabricate MoS_2-BP heterostructure n-p junction. Its electronic and optical properties will be measured and discussed in this section.

4.6.1 Device Process Flow

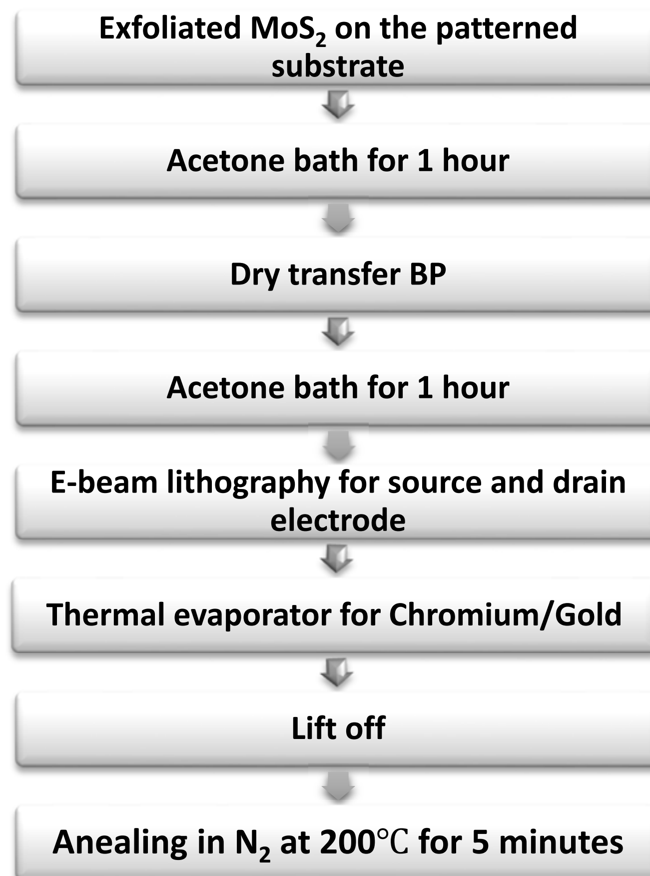

Fig. 4.28 The flow chart for MoS_2-BP heterostructure fabrication process

doi:10.6342/NTU201800956

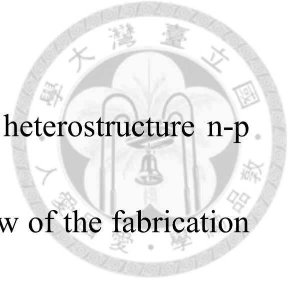

The process flow of the fabrication process for the MoS_2-BP heterostructure n-p junction is shown in Fig. 4.28. Fig. 4.29 illustrates the schematic flow of the fabrication process of our device. First, the MoS_2 flakes were mechanically exfoliated by scotch-tape technique and transferred to a patterned 300nm SiO_2/p^{++} Si substrate as shown in Fig. 4.1. After bath acetone for one hour, black phosphorus flake was transferred on the top of MoS_2 as shown in Fig. 4.30 (a) by using dry transfer. After second bath acetone for one hour, the source and drain would be defined by E-beam lithography, followed by thermal evaporation of Cr (5nm)/Au (80nm) contact metal and lift off process. Finally, the device was annealed at 200℃ for 5 minutes in N_2 to have better contact between MoS_2 and black phosphorus. Fig. 4.30 (b) shows the completed devices under optical microscopy.

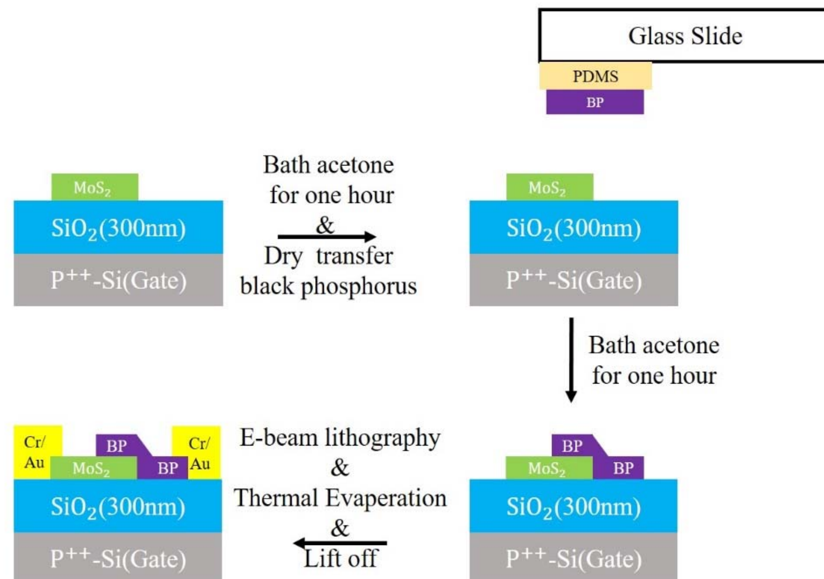

Fig. 4.29 Schematic flow of the fabrication process of MoS_2-BP heterostructure p-n junction.

doi:10.6342/NTU201800956

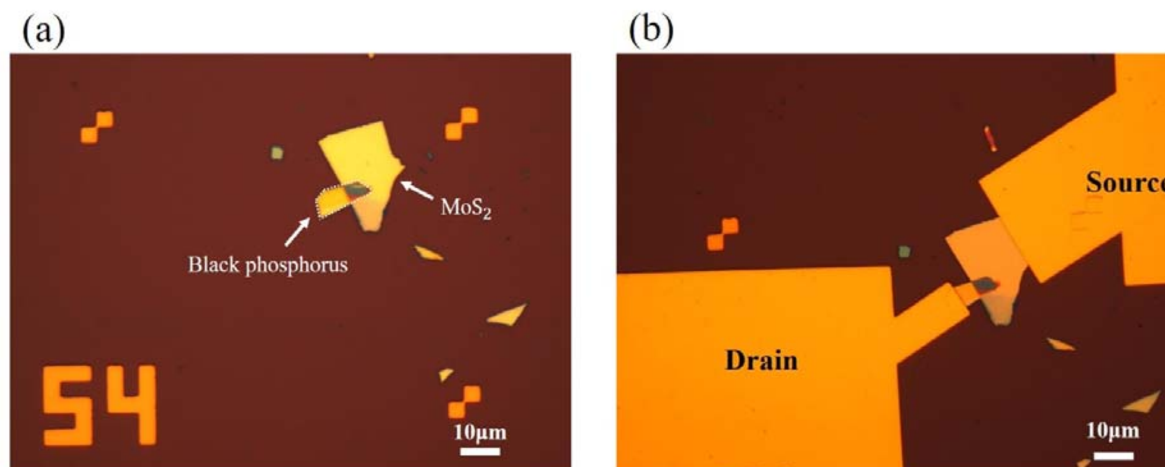

Fig. 4.30 Top view of MoS_2-BP heterostructure (a) without electrode (b) with electrode.

4.6.2 Device Performance

Fig. 4.31 shows the I_d-V_d curve in log scale of MoS_2-BP heterostructure n-p junction. The current rectification ratio as defined in Sec. 4.5.2 is 30 and its ideality factor is 1.84 extracted from Eq. (4.3). It shows that MoS_2-BP heterostructure is a real p-n junction because its ideality factor is in the interval between 1 and 2.

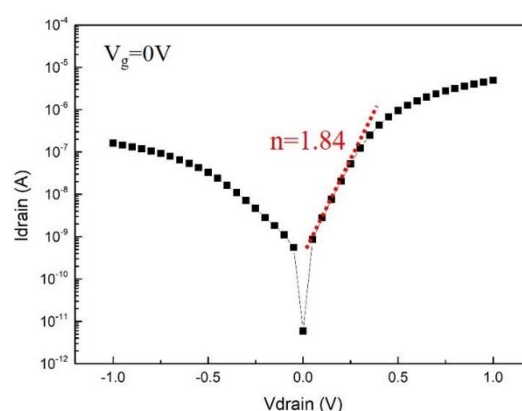

Fig. 4.31 I_d versus V_d in log scale of MoS_2-BP heterostructure n-p junction.

doi:10.6342/NTU201800956

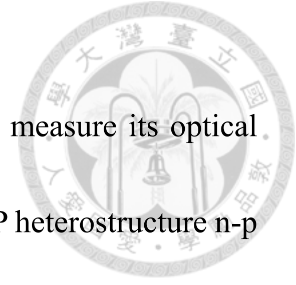

As shown in Sec. 4.5.2, the same light intensities are used to measure its optical properties. Fig. 4.32 shows the photoresponse at V_{ds}=1V of MoS_2-BP heterostructure n-p junction with different light intensity illumination (i.e. 1.334, 4.72, 8.4 and 10.86 mW/cm^2, respectively). In Fig. 4.32, the off region is the drain current without light illumination and the on region is the drain current with light illumination. It obviously shows on current has a strong dependence on the incident light intensity. Fig. 4.33 shows the I_d-V_d curve under dark and various incident light intensity from 1.334 to 10.84 mW/cm^2. The inset (1) shows the details of the negative V_d bias region and the inset (2) shows the details of the positive V_d bias region around 2V. Under reverse and forward bias, the photocurrent has a strong dependence on the incident light intensity. At V_{ds}=0V, the heterojunction didn't have any photoresponse which means MoS_2-BP heterostructure n-p junction is a photoconductor rather than a photodiode. As defined in Sec. 4.5.2, at V_{ds}=2V, the photocurrent I_{ph} are 17, 34, 53 and 77 nA for incident light intensity 1.334, 4.72, 8.4 and 10.86 mW/cm^2, respectively. Fig. 4.34 shows the responsivity R of the heterojunction versus light intensity at V_{ds}=2V. As defined in Sec. 4.5.2, the responsivity R of the heterojunction are 3.95, 2.23, 1.95 and 2.20 A/W for incident light intensity 1.334, 4.72, 8.4 and 10.86 mW/cm^2, respectively. In Fig. 4.34, it shows that the responsivity decreases before reaching an intensity of 8.4 mW/cm^2 and slightly increases after 8.4

doi:10.6342/NTU201800956

mW/cm^2. It is because the recombination reach saturation when light intensity is 8.4 mW/cm^2.

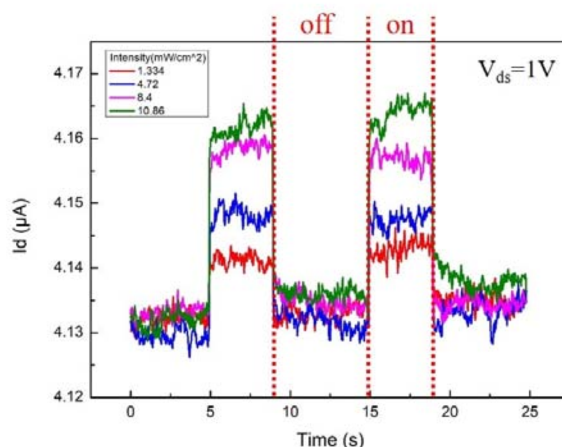

Fig. 4.32 The photoresponse of MoS_2-BP heterostructure n-p junction with different light intensity illumination.

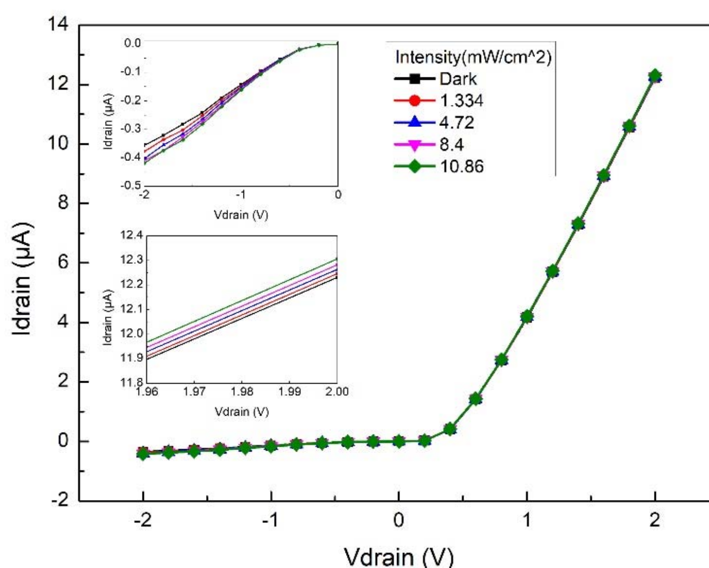

Fig. 4.33 I_d versus V_d characteristics of MoS_2-BP heterostructure n-p junction under various incident light intensity. The inset (1) shows the details in the negative bias region and the inset (2) shows the derails in the positive bias around 2V.

doi:10.6342/NTU201800956

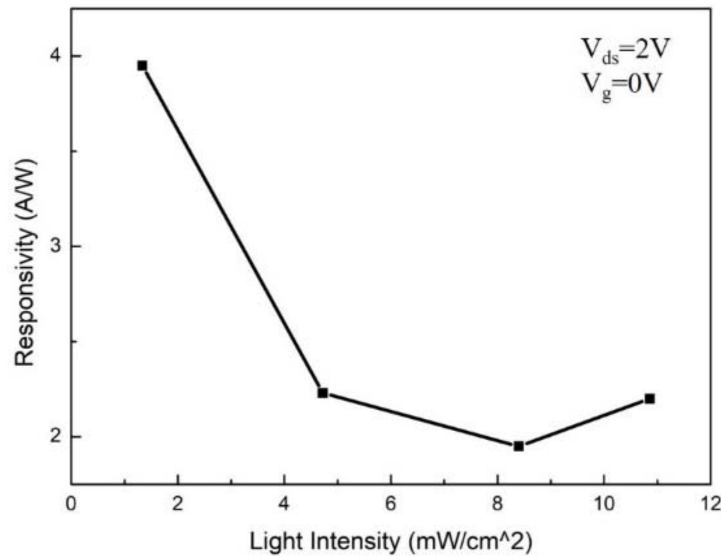

Fig. 4.34 Photodetection responsivity of MoS_2-BP heterostructure n-p junction versus incident light intensity.

In order to further discuss the above results, the MoS_2 and black phosphorus TFT were fabricated with the same fabrication processes as mentioned in Sec. 4.1.1 and their optical properties were measured. Fig. 4.35 shows the I_d-V_d curve of MoS_2 TFT under dark and various incident light intensity from 0.04037 to 10.86 mW/cm^2. The inset shows the details of the positive V_d region from 1 to 2 V. At V_{ds}=2V, the photocurrent I_{ph} are 52.3, 109, 189, 249, 320 and 412 nA for incident light intensity of 0.04037, 0.222, 1.334, 4.72, 8.4 and 10.86 mW/cm^2, respectively. The same light intensities are used to measure the optical properties of BP TFT. However, BP TFT didn't have any photoresponse when the incident light intensity is 0.04037 and 0.222 mW/cm^2. Therefore, Fig. 4.36 shows the

doi:10.6342/NTU201800956

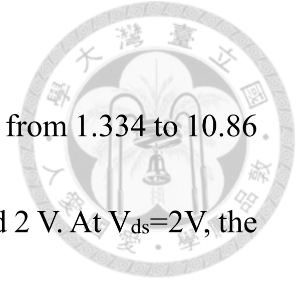

I_d-V_d curve of BP TFT under dark and various incident light intensity from 1.334 to 10.86 mW/cm^2. The inset shows the details of the positive V_d region around 2 V. At V_{ds}=2V, the photocurrent I_{ph} are 132, 191, 338 and 657 nA for incident light intensity 1.334, 4.72, 8.4 and 10.86 mW/cm^2, respectively. The black line in Fig. 4.37 shows the responsivity R of the MoS_2 TFT versus light intensity at V_{ds}=2V in semi-log scale. The responsivity R are 3083, 1164, 337, 126, 91 and 90 for incident light intensity of 0.04037, 0.222, 1.334, 4.72, 8.4 and 10.86 mW/cm^2, respectively. The red line in Fig. 4.37 shows the responsivity R of the MoS_2 TFT versus light intensity at V_{ds}=2V in semi-log scale. The responsivity R are 275, 112, 112 and 168 for incident light intensity 1.334, 4.72, 8.4 and 10.86 mW/cm^2, respectively.

From Fig. 4.27 and 4.37, it shows that MoS_2 TFT has better photodetecting ability and responsivity than MoS_2 rectifying diode. It is because the plasma doping would destroy the surface of MoS_2 which would enhance the recombination on the MoS_2 surface. Therefore, it will let the responsivity and photodetecting ability of MoS_2 rectifying diode degrade. In Fig. 4.34, it shows that MoS_2-BP heterojunction can detect the incident light when the light intensity is larger than 1.334 mW/cm^2 which is the same as BP TFT as shown in Fig. 4.37. Therefore, the photodetecting ability of MoS_2-BP heterojunction would be limited by the poor photodetecting region which is BP. Furthermore, the

doi:10.6342/NTU201800956

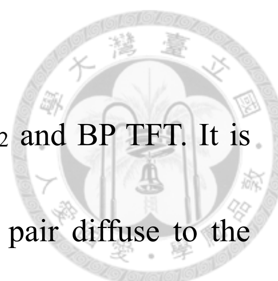

responsivity of MoS_2-BP heterojunction is lower than both of MoS_2 and BP TFT. It is because the recombination would increase when the electron-hole pair diffuse to the junction region of MoS_2-BP heterojunction which would let the responsivity become lower.

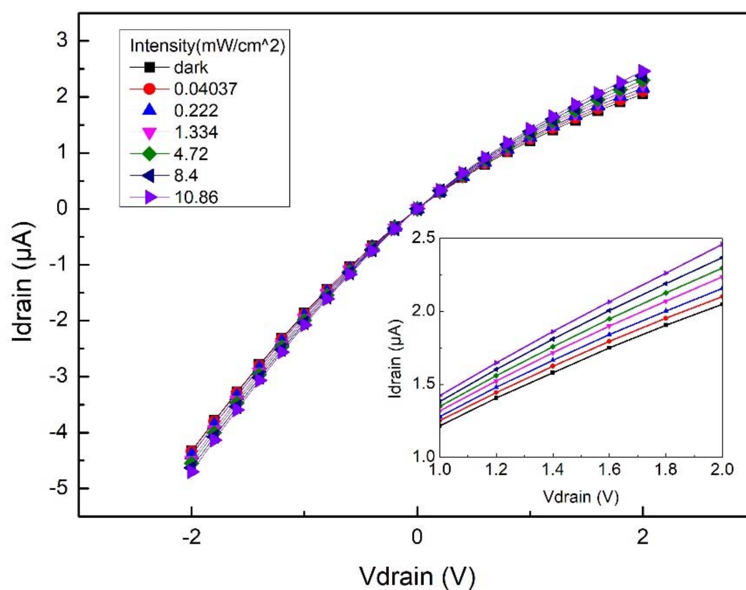

Fig. 4.35 I_d versus V_d characteristics of MoS_2 TFT under various incident light intensity. The inset shows the details in the positive bias region from 1 to 2 V.

doi:10.6342/NTU201800956

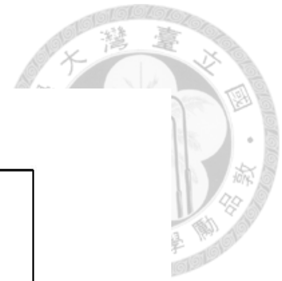

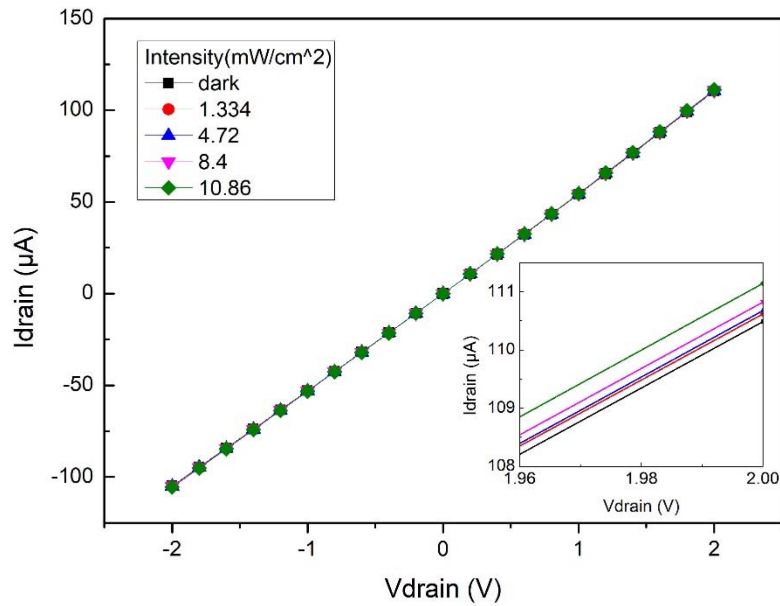

Fig. 4.36 I_d versus V_d characteristics of BP TFT under various incident light intensity. The inset shows the details in the positive bias region around 2 V.

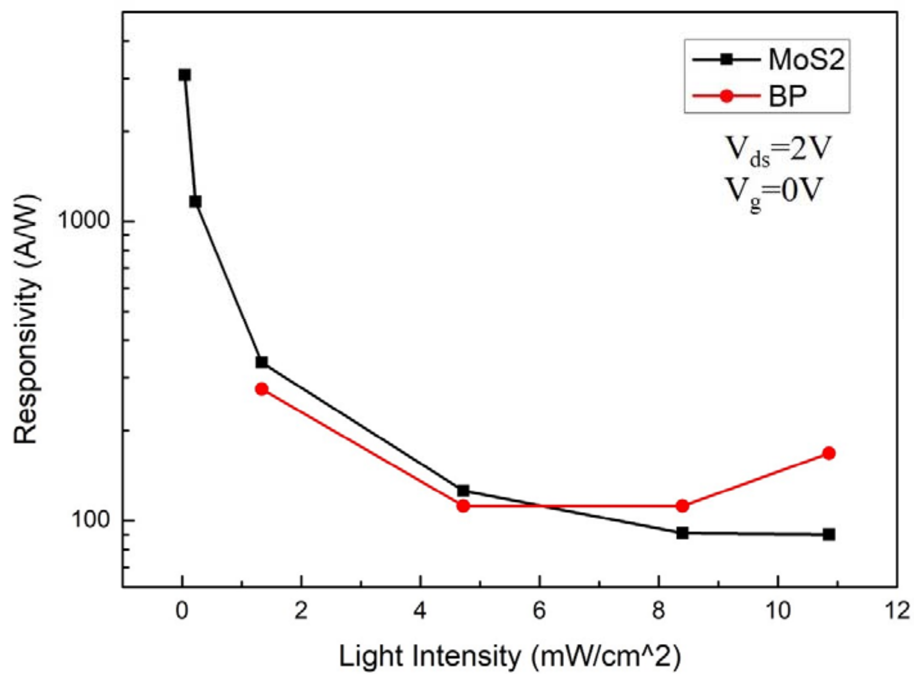

Fig. 4.37 Responsivity of MoS_2 and BP TFT versus incident light intensity in semi-log scale. The black line is MoS_2 TFT and red line is BP TFT.

doi:10.6342/NTU201800956

4.7 Summary

In the front of this chapter, back-gated MoS_2 TFTs using SiO_2 and h-BN substrate are fabricated. Both these two device show typical ohmic contact behavior by using Cr/Au metal contact. However, the interface trap between MoS_2 and SiO_2 would influence the mobility and hysteresis of MoS_2 TFT. In order to solve these problem, we use h-BN substrate to fabricate MoS_2 TFT and it has better mobility and lower hysteresis.

At the end of this chapter, MoS_2 rectifying diode is fabricated by using RIE doping. However, its ideality factor is larger than 2 which means it is not a real p-n junction. Therefore, in order to fabricate real p-n junction, black phosphorus was used to combine with MoS_2 to fabricate MoS_2-BP heterostructure n-p junction and its ideality factor is 1.84. Finally, by measuring their optical properties, it shows that although MoS_2-BP heterostructure n-p junction has lower responsivity than MoS_2 rectifying diode, it has better photodetecting ability than MoS_2 rectifying diode.

doi:10.6342/NTU201800956

Chpater 5 Conclusions

In this thesis, the electronic and optical properties of MoS_2 is studied. MoS_2 TFTs by using SiO_2 and h-BN substrate are fabricated. Finally, MoS_2 rectifying diode and MoS_2-BP heterostructure n-p junction would also be fabricated.

In Chapter 3, the MoS_2 film thickness are calibrated and measured by optical microscopy and AFM. The optical and vibrational properties of MoS_2 are explored by Raman and PL spectra. XPS is not only used to study the stability issue of ambient water and oxygen on MoS_2 surface but also measured the fermi level shift before and after the RIE doping for MoS_2 film. It shows that the Fermi level of MoS_2 film would shift about 0.4 eV toward the valence band after RIE doping by using CHF_3 plasma. Finally, UPS is also used to study the work function difference before and after RIE doping for MoS_2 film.

In Chapter 4, back-gated MoS_2 TFTs using SiO_2 and h-BN substrate are fabricated. Ohmic contacts are achieved by both substrates. MoS_2 TFT on h-BN substrate shows better mobility and lower hysteresis which is 63.5 cm^2/V-s and 0 V than that MoS_2 TFT on SiO_2 substrate which is 21.0 cm^2/V-s and 46.2 V. The best mobility of MoS_2 TFT on h-BN substrate is up to 117 cm^2/V-s. In order to further discuss the mechanism of the

doi:10.6342/NTU201800956

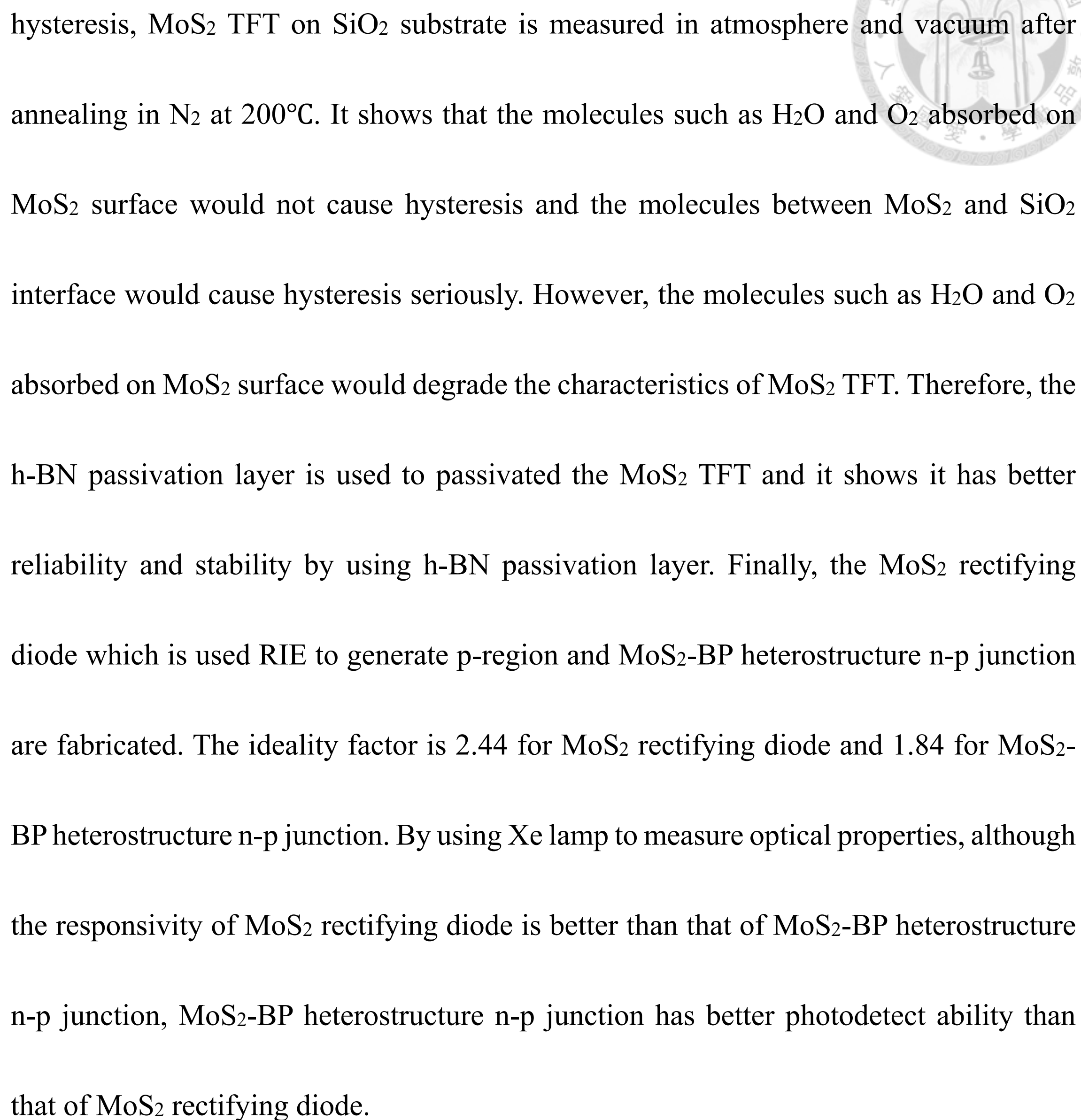

hysteresis, MoS_2 TFT on SiO_2 substrate is measured in atmosphere and vacuum after annealing in N_2 at 200℃. It shows that the molecules such as H_2O and O_2 absorbed on MoS_2 surface would not cause hysteresis and the molecules between MoS_2 and SiO_2 interface would cause hysteresis seriously. However, the molecules such as H_2O and O_2 absorbed on MoS_2 surface would degrade the characteristics of MoS_2 TFT. Therefore, the h-BN passivation layer is used to passivated the MoS_2 TFT and it shows it has better reliability and stability by using h-BN passivation layer. Finally, the MoS_2 rectifying diode which is used RIE to generate p-region and MoS_2-BP heterostructure n-p junction are fabricated. The ideality factor is 2.44 for MoS_2 rectifying diode and 1.84 for MoS_2-BP heterostructure n-p junction. By using Xe lamp to measure optical properties, although the responsivity of MoS_2 rectifying diode is better than that of MoS_2-BP heterostructure n-p junction, MoS_2-BP heterostructure n-p junction has better photodetect ability than that of MoS_2 rectifying diode.

doi:10.6342/NTU201800956

References

[1] Novoselov, K.S., A.K. Geim, S.V. Morozov, D. Jiang, Y. Zhang, S.V. Dubonos, I.V. Grigorieva, and A.A. Firsov, *Electric field effect in atomically thin carbon films.* Science, 2004. **306**(5696): p. 666-9.

[2] Mak, K.F., C.Lee, J. Hone, J. Shan, and T.F. Heinz, *Atomically thin MoS2: A new direct-gap semiconductor.* Phys Rev Lett, 2010. **105**(13): p. 136805.

[3] Lee, G.-H., X. Cui, Y.D. Kim, G. Arefe, X. Zhang, C.-H. Lee, F.Y.K. Watenabe, T. Taniguchi, P. Kim, and J. Hone, *High Stable dual gate MoS2 Transistors Encapsulated by Hexagonal Boron Nitride with Gate-Controllable Contact, Resistance, and Threshold Voltage.* ACS Nano, 2015. **9**(7): p. 7019-7026.

[4] Novoselov, K.S., D. Jiang, F. Schedin, T.J. Booth, V.V. Khotkevich, S.V. Morozov, and A.K. Geim, *Two-dimensional atomic crystals.* Proc Natl Acad Sci USA, 2005. **102**(30): p. 10451-3.

[5] Gui, G., J. Li, and J. Zhong, *Band structure engineering of graphene by strain: First-principles calculations.* Physical Review B, 2008. **78**(7).

[6] Xia, F., D.B. Farmer, Y.M. Lin, and P. Avouris, *Graphene field-effect transistors with high on/off current ratio and large transport band gap at room temperature.* Nano Lett, 2010. **10**(2): p. 715-8.

doi:10.6342/NTU201800956

[7] Radisavljevic, B., A. Radenovic, J. Brivio, V. Giacometti, and A. Kis, *Single-layer MoS2 transistors.* Nat Nanotechnol, 2011. **6**(3): p. 147-50.

[8] Wang, Q.H., K. Kalantar-Zadeh, A. Kis, J.N. Coleman, and M.S. Strano, *Electronics and optoelectronics of two-dimensional transition metal dichalcogenides.* Nat Nanotechnol, 2012. **7**(11): p. 699-712.

[9] Xu, M., T. Liang, M. Shi, and H. Chen, *Graphene-like two-dimensional materials.* Chem Rev, 2013. **113**(5): p. 3766-98.

[10] Butler, S.Z., S.M. Hollen, L. Cao, Y. Cui, J.A. Gupta, H.R. Gutierrez, T.F. Heinz, S.S. Hong, J. Huang, A.F. Ismach, E. Johnston-Halperin, M. Kuno, V.V. Plashnitsa, R.D. Robinson, R.S. Ruoff, S. Salahuddin, J. Shan, L. Shi, M.G. Spencer, M. Terrones, W. Windl, and J.E. Goldberger, *Progress, challenges, and opportunities in two-dimensional materials beyond graphene.* ASC Nano, 2013. **7**(4): p. p. 2898-926.

[11] Enyashin, A.N., L. Yadgarov, L. Houben, I. Popov, M. Weidenbach, R. Tenne, M. Bar-Sadan, and G. Seifert, *New Route for Stabilization of 1T-WS2and MoS2Phases.* The Journal of Physical Chemistry C, 2011. **115**(50): p. 24586-24591.

[12] Eda, G., H. Yamaguchi, D. Voiry, T. Fujita, M. Chen, and M. Chhowalla,

doi:10.6342/NTU201800956

Photoluminescence from chemically exfoliated MoS2. Nano Lett, 2011. **11**(12): p. 5111-6.

[13] Toh, R.J., Z. Sofer, J. Luxa, D. Sedmidubsky, and M. Pumera, *3R phase of MoS2 and WS2 outperforms the corresponding 2H phase for hydrogen evolution.* Chem Commun (Camb), 2017. **53**(21): p. 3054-3057.

[14] Wypych, F. and R. Schöllhorn, *1T-MoS2, a New Metallic Modification of Molybdenum Disulfide.* J. Chem. Soc., Chem. Commun. , 1992. **0**: p. 1386,1388.

[15] Wilson, J.A. and A.D. Yoffe, *The transition metal dichalcogenides discussion and interpretation of the observed optical, electrical and structural properties.* Advances in Physics, 1969. **18**(73): p. 193-335.

[16] Splendiani, A., L. Sun, Y. Zhang, T. Li, J. Kim, C.Y. Chim, G. Galli, and F. Wang, *Emerging photoluminescence in monolayer MoS2.* Nano Lett, 2010. **10**(4): p. 1271-5.

[17] Korn, T., S. Heydrich, M. Hirmer, J. Schmutzler, and C. Schüller, *Low-temperature photocarrier dynamics in monolayer MoS2.* Applied Physics Letters, 2011. **99**(10): p. 102109.

[18] Li, T., and G. Galli, *Electronic Properties of MoS2 Nanoparticles.* The Journal of Physical Chemistry C, 2007. **111**(44): p. 16192-16196.

doi:10.6342/NTU201800956

[19] Duan, X., C. Wang, A. Pan, R. Yu, and X. Duan, *Two-dimensional transition metal dichalcogenides as atomically thin semiconductors: opportunities and challenges.* Chem Soc Rev, 2015. **44**(24): p. 8859-76.

[20] Terrones, H., F. Lopez-Urias, and M. Terrones, *Novel hetero-layered materials with tunable direct band gaps by sandwiching different metal disulfides and diselenides.* Sci Rep, 2013. **3**: p. 1549.

[21] Liu, H. and P.D. Ye, *MoS2 Dual-Gate MOSFET With Atomic-Layer-Deposited Al2O3 as Top-Gate Dielectric.* IEEE Electron Device Letters, 2012. **33**(4): p. 546-548.

[22] Kim, S., A. Konar, W.S. Hwang, J.H. Lee, J. Lee, J. Yang, C. Jung, H. Kim, J.B. Yoo, J.Y. Choi, Y.W. Jin, S.Y. Lee, D. Jena, W. Choi, and K. Kim, *High-mobility and low-power thin-film transistors based on multilayer MoS2 crystals.* Nat Commun, 2012. **3**: p. 1011.

[23] Yu, N., L. Wang, M. Li, X. Sun, T. Hou, and Y. Li, *Molybdenum disulfide as a highly efficient adsorbent for non-polar gases.* Phys Chem Chem Phys, 2015. **17**(17): p. 11700-4.

[24] Yang, L., K. Majumdar, H. Liu, Y. Du, H. Wu, M. Hatzistergos, P.Y. Hung, R. Tieckelmann, W. Tsai, C. Hobbs, and P.D. Ye, *Chloride molecular doping*

doi:10.6342/NTU201800956

technique on 2D materials: WS2 and MoS2. Nano Lett, 2014. **14**(11): p. 6275-80.

[25] Li, H., Z. Yin, Q. He, H. Li, X. Huang, G. Lu, D.W. Fam, A.I. Tok, Q. Zhang, and H. Zhang, *Fabrication of single- and multilayer MoS2 film-based field-effect transistors for sensing NO at room temperature.* Small, 2012. **8**(1): p. 63-7.

[26] Late, D.J., Y.K. Huang, B. Liu, J. Acharya, S.N. Shirodkar, J. Luo, A. Yan, D. Charles, U.V. Waghmare, V.P. Dravid, and C.N. Rao, *Sensing behavior of atomically thin-layered MoS2 transistors.* ASC Nano, 2013. **7**(6): p. 4879-91.

[27] Sarkar, D., W. Liu, X. Xie, A.C. Anselmo, S. Mitragotri, and K. Banerjee, *MoS2 Field Effect Transistor for next generation label-free biosensors.* ASC Nano, 2014. **8**(4): p. 3992-4003.

[28] Cho, B., M.G. Hahm, M. Choi, J. Yoon, A.R. Kim, Y.J. Lee, S.G. Park, J.D. Kwon, C.S. Kim, M. Song, Y. Jeong, K.S. Nam, S. Lee, T.J. Yoo, C.G. Kang, B.H. Lee, H.C. Ko, P.M. Ajayan, and D.H. Kim, *Charge-transfer-based gas sensing using atomic-layer MoS2.* Sci Rep, 2015. **5**: p. 8052.

[29] Zhang, E., W. Wang, C. Zhang, Y. Jin, G. Zhu, Q. Sun, D.W. Zhang, P. Zhou, and F. Xiu, *Tunable charge-trap memory based on few-layer MoS2.* ASC Nano,

doi:10.6342/NTU201800956

2015. **9**(1): p. 612-9.

[30] Wang, J., X. Zou, X. Xiao, L. Xu, C. Wang, C. Jiang, J.C. Ho, T. Wang, J. Li, and L. Liao, *Floating gate memory-based monolayer MoS2 transistor with metal nanocrystals embedded in the gate dielectrics.* Small, 2015. **11**(2): p. 208-13.

[31] Chen, M., H. Nam, S. Wi, G. Priessnitz, I.M. Gunawan, and X. Liang, *Multibit data storage states formed in plasma-treated MoS2 transistors.* ASC Nano, 2014. **8**(4): p. 4023-32.

[32] Tang, W., C. Liu, L. Wang, X. Chen, M. Luo, W. Guo, S.-W. Wang, and W. Lu, *MoS2 nanosheet photodetectors with ultrafast response.* Applied Physics Letters, 2017. **111**(15): p. 153502.

[33] Cheng, R., D. Li, H. Zhou, C. Wang, A. Yin, S. Jiang, Y. Liu, Y. Chen, Y. Huang, and X. Duan, *Electroluminescence and photocurrent generation from atomically sharp WSe2/MoS2 heterojunction p-n diodes.* Nano Lett, 2014. **14**(10): p. 5590-7.

[34] Furchi, M.M., A. Pospischil, F. Libisch, J. Burgdorfer, and T. Mueller, *Photovoltaic effect in an electrically tunable van der Waals heterojunction.* Nano Lett, 2014. **14**(8): p. 4785-91.

[35] Li, M.Y., Y. Shi, C.C. Cheng, L.S. Lu, Y.C. Lin, H.L. Tang, M.L. Tsai, C.W.

doi:10.6342/NTU201800956

Chu, K.H. Wei, J.H. He, W.H. Chang, K. Suenaga, and L.J. Li, *Epitaxial growth of a monolayer WSe2-MoS2 lateral p-n junction with an atomically sharp interface.* Science, 2015. **349**(6247): p. 524-528.

[36] Schaller and R.R., *Moore's law: past, present and future.* IEEE Spectrum, 1997. **34**(6): p. 52-59.

[37] Schwierz, F., *Graphene transistors.* Nat Nanotechnol, 2010. **5**(7): p. 487-96.

[38] Frank, D.J., Y. Taur, and H.S.P. wong, *Generalized scale length for two-dimensional effects in MOSFET's.* IEEE Electron Device Letters, 1998. **19**(10): p. 385-387.

[39] Yan, R.H., A. Ourmazd, and K.F. Lee, *Scaling the Si MOSFET: From Bulk to SOI to Bulk.* IEEE Transactions on Electron Devices, 1992. **39**(7): p. 1704-1710.

[40] Yoon, Y., K. Ganapathi, and S. Salahuddin, *How good can monolayer MoS(2) transistors be?* Nano Lett, 2011. **11**(9): p. 3768-73.

[41] Liu, L., S.B. Kumar, Y. Ouyang, and J. Guo, *Performance Limits of Monolayer Transition Metal Dichalcogenide Transistors.* IEEE Transactions on Electron Devices, 2011. **58**(9): p. 3042-3047.

[42] Fiori, G., F. Bonaccorso, G. Iannaccone, T. Palacios, D. Neumaier, A. Seabaugh, S.K. Banerjee, and L. Colombo, *Electronics based on two-dimensional*

doi:10.6342/NTU201800956

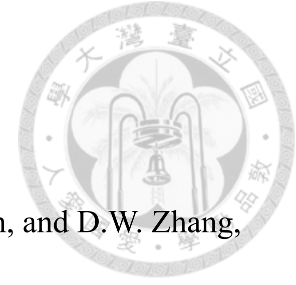

materials. Nat Nanotechnol, 2014. **9**(10): p. 768-79.

[43] Wang, X., T.-B. Zhang, W. Yang, H. Zhu, L. Chen, Q.-Q. Sun, and D.W. Zhang, *Improved integration of ultra-thin high-k dielectrics in few-layer MoS2 FET by remote forming gas plasma pretreatment.* Applied Physics Letters, 2017. **110**(5): p. 053110.

[44] Bolshakov, P., P. Zhao, A. Azcatl, P.K. Hurley, R.M. Wallace, and C.D. Young, *Improvement in top-gate MoS2 transistor performance due to high quality backside Al2O3 layer.* Applied Physics Letters, 2017. **111**(3): p. 032110.

[45] Kolla, L.G., S. Bhattacharjee, M. S, and N. Bhat, *High Performance HfO2 Back Gated Multilayer MoS2 transistors.* IEEE Electron Device Letters, 2016: p. 1-1.

[46] Yang, W., Q.Q. Sun, Y. Geng, L. Chen, P. Zhou, S.J. Ding, and D.W. Zhang, *The Integration of Sub-10 nm Gate Oxide on MoS2 with Ultra Low Leakage and Enhanced Mobility.* Sci Rep, 2015. **5**: p. 11921.

[47] Lee, G.H., Y.J. Yu, X. Cui, N. Petrone, C.H. Lee, M.S. Choi, D.Y. Lee, C. Lee, W.J. Yoo, K. Watanabe, T. Taniguchi, C. Nuckolls, P. Kim, and J. Hone, *Flexible and transparent MoS2 field effect transistors on hexagonal boron nitride-graphene heterostructures.* ASC Nano, 2013. **7**(9): p. 7931-7936.

[48] Egginger, M., S. Bauer, R. Schwödiauer, H. Neugebauer, and N.S. Sariciftci,

doi:10.6342/NTU201800956

Current versus gate voltage hysteresis in organic field effect transistors. Monatshefte für Chemie - Chemical Monthly, 2009. **140**(7): p. 735-750.

[49] Late, D.J., B. Liu, H.S.S.R. Matte, V.P. Dravid, and C.N.R. Rao, *Hysteresis in Single-Layer MoS2 Field Effect Transistors* ACS Nano, 2012. **6**(6): p. 5635-5641.

[50] Li, T., G. Du, B. Zhang, and Z. Zeng, *Scaling behavior of hysteresis in multilayer MoS2 field effect transistors.* Applied Physics Letters, 2014. **105**(9): p. 093107.

[51] Cho, A.-J., S. Yang, K. Park, S.D. Namgung, H. Kim, and J.-Y. Kwon, *Multi-Layer MoS2 FET with Small Hysteresis by Using Atomic Layer Deposition Al2O3 as Gate Insulator.* ECS Solid State Letters, 2014. **3**(10): p. Q67-Q69.

[52] Guo, Y., X. Wei, J. Shu, B. Liu, J. Yin, C. Guan, Y. Han, S. Gao, and Q. Chen, *Charge trapping at the MoS2-SiO2 interface and its effects on the characteristics of MoS2 metal-oxide-semiconductor field effect transistors.* Applied Physics Letters, 2015. **106**(10): p. 103109.

[53] Iqbal, M.W., M.Z. Iqbal, X. Jin, J. Eom, and C. Hwang, *Superior characteristics of graphene field effect transistor enclosed by chemical-vapor-deposition-grown hexagonal boron nitride.* J. Mater. Chem. C, 2014. **2**(37): p. 7776-7784.

doi:10.6342/NTU201800956

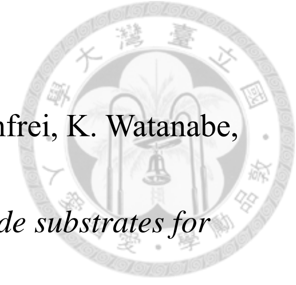

[54] Dean, C.R., A.F. Young, I. Meric, C. Lee, L. Wang, S. Sorgenfrei, K. Watanabe, T. Taniguchi, P. Kim, K.L. Shepard, and J. Hone, *Boron nitride substrates for high-quality graphene electronics.* Nat Nanotechnol, 2010. **5**(10): p. 722-6.

[55] Park, W., J. Park, J. Jang, H. Lee, H. Jeong, K. Cho, S. Hong, and T. Lee, *Oxygen environmental and passivation effects on molybdenum disulfide field effect transistors.* Nanotechnology, 2013. **24**(9): p. 095202.

[56] Zhao, P., D. Kiriya, A. Azcatl, C. Zhang, M. Tosun, Y.-S. Liu, M. Hettick, J.S. Kang, S. McDonnell, S. KC, K. Guo, K. Cho, R.M. Wallce, and A. Javey, *Air stable p-doping of WSe2 by covalent functionalization.* ACS Nano, 2014. **8**(10): p. 10808-10814.

[57] Lin, J.D., C. Han, F. Wang, R. Wang, D. Xiang, S. Qin, X.-A. Zhang, L. Wang, H. Zhang, A.T.S. Wee, and W. Chen, *Electron-doping-enhanced trion formation in monolayer Molybdenum Disulfide functionalized with cesium carbonate.* ACS Nano, 2014. **8**(5): p. 5323-5329.

[58] Chen, K., D. Kiriya, M. Hettick, M. Tosun, T.-J. Ha, S.R. Madhvapathy, S. Desai, A. Sachid, and A. Javey, *Air stable n-doping of WSe2 by silicon nitride thin films with tunable fixed charge density.* APL Materials, 2014. **2**(9): p. 092504.

doi:10.6342/NTU201800956

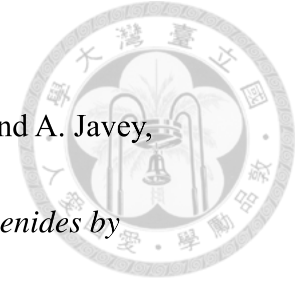

[59] Fang, H., M. Tosun, G. Seol, T.C. Chang, K. Takei, J. Guo, and A. Javey, *Degenerate n-doping of few-layer transition metal dichalcogenides by potassium.* Nano Lett, 2013. **13**(5): p. 1991-5.

[60] Kang, D.-H., M.-S. Kim, J. Shim, J. Jeon, H.-Y. Park, W.-S. Jung, H.-Y. Yu, C.-H. Pang, S. Lee, and J.-H. Park, *High-Performance Transition Metal Dichalcogenide Photodetectors Enhanced by Self-Assembled Monolayer Doping*. Advanced Functional Materials, 2015. **25**(27): p. 4219-4227.

[61] Tarasov, A., S. Zhang, M.Y. Tsai, P.M. Campbell, S. Graham, S. Barlow, S.R. Marder, and E.M. Vogel, *Controlled doping of large-area trilayer MoS2 with molecular reductants and oxidants.* Adv Mater, 2015. **27**(7): p. 1175-81.

[62] Kiriya, D., M. Tosun, P. Zhao, J.S. Kang, and A. Javey, *Air-stable surface charge transfer doping of MoS2 by benzyl viologen.* J Am Chem Soc, 2014. **136**(22): p. 7853-6.

[63] Amani, M., D.-H. Lien, D. Kiriya, J. Xiao, A. Azcatl, J. Noh, K. Cho, R.M. Wallace, S.-C. Lee, J.-H. He, J.W. Ager, X. Zhang, E. Yablonovitch, and A. Javey, *Near-unity photoluminescence quantum yield in MoS2.* Science, 2015. **350**(6265): p. 1065-1068.

[64] Chen, M., S. Wi, H. Nam, G. Priessnitz, and X. Liang, *Effects of MoS2 thickness*

doi:10.6342/NTU201800956

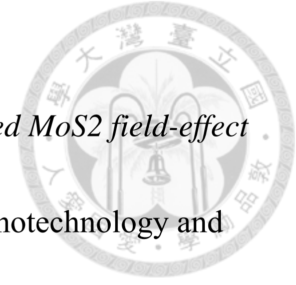

and air humidity on transport characteristics of plasma-doped MoS2 field-effect transistors. Journal of Vacuum Science & Technology B, Nanotechnology and Microelectronics: Materials, Processing, Measurement, and Phenomena, 2014. **32**(6): p. 06FF02.

[65] Nam, H., S. Wi, H. Rokni, M. Chen, G. Priessnitz, W. Lu, and X. Liang, *MoS2 transistors fabricated via plasma-assisted nanoprinting of few-layer MoS2 flakes into large area arrays.* ACS Nano, 2013. **7**(7): p. 5870-5881.

[66] Wi, S., H. Kim, M. Chen, H. Nam, L.J. Guo, E. Meyhofer, and X. Liang, *Enhancement of photovoltaic response in multilayer MoS2 induced by plasma doping.* ACS Nano, 2014. **8**: p. 5270-5281.

[67] Choudhary, N., M.R. Islam, N. Kang, L. Tetard, Y. Jung, and S.I. Khondaker, *Two-dimensional lateral heterojunction through bandgap engineering of MoS2 via oxygen plasma.* J Phys Condens Matter, 2016. **28**(36): p. 364002.

[68] Chen, M., H. Nam, S. Wi, L. Ji, X. Ren, L. Bian, S. Lu, and X. Liang, *Stable few-layer MoS2 rectifying diodes formed by plasma-assisted doping.* Applied Physics Letters, 2013. **103**(14): p. 142110.

[69] Late, D.J., B. Liu, H.S.S.R. Matte, C.N.R. Rao, and V.P. Dravid, *Rapid Characterization of Ultrathin Layers of Chalcogenides on SiO2/Si Substrates.*

doi:10.6342/NTU201800956

Advanced Functional Materials, 2012. **22**(9): p. 1894-1905.

[70] Li, H., Q. Zhang, C.C.R. Yap, B.K. Tay, T.H.T. Edwin, A. Olivier, and D. Baillargeat, *From Bulk to Monolayer MoS2: Evolution of Raman Scattering*. Advanced Functional Materials, 2012. **22**(7): p. 1385-1390.

[71] Tongay, S., J. Zhou, C. Ataca, J. Liu, J.S. Kang, T.S. Matthews, L. You, J. Li, J.C. Grossman, and J. Wu, *Broad-range modulation of light emission in two-dimensional semiconductors by molecular physisorption gating*. Nano Lett, 2013. **13**(6): p. 2831-6.

[72] Nan, H., Z. Wang, W. Wang, Z. Liang, Y. Lu, Q. Chen, D. He, P. Tan, F. Miao, X. Wang, j. Wang, and Z. Ni, *Strong photoluminescence enhancement of MoS2 through defect engineering and oxygen bonding*. ACS Nano, 2014. **8**(6): p. 5738-5745.

[73] Lin, Y.C., W. Zhang, J.K. Huang, K.K. Liu, Y.H. Lee, C.T. Liang, C.W. Chu, and L.J. Li, *Wafer-scale MoS2 thin layers prepared by MoO3 sulfurization.* Nanoscale, 2012. **4**(20): p. 6637-41.

[74] Kim, K.K., A. Hsu, X. Jia, S.M. Kim, Y. Shi, M. Dresselhaus, T. Palacios, and J. Kong, *Synthesis and Characterization of Hexagonal Boron Nitride Film as a Dielectric Layer for Graphene Devices.* ACS Nano. **6**(10): p. 8583-8590.

doi:10.6342/NTU201800956

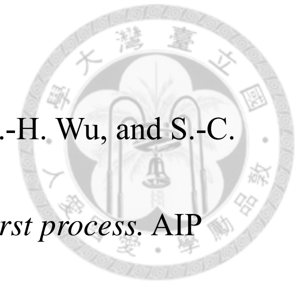

[75] Chang Chien, C.-S., H.-M. Chang, W.-T. Lee, M.-R. Tang, C.-H. Wu, and S.-C. Lee, *High performance MoS2 TFT using graphene contact first process.* AIP Advances, 2017. **7**(8): p. 085018.

doi:10.6342/NTU201800956